The Intrinsic Characteristics of Galaxies on the SFR–M ▯ Plane at 1.2 < z < 4: I. The Correlation between Stellar Age, Central Density, and Position Relative to the Main Sequence

Item Type	Article
Authors	Lee, Bomee; Giavalisco, Mauro; Whitaker, Katherine E.; Williams, Christina C.; Ferguson, Henry C.; Acquaviva, Viviana; Koekemoer, A.; Straughn, Amber N.; Guo, Yicheng; Kartaltepe, Jeyhan S.; Lotz, Jennifer; Pacifici, Camilla; Croton, Darren J.; Somerville, Rachel S.; Lu, Yu
Citation	The Intrinsic Characteristics of Galaxies on the SFR–M ▯ Plane at 1.2 < z < 4: I. The Correlation between Stellar Age, Central Density, and Position Relative to the Main Sequence 2018, 853 (2):131 The Astrophysical Journal
DOI	10.3847/1538-4357/aaa40f
Publisher	IOP PUBLISHING LTD
Journal	The Astrophysical Journal
Rights	© 2018. The American Astronomical Society. All rights reserved.
Download date	26/08/2022 03:07:50
Item License	http://rightsstatements.org/vocab/InC/1.0/
Version	Final published version
Link to Item	http://hdl.handle.net/10150/627039

CrossMark

The Intrinsic Characteristics of Galaxies on the SFR–M_* Plane at $1.2 < z < 4$: I. The Correlation between Stellar Age, Central Density, and Position Relative to the Main Sequence

Bomee Lee[1,2] , Mauro Giavalisco[1] , Katherine Whitaker[1,3,15] , Christina C. Williams[4] , Henry C. Ferguson[5] ,
Viviana Acquaviva[6] , Anton M. Koekemoer[5] , Amber N. Straughn[7], Yicheng Guo[8,9] , Jeyhan S. Kartaltepe[10] ,
Jennifer Lotz[5] , Camilla Pacifici[7,16] , Darren J. Croton[11] , Rachel S. Somerville[12,13], and Yu Lu[14]

[1] Department of Astronomy, University of Massachusetts, Amherst, MA 01003, USA; bomee@ipac.caltech.edu
[2] Infrared Processing and Analysis Center, California Institute of Technology, Pasadena, CA 91125, USA
[3] Department of Physics, University of Connecticut, Storrs, CT 06269, USA
[4] Steward Observatory, University of Arizona, 933 N. Cherry Avenue, Tucson, AZ 85721, USA
[5] Space Telescope Science Institute, 3700 San Martin Drive, Baltimore, MD 21218, USA
[6] Department of Physics, CUNY NYC College of Technology, 300 Jay Street, Brooklyn NY 11201, USA
[7] Goddard Space Flight Center, Code 665, Greenbelt, MD 20771, USA
[8] UCO/Lick Observatory, Department of Astronomy and Astrophysics, University of California, Santa Cruz, CA 95064, USA
[9] Department of Physics and Astronomy, University of Missouri, Columbia, MO 65211, USA
[10] School of Physics and Astronomy, Rochester Institute of Technology, 84 Lomb Memorial Drive, Rochester, NY 14623, USA
[11] Centre for Astrophysics & Supercomputing, Swinburne University of Technology, P.O. Box 218, Hawthorn, Victoria 3122, Australia
[12] Department of Physics and Astronomy, Rutgers, The State University of New Jersey, NJ 08854, USA
[13] Center for Computational Astrophysics, Flatiron Institute, New York, NY 10010, USA
[14] The Observatories, The Carnegie Institution for Science, 813 Santa Barbara Street, Pasadena, CA 91101, USA

Abstract

We use the deep CANDELS observations in the GOODS North and South fields to revisit the correlations between stellar mass (M_*), star formation rate (SFR) and morphology, and to introduce a fourth dimension, the mass-weighted stellar age, in galaxies at $1.2 < z < 4$. We do this by making new measures of M_*, SFR, and stellar age thanks to an improved SED fitting procedure that allows various star formation history for each galaxy. Like others, we find that the slope of the main sequence (MS) of star formation in the (M_*; SFR) plane bends at high mass. We observe clear morphological differences among galaxies across the MS, which also correlate with stellar age. At all redshifts, galaxies that are quenching or quenched, and thus old, have high Σ_1 (the projected density within the central 1 kpc), while younger, star-forming galaxies span a much broader range of Σ_1, which includes the high values observed for quenched galaxies, but also extends to much lower values. As galaxies age and quench, the stellar age and the dispersion of Σ_1 for fixed values of M_* shows two different regimes: one at the low-mass end, where quenching might be driven by causes external to the galaxies; the other at the high-mass end, where quenching is driven by internal causes, very likely the mass given the low scatter of Σ_1 (mass quenching). We suggest that the monotonic increase of central density as galaxies grow is one manifestation of a more general phenomenon of structural transformation that galaxies undergo as they evolve.

Key words: galaxies: evolution – galaxies: formation – Galaxy: structure – techniques: photometric

1. Introduction

Deep multi-wavelength surveys like CANDELS (Cosmic Assembly Near-infrared Extragalactic Legacy Survey: Grogin et al. 2011; Koekemoer et al. 2011) have provided a tremendous amount of new observational data for a large sample of galaxies over the last few years. These surveys enable us to explore the universe at redshifts $z = 1$–3, the peak epoch of star formation and active galactic nuclei (AGN) activity (Madau & Dickinson 2014), and very likely the epoch when the Hubble sequence formed (Kriek et al. 2009; Szomoru et al. 2011; Wuyts et al. 2011; Lee et al. 2013). This peak in the star formation rate density of the universe signals a transition in the mode of galaxy evolution, from the early universe galaxies, which form stars rapidly, presumably due to an abundance of cold gas, to an epoch of less star formation and more passive evolution. Indeed a number of studies have reported the emergence of massive compact quiescent galaxies by $z \sim 2$–3

(Cimatti et al. 2004; Trujillo et al. 2006, 2007; Cassata et al. 2008, 2010; van Dokkum et al. 2008). Their number density increases rapidly, by a factor of five, after $z \sim 1$, and they are up to five times more compact in size than local ones with similar stellar masses (Cassata et al. 2011, 2013). However, ellipsoidal, compact quiescent galaxies are morphologically very dissimilar from their more extended disky star-forming counterparts (Kriek et al. 2009; Cassata et al. 2011; Szomoru et al. 2011; Cheung et al. 2012; Guo et al. 2012; Lee et al. 2013).

Quenching appears to be tied to morphological transitions, but this process is very poorly understood. Several quenching mechanisms have been proposed to explain the formation of quiescent galaxies. In general, very compact and massive galaxies are thought to be a result of a highly dissipative process, either (1) gas-rich mergers (Springel et al. 2005; Hopkins et al. 2006, 2008; Wuyts et al. 2010), or (2) direct accretion of cold gas driven by violent disk instabilities in a compact disk (VDI; Dekel et al. 2009; Genzel et al. 2011) or by gas traveling directly to the galaxy center and forming stars

---
[15] Hubble Fellow.
[16] NASA Postdoctoral Program Fellow.

in situ (Johansson et al. 2012). The quenching of star formation subsequently takes place late when the gas supply is halted. Recently, it has been proposed that a significant fraction of quiescent galaxies at $z > 2$ are actually compact rotating disks (van der Wel et al. 2011; Bruce et al. 2012), as opposed to systems stabilized by a significant, or dominant, fraction of velocity dispersion. The presence of passive disks seems inconsistent with a classical model, in which galaxy morphology is transformed from a disk into a spheroid and star formation subsequently quenches. However, recent hydrodynamic simulations predict that passive disks at $z > 2$ will form when cold gas inflows are halted, thus quenching star formation without transformation of morphology (Keres et al. 2005; Dekel & Birnboim 2008; Wellons et al. 2015). Consistent with this scenario, Williams et al. (2014) argued that compact galaxies simply assemble at very early times and evolve through in situ star formation by studying morphologies and volume densities of massive early-type galaxies at $z \sim 2$ and those of compact star-forming galaxies at $z > 3$. Moreover, using semi-analytic models, Brennan et al. (2015) found that the fractions of atypical galaxies (star-forming spheroids and quiescent disks) are non-negligible and stay constant at $0 < z < 3$. They showed that these atypical galaxies follow different evolutionary paths compared with major populations, star-forming disks, and quiescent spheroids. The existence of such atypical galaxies suggests that the physical mechanism responsible for quenching star formation may, at least in some cases, be distinct from the process responsible for the morphological transformation. Therefore, in principle, one should study the morphologies of galaxies in different star formation regimes to constrain the dominant quenching mechanism and solve the puzzle of galaxy evolution.

Classifying galaxies into different star formation regimes at high redshift is facilitated by the fact that star formation rate (SFR) and stellar mass (M_*) of star-forming galaxies (SFGs) are strongly correlated out to at least $z \sim 4$ (Daddi et al. 2007; Noeske et al. 2007; Pannella et al. 2009, 2015; Elbaz et al. 2011; Whitaker et al. 2012, 2014; Lee et al. 2015; Salmon et al. 2015; Schreiber et al. 2015; Tomczak et al. 2016). This correlation is commonly called the "main sequence of star formation" (MS). A common interpretation of the MS is that the location of galaxies relative to the MS follows a different time evolution of SFR (Renzini 2009; Daddi et al. 2010; Rodighiero et al. 2011; Sargent et al. 2012; Renzini & Peng 2015). The tight MS with near unity slope reflects that the majority of SFGs follow a steadily increasing star formation history governed by a set of gradual physical processes like gas exhaustion (Noeske et al. 2007). A small fraction of galaxies exhibit quasi-exponential mass and SFR growth, either through major mergers or through strong bursts of star formation in the densest regions (Elbaz et al. 2011; Sargent et al. 2012). While typical galaxies therefore spend most of their time on the MS prior to additional quenching processes, these starburst galaxies are located above the MS and play a relatively minor role in the star formation history of the universe (Rodighiero et al. 2011). Galaxies located below the MS include quiescent galaxies (QGs), with spheroidal-like structures and little star formation activity, as well as fading SFGs with diminishing star formation activity. The transient galaxies, such as those in the green valley, can dominate the lower region of the MS. At $z < 1$, green valley galaxies are known to be off the MS (Schawinski et al. 2014), and they have intermediate

morphologies combining disk-dominated and bulge-dominated systems (Salim et al. 2009; Mendez et al. 2011; Pandya et al. 2017).

Star formation activities of galaxies are strongly correlated with morphologies (Cameron et al. 2011; Szomoru et al. 2011; Wuyts et al. 2011; Wang et al. 2012; Lee et al. 2013). Wuyts et al. (2011) investigated how the structures of galaxies depend on their location in the log(SFR)–log(M_*) diagram since $z \sim 2.5$, using large data sets from four different fields (COSMOS, UDS, GOODS—South and North); They found strong trends of specific star formation rate (sSFR = SFR/M_*) with galaxy morphology, represented by Sérsic index (n) (see also Whitaker et al. 2015). The galaxies on and above the main sequence (MS) mostly show exponential light profiles ($n \approx 1$) and have blue rest-frame colors, while relatively red galaxies reside below the MS and have "de Vaucouleur" (or similar) light profiles. However, most morphological studies on the MS have focused *only* on star-forming galaxies at $z > 1$ (Elbaz et al. 2011; Wuyts et al. 2011; Salmi et al. 2012; Whitaker et al. 2015), and do not account for how galaxy morphology of the entire population (including quiescent galaxies) differ throughout the log(SFR)–log(M_*) plane. Recently, Brennan et al. (2017) studied the structure of $z < 2.5$ galaxies all the way across and below the MS in CANDELS and a a semi-analytic model (SAM) of galaxy formation.

It is important to constrain the intrinsic shape of the MS for all galaxies across the log(SFR)–log(M_*) plane. Speagle et al. (2014) reported that the sample selection and other systematic uncertainties can significantly affect the slope of the MS through an extensive compilation of 64 measurements of the MS from 25 literature references using different SFRs, stellar masses, and different samples with different fitting methods out to $z \sim 6$. It is a general conclusion at all explored redshifts and masses that the MS has a constant dispersion of $\sim$0.3 dex. Furthermore, though it is well-known that the normalization of the MS increases with redshift, the derived single power-law slope is sensitive to the SFR indicators, sample selections, and initial mass function (IMF). Recently, several studies have found that the MS slope dramatically declines for massive galaxies at $z < 2$ (Karim et al. 2011; Whitaker et al. 2014; Lee et al. 2015; Schreiber et al. 2015; Tomczak et al. 2016); therefore a single power-law cannot explain the MS slope, and a more complicated formula is necessary. There is also evidence that the stellar mass above which the MS flattens evolves with redshift (Gavazzi et al. 2015; Lee et al. 2015; Tomczak et al. 2016). However, recently Renzini and Peng (2015) redefined the MS to be the main ridge line of the star formation peak in the three-dimensional SFR-mass-number space at $z \sim 0$ (i.e., the mode and not the mean/median). Even when removing the pre-selection of star-forming galaxies, they find that the best MS slope can be explained with a single power-law, without a bending of the MS at high masses. It is evident that the robust characterization of the MS with careful sample selections, accurate estimations of M_* and SFR, and better fitting methods are crucial.

A major complication in measuring the physical properties by fitting spectral energy distribution (SED) of galaxies at $z > 1$ is our inability to reliably constrain the star formation histories (SFHs). In general, it would be ideal to measure the real SFH of a galaxy, rather than assuming an analytic function for it. However, due to the complexity of the real SFH, the SED fitting depends on the SFH model with a simple functional

form. There are limitations in using SFH models—the degeneracy between SFHs and other properties of galaxies such as dust extinction, metallicity, and redshift, as well as the "outshining effect," where light from massive, young stars dominates the observed SEDs with significantly higher luminosities than older stellar populations. Despite these limitations, the most commonly used SFH model is an exponentially decreasing star formation history, or a τ-model. The properties of remote spheroidal quiescent galaxies and low redshift galaxies (including local spiral galaxies) are known to be reproduced well using the τ-model (Wuyts et al. 2009; Bell & de Jong 2000), because they clearly formed stars at a higher rate in their past than at the epoch of observation. However, using mock star-forming galaxies at $z > 2$, Lee et al. (2009) and Wuyts et al. (2009) showed that the τ-model cannot recover the intrinsic SFHs for star-forming galaxies. Nevertheless, many studies still use the τ-model for all galaxy types in the high-redshift universe for convenience, even though they do not necessarily show signs of star formation decline. Recently, several studies have argued, either with observations (Maraston et al. 2010; Papovich et al. 2011; Reddy et al. 2012; Pacifici et al. 2013) or with simulations (Lee et al. 2010; Pforr et al. 2012; Behroozi et al. 2013), that the increasing SFH is a more appropriate model for star-forming galaxies, especially at $z \gtrsim 2$. The basic conclusion of these SFH analyses is that various SFH models should be used to investigate diverse galaxy populations (Conroy 2013). In this regard, different SFH parameterizations are suggested (Lee et al. 2010; Behroozi et al. 2013; Simha et al. 2014; Cassará et al. 2016), but we still do not know what the intrinsic SFH of a galaxy is nor how complicated it is.

This paper is the first in a series of papers investigating the characteristics of star-forming galaxies located on, above, and below the MS and quiescent galaxies at $1.2 < z < 4$ selected from the CANDELS (PI: S. Faber, H. Ferguson). The primary goals of this study is to use an advanced SED fitting technique, SpeedyMC, a Markov Chain Monte Carlo (MCMC) code based on Bayesian statistics (Acquaviva et al. 2012), to obtain new measures of the integrated parameters of the galaxies' stellar populations (i.e., stellar mass, star formation rate, median-mass-weighted stellar age and dust obscuration, and study correlations with morphology). The novelty of our approach is that the star formation history of the galaxies is not set equal to an assumed function but rather is treated as a free "parameter," chosen from five simple models (constant, linearly increasing, delayed, exponentially decreasing, and increasing SFHs). We test the robustness of our measures, especially the SFR and the mean stellar age, against mock galaxies from SAM simulations, as well as with independent measures (SFR only). By adding the stellar age measures to the relation between morphology and the location of galaxies relative to the MS, we also investigate the evolution of galaxies and their quenching process. We also use various morphological diagnostics measured from the CANDELS/WFC3 H-band images, including parametric (Sérsic index, half-light radius), non-parametric (G and M_{20}) measures, and projected mass densities (Σ_{50} and Σ_1: see Section 5.2 for definitions). The second paper in this series will focus on the non-parametric measures and Σ_1 to explore the morphological transformation of galaxies as they evolve.

The structure of this paper is as follows. The optical and NIR data from CANDELS and the infrared data from *Herschel* and the sample selection used in this study are introduced in Section 2. In Section 3, the galaxy properties (stellar mass, age, and SFR) obtained using various SFH models with SpeedyMC are explained in detail, and the validation of the SED fitting results through comparisons with different SFR indicators and simulations are also found. With the robust estimation of M_* and SFR using the best-fit SFH, we investigate the MS in the log(SFR)–log(M_*) diagram in Section 4 and classify galaxies according to their positions relative to the MS. We then present an extensive morphological analysis associated with the location in the log(SFR)–log(M_*) plane using parametric (Sérsic index and half-light radius), non-parametric (G and M_{20}) measures, and projected mass densities in Section 5. The synthesis of morphological trends relative to the MS is presented in Section 6. We discuss our results in the context of quenching processes of galaxies in Section 7 and conclude with a summary in Section 8.

2. Data

All data used in this study are based on the WFC3/F160W (H-band) selected multi-wavelength catalogs from the CANDELS (Grogin et al. 2011; Koekemoer et al. 2011). We use CANDELS/ Deep fields (GOODS-S and -N) having deeper and fully panchromatic images relative to CANDELS/Wide fields (COSMOS, EGS, and UDS). The Deep fields cover about 130 square arc minutes and have a 5σ point source limiting depth of $H_{\rm AB} = 27.5$. The multi-wavelength photometry has been obtained using a software package with an object template-fitting method (TFIT, Laidler et al. 2007). This catalog includes photometry from the *HST*/ACS images in the BViz and F814W; from WFC3/IR images in the F098M (only in the GOODS-S), F105W, F125W, F160W; from VLT/VIMOS U and VLT/ISAAC Ks images; and from the *Spitzer*/IRAC images at 3.6, 4.5, 5.8, and 8.0 μm (GOODS-S from Guo et al. 2013 and GOODS-N from G. Barro et al. 2018, in preparation). We use CANDELS best estimated photometric redshifts (photo-z) measured for all galaxies by Dahlen et al. (2013), unless spectroscopic redshifts (spec-z) are available (about 6% of our sample).

In order to investigate the characteristics of IR detected galaxies among our sample, we use the public GOODS-*Herschel* DR1 catalogs in the GOODS-S and -N (Elbaz et al. 2011) and identify IR detected galaxies by matching the positions in both CANDELS and GOODS-*Herschel* catalogs. The source catalogs containing *Spitzer*/MIPS 24 μm, 70 μm (only GOODS-S) and *Herschel*/PACS 100 μm, 160 μm bands are used to compute total infrared luminosities in Section 3.1. *Herschel*/PACS flux densities and uncertainties are extracted from the PSF fitting using the *Spitzer*/MIPS 24 μm prior positions.

2.1. Sample Selection

The goal of this paper is to study galaxies at $1 \lesssim z \lesssim 4$, the peak epoch of the star formation (Madau & Dickinson 2014). We identify 23,580 galaxies at $1 \leqslant z < 4$ in the CANDELS portion of the GOODS-N and GOODS-S fields after limiting our sample to sources with H-band signal-to-noise ratio SNR(H) > 10. We also eliminated from the sample those galaxies for which the SExtractor PhotFlag and SpeedyMC quality flags revealed problems with the fitting procedures. SExtractor PhotFlag is used to designate suspicious sources that fall in contaminated regions (Guo et al. 2013). We only use

galaxies having PhotFlag = 0, indicating non-contaminated sources without detections of star spikes, halos, and bright stars, as well as excluding sources that are either artifacts or falling at the edge of the image. SpeedyMC quality flag is a warning sign, which represents the quality of the convergence of the MCMC chains. The quality flag is assigned using the length of the chain and the Gelman and Rubin "R" test (Gelman & Rubin 1992), which compares the variance of the mean within and between chains. If several long chains are present and $R - 1 < 1$, then flag = 1. If only one (long) chain is used, or if several chains are used, but there is a convergence problem ($R - 1 > 1$, common if there are multiple peaks), then flag = 2. If there are no long chains, then flag = 3. Following the definition of the quality flag, galaxies with flag = 3 are excluded in our final sample.

In this study, we separate star-forming galaxies from quiescent galaxies using the UVJ color–color selection. Previous studies have shown that the galaxy selection in sSFR can effectively discriminate between quiescent and star-forming galaxies (Karim et al. 2011; Lee et al. 2013). Because it might cause an artificially clean correlation between SFR and M_*, it is preferable to use a quiescent selection independent of SFR and/or M_*. Color–color selection has been widely used to classify quiescent galaxies out to $z \sim 3$ during the last decade (e.g., BzK by Daddi et al. 2007; Lee et al. 2013; e.g., UVJ by Williams et al. 2009; Brammer et al. 2011; Whitaker et al. 2011). Quiescent galaxies are characterized by red U–V colors and bluer V–J colors relative to star-forming galaxies having same U–V colors. In this study, we classify quiescent galaxies at all explored redshifts as

$$U - V > 0.88 \times (V - J) + 0.49,$$
$$U - V > 1.3, \quad V - J < 1.6. \tag{1}$$

Using slightly different definitions of quiescent galaxies is common in different surveys: while Whitaker et al. (2012) changed to a redshift independent rest-frame UVJ selection, Muzzin et al. (2013) adopt one that has weak redshift evolution, dating back to the original work of Williams et al. (2009). We use the definition of Schreiber et al. (2015) for all CANDELS fields up to $z = 4$. The rest-frame colors are measured using the EAZY software (Brammer et al. 2008), which performs a template-based interpolation of the observed photometry. We use the template set of Muzzin et al. (2013), using the Bessel filters in the optical and Palomar filters in the NIR. From Equation (1), we find that about 3% (29% for $M_* > 3 \times 10^{10} M_\odot$) galaxies are classified as quiescent galaxies.

We have studied the completeness of our sample as a function of the H-band limiting magnitude and surface brightness using the simulations by Guo et al. (2013), in which artificial galaxies with an exponential profile (Sérsic parameter $n = 1$) or De Vaucouleurs profile ($n = 4$) have been inserted into the H-band images and retrieved and analyzed with the same procedures as real galaxies. This analysis only tests for incompleteness in the detection process; our additional cut in H-band SNR ensures that the subsequent morphological analysis is likely to succeed for each detected galaxy. Figure 1 summarizes the results of the simulations and shows the 50%- and 80%-completeness curves in the half-light radius (R_e) versus H-band plane together with our sample, namely all galaxies with stellar mass $M_* > 10^9 M_\odot$ (see later). Star-forming galaxies are shown in blue and passive ones in red.
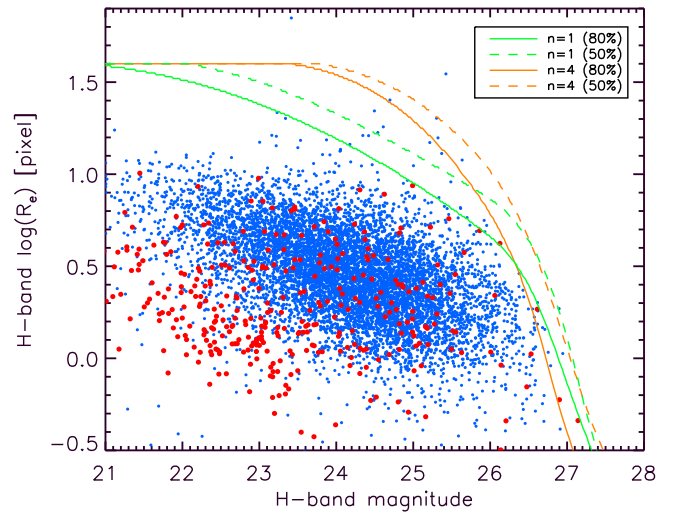

Figure 1. Completeness curves for the CANDELS GOODS H-band images in the GOODS-S fields from the Monte Carlo simulations by Guo et al. (2013) plotted against our sample in the half-light radius (R_e) vs. H-band mag plane. Blue and red points represent UVJ selected star-forming and quiescent galaxies, respectively. Both 50% (dashed) and 80% (solid) completeness curves are shown for two morphological types, the exponential disk (Sérsic $n = 1$) and the De Vaucouleurs spheroid ($n = 4$) with green and orange lines, respectively. About two dozen galaxies are outside the 80% curve of disks and about one dozen outside the same curve for spheroids, suggesting that our sample is about 80% complete at all redshift and stellar mass that we have considered.

Except for about two dozen galaxies who are outside the disk 80% curve and for one dozen galaxies which are outside the spheroid 80% curve, the rest of the sample is located within the 80% disk. This leads us to conclude that the sample is at least 80% complete at all redshift and stellar mass considered here, and that incompleteness is not likely to affect any of our conclusions.

Lastly, $\sim$1.5% of our sample are known X-ray, IR, and radio AGN candidates among our final sample (GOODS-S: Xue et al. 2011 [X-ray], Padovani et al. 2011; Donley et al. 2012 [IR]; GOODS-N: Alexander et al. 2003 [X-ray]). Most of these AGN candidates (87%) are classified as star-forming galaxies from the UVJ diagram, and about half of them are IR detected galaxies. Although our FIR measurements can be polluted by the light of dust-obscured AGN, we do not exclude AGN candidates from the further study because inclusion of them does not significantly change our results.

3. SED Fitting Allowing Various Star Formation Histories

We have investigated how the choice of star formation history affects the behavior of the spectral energy distribution (SED) fitting by comparing galaxy properties obtained using five commonly used star formation history (SFH) models: linearly increasing, constant, delayed (linearly increasing at early time, then exponentially decreasing after $t = \tau$), exponentially decreasing (τ-model), and exponentially increasing (inverted τ-model) SFHs (see Table 1 for definitions of SFH models). SEDs are fit with SpeedyMC (Acquaviva et al. 2012) to measure the properties of stellar populations including stellar mass, age, dust reddening, and star formation rate. SpeedyMC is an updated version of GalMC, which is a publicly available Markov Chain Monte Carlo (MCMC) code for the SED fitting based on Bayesian statistics (Acquaviva et al. 2011). In SpeedyMC, the model spectra are computed

Table 1
Definitions of Five SFHs

SFH	Definition
Linearly increasing SFH (LinInc)	$SFR(t) \propto t$
Constant SFH (CSF)	$SFR(t) = \text{constant} \propto \text{galaxy mass/age}$
Delayed SFH (Delay)	$SFR(t) \propto \frac{t}{\tau^2} e^{(-t/\tau)}$
Exponentially decreasing SFH (Tau)	$SFR(t) \propto \frac{1}{\tau} e^{(-t/\tau)} \ (\tau > 0)$
Exponentially increasing SFH (InvTau)	$SFR(t) \propto \frac{1}{\tau} e^{(-t/\tau)} \ (\tau < 0)$

Note. $SFR(t)$ is the instantaneous star formation rate and the star formation timescale, τ, is the free parameter during the SED fitting, ranging from 0.1 to 5 Gyr.

once at a grid of locations exploring the entire parameter space. Then, the MCMC exploration of the parameter space is carried out, but a multi-linear interpolation between the pre-computed spectra is used to compute the model SED at each step.

One of the advantages of MCMC technique is that it provides posterior distributions of the galaxy properties estimated from the code, allowing an accurate computation of expectation values and confidence intervals, even in the case of non-Gaussian probability distribution functions. As a final output, we adopt the mean values computed from the posterior distribution. In most cases, the mean and the best-fit values are close, especially when the posterior distribution is approximately Gaussian. However, the best-fit values are not meaningful when the probability distribution is skewed or broad. In a case of bimodal distributions, the mode of the probability distribution would be a better estimate than the mean. But we find that less than 3% have bimodal distributions in any SFHs and that the differences between mode and mean values of the bimodal distributions are not significant.

We fit the CANDELS multi-band photometry to the Bruzual and Charlot (2003) (BC03) spectral population synthesis library, with a Chabrier initial mass function (IMF) and metallicity fixed to the solar value. The Calzetti law (Calzetti et al. 2000) is used for the dust obscuration model, together with the Madau prescription for the opacity of intergalactic medium (IGM) (MAdau 1995). Redshifts are fixed to the CANDELS photo-z (or spec-z if available) during the fitting. We include the flux from the nebular continuum and line emission by tracking the number of Lyman-continuum photons and by assuming case B recombination. We then model the empirical line intensities relative to $H\beta$ for H, He, C, N, O, and S lines as a function of metallicity according to the prescription in Anders and Fritze-v (2003) and Schaerer and de Barros (2009). SpeedyMC performs the SED fitting on the three (or four) dimensional parameter space defined by stellar mass, age, dust extinction, and e-folding time, τ (in the case of τ-related SFHs). We define the stellar age as the median stellar mass-weighted age of the galaxy (i.e., the lookback time in which 50% of the stellar mass has been built). Dust extinction (reddening) is parameterized by the color excess, $E(B–V)$, assuming the Calzetti dust absorption law. Overall, our

procedure is conceptually similar to that of Pforr et al. (2012) and Maraston et al. (2010) to study galaxies at $1.4 < z < 2.9$, the key differences being that they used the stellar population models by Maraston (2005) and did not include the nebular emission. Our work also considers a wider choice of SFH and takes advantage of the broader wavelength coverage and deeper sensitivity of the CANDELS/Deep survey.

We present the best-fit star formation history (Best Fit SFH) of individual galaxies determined by the maximum likelihood obtained from the SpeedyMC. Figure 2 depicts the fraction of galaxies having the Best Fit SFH as one of five SFHs. Most of the quiescent galaxies classified from the rest-frame UVJ diagram are best-fit with decreasing SFHs, either Delay or Tau SFHs. A total of 47% of SFGs are also best-fit with decreasing SFHs, and the rest of them with increasing SFHs (LinInc, CSF, and InvTau). For SFGs at high redshift, Delay and InvTau SFHs have been suggested as more suitable functional forms than the Tau (Delay: Lee et al. 2010; Speagle et al. 2014; InvTau: Maraston et al. 2010; Pforr et al. 2012). However, we show here that they are not the preferred SFH in the SED fitting of SFGs at $1 < z < 4$. Only 5.7% and 1.1% of SFGs have the Delay and InvTau as the Best Fit SFH, respectively. As we will further demonstrate in Sections 3.1 and 3.2, our results suggest that using only one SFH for all galaxies is not necessarily the correct approach.

3.1. Comparison of SFRs with Various SFR Indicators

Without dust extinction, SFR estimated from rest-frame UV light is more sensitive than SFR estimated from IR or radio data by orders of magnitude because it originates mainly from young, massive stars (Madau & Dickinson 2014). However, most energy radiated by young stars is heavily obscured by dust at least out to $z = 2.5$; Whitaker et al. 2017 showed that >50% of star formation is obscured at $\log(M_*/M_\odot) > 9.4$(see also, e.g., Magnelli et al. 2009; Murphy et al. 2011; Bourne et al. 2016). Since IR emission represents re-emitted UV emission from completely dust-obscured stars, correctly estimated total IR luminosity (L_{IR}^{tot}) is a key to measuring the actual SFR of distant galaxies. Currently, *Herschel* observations enable us to *directly* measure re-processed star light, and hence the total bolometric IR luminosity of individual massive galaxies. But a significant fraction of SFGs are missed at $z > 1$ and far-infrared (FIR) luminosity is limited to the brightest galaxies because of the sensitivity limit of *Herschel* (Elbaz et al. 2011). In the absence of FIR data, various SFR indicators have been used to *indirectly* estimate the dust attenuation of individual galaxies (Daddi et al. 2007; Karim et al. 2011; Lee et al. 2011; Sobral et al. 2012; Arnouts et al. 2013).

The total SFR, adding SFR from IR and UV emission, might be the best indicator of SFR for SFGs because it combines the light from the unobscured stars (UV) and that which is re-processed by dust (IR). In Figure 3, we compare four different SFR measurements to total SFR, SFR($UV_{FUV} + IR$), for 2,006 SFGs that have 24 μm and/or *Herschel* detections at $1 < z < 3$ and $\log(M_*/M_\odot) > 9$. We only use galaxies at $z < 3$ due to the sensitivity limits of the GOODS-*Herschel* observations (Elbaz et al. 2011). Here are the definitions of each SFR we use in this analysis:

1. *Instantaneous SFR*: The instantaneous SFR obtained from the SED fitting, including prescriptions of dust obscuration, is commonly used for galaxies lacking
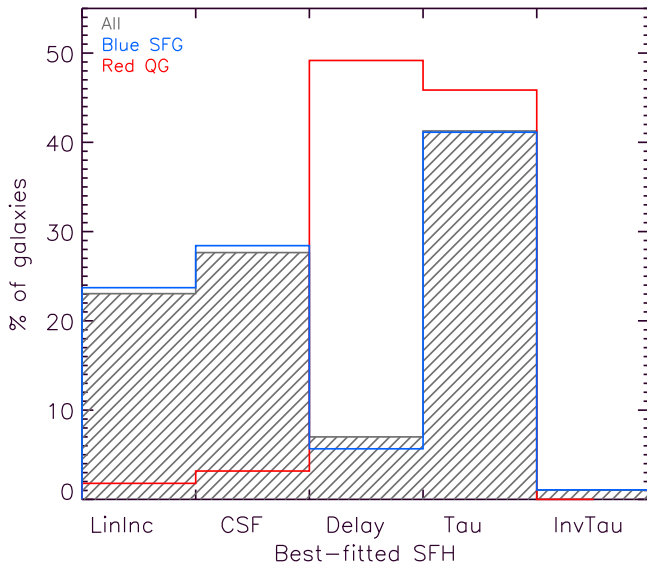
Figure 2. Histogram of the percentage of galaxies having the Best Fit SFH as linearly increasing SFH (LinInc), constant SFH (CSF), delayed model (Delay), τ-model (Tau), and inverted-τ model (exponentially increasing SFH; InvTau). The gray shaded histogram represents all galaxies, whereas blue and red are for rest-frame UVJ selected SFGs and QGs. The SEDs of most of the QGs are best-fit using decreasing model such as delayed and τ-models, while SFGs have various SFHs.

spectroscopic star formation tracers. However, it is strongly dependent on the choice of SFH (Maraston et al. 2010). In this study, the SFR is obtained from the best-fit SED, assuming the Best Fit SFH for each galaxy. For comparison, we also show the instantaneous SFR obtained using the τ and inverted-τ models.

2. *SFR from dust-corrected UV emission*: The dust-corrected UV SFR, $SFR(UV_{cor})$, is computed using the conversion factor by Conroy et al. (2009) with an assumption of the Chabrier IMF,

$$SFR\,(UV_{cor})\,[M_\odot/yr] = 0.82 \times 10^{-28} L_{1500}(erg/s/Hz). \quad (2)$$

We adopt the empirical correlation between dust obscuration and the slope of the rest-frame UV of starburst galaxies (Meurer et al. 1999; Calzetti et al. 2000) to derive the dust-corrected UV luminosity at the rest-frame 1500 Å(L_{1500}), and subsequently $SFR(UV_{cor})$.

3. *Total SFR.* This SFR is a combination of light from both the UV and IR, $SFR_{tot} = SFR(UV_{FUV}) + SFR(IR)$ (Madau & Dickinson 2014). SFR(IR) is defined as

$$SFR_{IR}[M_\odot/yr] = 1.09 \times 10^{-10} L_{IR}(L_\odot), \quad (3)$$

where L_{IR} is the total infrared luminosity, $L(8–1000\,\mu m)$. We measure L_{IR} by fitting the mid- or far-infrared SED with IR templates for high-redshift SFGs ($0.5 < z < 3$) introduced by Kirkpatrick et al. (2015). We use a maximum of three bands $70\,\mu m$ from *Spitzer*/MIPS, $100\,\mu m$, and $160\,\mu m$ from *Herschel*/PACS, if available. For galaxies only having $24\,\mu m$ *Spitzer*/MIPS observation, we use $24\,\mu m$ to compute L_{IR}. The far-UV (FUV) components of star formation is derived from the observed FUV luminosity at 1500 Å with no correction for extinction, and the $SFR(UV_{FUV})$ is subsequently estimated using the conversion factor by Conroy et al. (2009). The overall

conversion factor of the FUV and IR contribution assumes the Chabrier IMF.

In Figure 3, we use the Pearson correlation coefficient (ρ), the average ($\langle\Delta SFR\rangle$), and the mean absolute deviation (σ) of the differentiation of SFRs to test correlations between the different SFR estimates. The SFRs obtained using the inverted-τ model show the best correlation with $SFR(UV_{FUV} + IR)$; these models have the largest ρ (0.63), smallest $\langle\Delta SFR\rangle$ (0.04), and lowest σ (0.36). However, despite these statistics, we note that only 1.1% of SFGs are formally best-fit with an inverted-τ model. We also find that SFRs obtained using the Best Fit SFH have a similarly large ρ (0.59), only a modest offset in $\langle\Delta SFR\rangle$ (0.16), and relatively small σ (0.30) when compared with results obtained using the τ-model or dust-corrected UV SFR. This implies that the SFRs obtained using the Best Fit SFH are better correlated with total SFRs relative to the individual SFHs. Furthermore, we propose that the Best Fit SFH of each galaxy is a robust approach that yields more accurate SED-derived SFRs for the overall galaxy population.

3.2. Validation with Simulated Galaxies

Next we test how well we can recover the various best-fit galaxy properties from SpeedyMC, in particular the SFH, stellar age, SFR and stellar mass, by using a sample of artificial galaxies created using simulations of CANDELS light cones (R. S. Somerville et al. 2018, in preparation), based on a combination of the ROCKSTAR halo catalogs by Behroozi et al. (2013) extracted from the Bolshoi dark matter N-body simulations of Klypin et al. (2011), together with the semi-analytic models (SAMs) of Somerville et al. (2012), dubbed the "Santa Cruz models." The SAMs implement gas cooling, star formation, and the growth of supermassive black holes, as well as including the effects of merging, stellar-driven winds, and black hole feedback. The synthetic magnitudes of the galaxies are computed using BC03 models convolved with the star formation history and chemical enrichment evolution of each galaxy as predicted by the SAM, assuming a Chabrier IMF. The Santa Cruz models implement the effects of dust based on a two-component model of the extinction (Charlot & Fall 2000), including diffuse cirrus in the disk and the dense birth clouds surrounding new stars. To derive the actual extinction, a "slab" model is used to compute the inclination dependent extinction (see Somerville et al. 2012 for further details). The total amount of energy absorbed by the dust is assumed to be re-emitted in the IR using the templates of Chary and Elbaz (2001) to determine the SEDs of the dust emission.

Specifically, for our test of SpeedyMC, we use the CANDELS/GOODS-S mock catalog, from which we have randomly extracted 1000 galaxies with the same selection criteria we have used for the observed galaxies in Section 2, redshift in the range $1 < z < 4$, stellar mass $>10^9\,M_\odot$. To estimate the photometric errors in each band for a simulated galaxy, we extract a random Gaussian variable using median errors and scatters of each observed band in the GOODS-S field. We then use them as the photometric errors of simulated galaxies in this MOCK catalog and run SpeedyMC for those 1000 galaxies. True synthetic fluxes and the randomly extracted photometric errors are being used as input into SpeedyMC. Note that, in principle, it is suggested to perturb the synthetic fluxes by some photometric errors to properly simulate observed fluxes of galaxies. However, this only
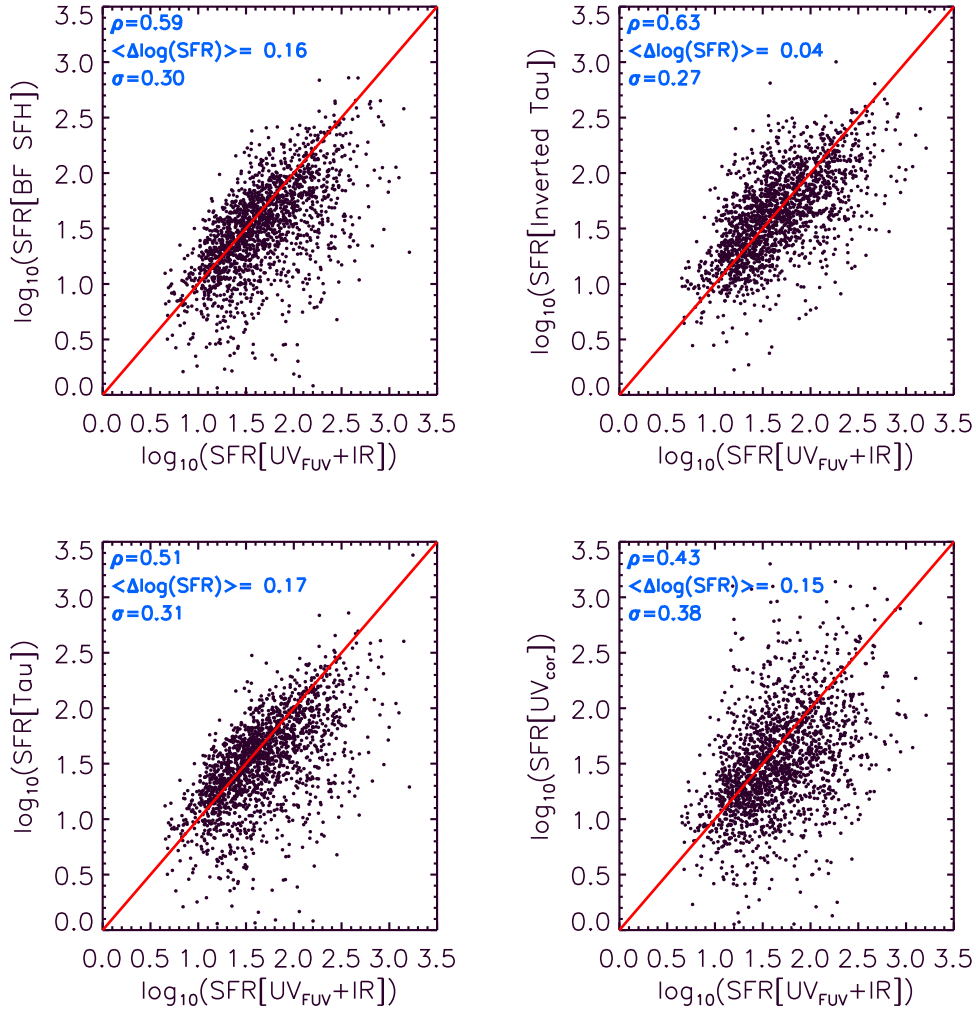
Figure 3. Comparison of total SFRs for IR detected SFGs with SFRs obtained using the Best Fit SFH (BF SFH), τ, inverted-τ models, and dust-corrected UV SFR. The red line is for the one-to-one correlation. ρ, $\langle\Delta\text{SFR}\rangle$, σ are the Pearson correlation coefficient, average and mean absolute deviation (MAD) of differences of log (SFR), respectively. When ρ is close to unity, SFRs in x- and y-axes are linearly correlated, and as $\langle\Delta\text{SFR}\rangle$ and σ are close to zero, SFRs in x- and y-axes are identical. Even though statistics indicate that the SFR obtained using the inverted-τ model shows the best correlation with SFR(UV$_{\text{FUV}}$+IR), the relatively good correlation between SFR obtained using the Best Fit SFH and SFR(UV$_{\text{FUV}}$+IR) are also shown in this comparison.

slightly increases the observed scatters in Figures 4–7 and leaves the qualitative results unchanged.

After excluding 32 galaxies that have SpeedyMC quality flag = 3, we compare the "observed" output parameters from the Best Fit SFH and five SFHs (age, stellar mass, and SFR) with the input values from the mock catalog. We do not perform a detailed comparison of the Best Fit SFH with the intrinsic one because, in general, the latter is rather different from our simple five analytic functions and the focus of this paper is not on the reconstruction of the SFH of the galaxies. Rather, we use the comparison of the derived stellar age, M_*, and SFR with the intrinsic values to quantify the effectiveness of the fit, including the determination of an approximate simple SFH that is capable of returning robust measures of SFR and stellar age.

We first consider the stellar age, as this is the parameter that most directly relates to the SFR. We initially considered two estimators of the stellar age, the age since the onset of star formation(Age_O), and the median stellar mass-weighted age (Age_M). After verifying that Age_M correlates with intrinsic age from the MOCK significantly better than Age_O (smaller scatters in all cases of SFHs), however, we have used the median stellar

mass-weighted age for subsequent analysis. In Figure 4, we show the comparison of the input Age_M in the case of the Best Fit SFH (bottom right panel) relative to when the SFH is forced to be only one of the five analytical models. Red circles and orange squares represent quiescent galaxies (QGs) selected from different definitions. Normally the dividing cut used for observed galaxies does not work well for model galaxies, because the distribution of specific star formation rates (and the distribution of galaxies on the color–color diagram) in the model is not bimodal. Thus we cannot apply the same UVJ color–color selection to the model galaxies. Brennan et al. (2015) defined the quiescent galaxies as having less than 25% of the sSFR of the main-sequence (MS) line for both observations (CANDELS) and model galaxies (SAMs). Adopting their definition, we separate quiescent galaxies from star-forming ones based on their distances from the MS, defined as $R_{\text{SB}} = \text{sSFR}/\text{sSFR}$ of the MS (Elbaz et al. 2011; see Figure 7 for the MS slope estimation of mock galaxies). Two QG selection cuts used here are (1) $R_{\text{SB}} < 0.25$ from Brennan et al. (2015) (red circles) and (2) $R_{\text{SB}} < 1/30$ from Section 4.2 in this study (orange squares). As a result, we classify 150 and 33 quiescent galaxies among 968 mock samples, respectively.
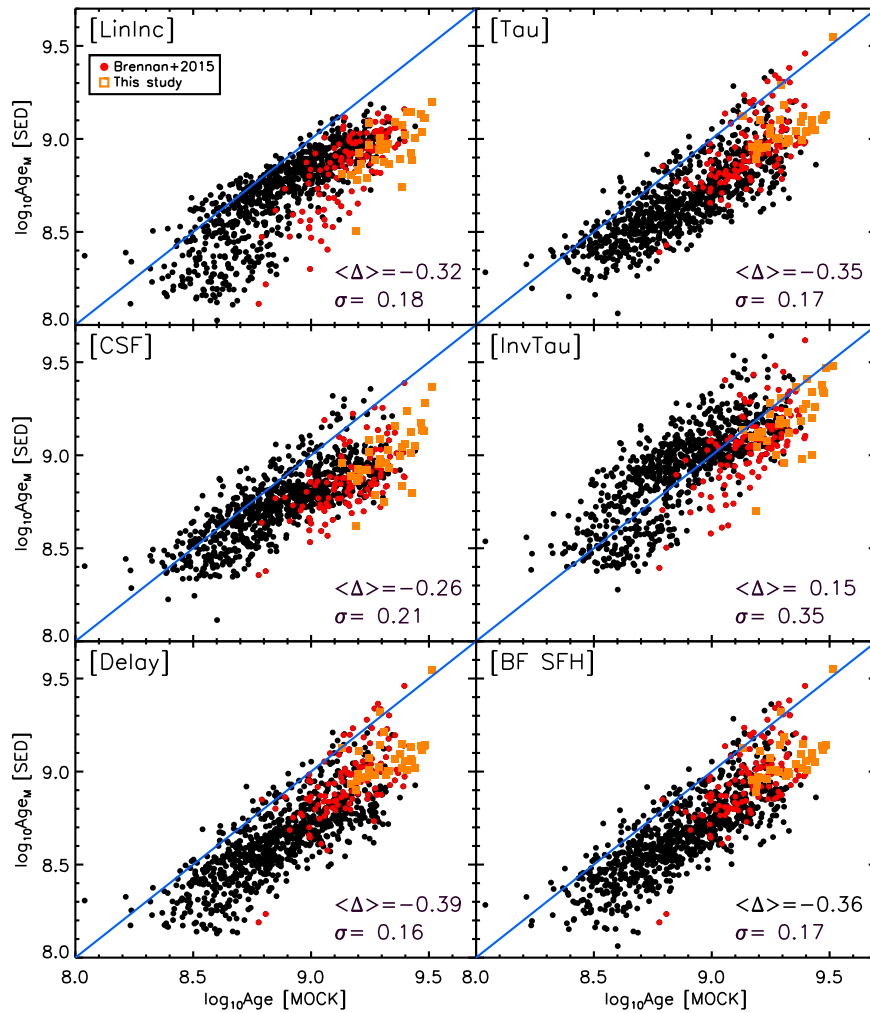
Figure 4. Comparison of median stellar-mass-weighted age (Age$_M$ [SED]) obtained from SpeedyMC to the intrinsic age from the simulation (Age[MOCK]) for mock galaxies. Blue lines indicate a linear correlation. $\langle\Delta\rangle$ and σ are the mean and mean absolute deviation of (Age$_{derived}$−Age$_{intrinsic}$)/Age$_{intrinsic}$, respectively. Quiescent galaxies are classified as galaxies having $R_{SB} < 0.25$ (red circles, 150 galaxies), following the definition from Brennan et al. (2015), and $R_{SB} < 1/30$ (orange squares, 33 galaxies), from this study (see Section 4.2). Based on $\langle\Delta\rangle$, ages obtained using InvTau are the closest to the intrinsic absolute ages, while the deviations (σ) are the largest. Though the relative ages are generally robust, all models underestimate the absolute ages.

In Figure 4, there is a clear correlation between the input and output age, irrespective of the adopted SFH. The robustness of the measure, however, varies with the SFH and with galaxy type, namely SFGs (black points) or QGs (red and orange points). In all cases, the ages of QGs are underestimated by ∼0.1–0.4 dex. Forcing the SFH to the Lininc, Constant or InvTau results in larger scatters to both SFGs and QGs, and even worse for QGs. This is not surprising, as these adopted SFHs are not typical of QGs. While the InvTau model produces stellar mass-weighted ages for SFGs that are closest to reality (i.e., closest in absolute age), there is a significantly larger scatter. Apparently, the ages derived with the Tau, Delay, and Best Fit SFHs perform better, preserving the relative age of both QGs and SFGs. We cannot differentiate between the overall quality of Age$_M$ from these three SFHs, as they all have similar order offsets in terms of absolute age and a small intrinsic scatter. The range of recovered age versus input age is located parallel to but downshifted by ∼0.5 dex relative to the diagonal line (where recovered age equals input age). In other words, while we can robustly recover the relative ages, we underestimate the absolute age by a constant amount (in log-log scale). It may be that this systematic offset relative to the

absolute age is due to our simplifying assumption that the metallicity is fixed to a constant value during the fit. However, one could use the results of these comparisons with simulated galaxies, where we know "truth," to correct to the absolute ages. In this work, we are not so much interested in the absolute age dating of the galaxies as we are in the relative ones. We therefore proceed estimating age differences adopting the mass-weighted age estimated by the Best Fit SFH for the analysis of the real data.

Next, we consider how well we can recover the stellar mass of galaxies using the various SFHs. In Figure 5, we compare the measured stellar mass of the simulated galaxies for each of the five SFHs and the Best Fit SFH relative to the input values. This comparison confirms what has been found in many previous studies: the stellar mass is the most robust recovered parameter by SED fitting procedures (e.g., Muzzin et al. 2009; Lee et al. 2010; Santini et al. 2015), and it is largely degenerate to the assumptions of SFH. We do observe that stellar masses of both SFGs and QGs are nicely recovered by the SED fit, while there is a systematic bias toward large value of ∼0.2 dex or less; this result is largely independent of the adopted SFH. The independence of the measured stellar mass from the
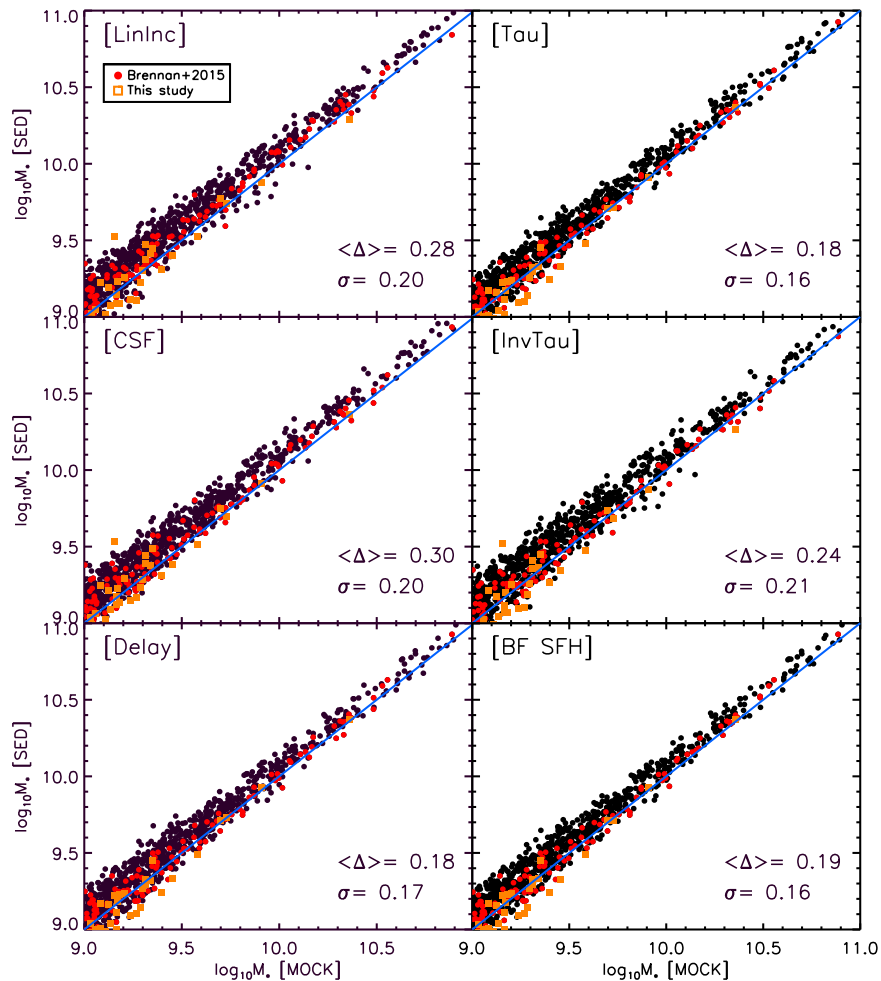
Figure 5. Comparison of stellar masses (M_* [$M_\odot$]) obtained from SpeedyMC relative to simulation, with red and orange points representing QGs classified using different definitions (Brennan et al. 2015 and this study, respectively) and black points SFGs. The M_* obtained using five SFHs strongly correlates with the intrinsic M_*, indicating that the stellar mass estimation is insensitive to the assumed SFH and galaxy types (i.e., SFGs and QGs). Generally, the derived stellar mass overestimates the intrinsic stellar mass about ~0.2 dex (or less).

assumed SFH for the simulations is also clearly observed in the case of real galaxies, for which the stellar masses for each assumed SFH are compared against each other (full discussion forthcoming in B. Lee et al. 2018, in preparation).

Figure 6 shows that the star formation rate, on the other hand, does indeed depend on the assumed SFH. We also see this result evidently from our comparison of the measurements of real galaxies for each the five SFHs considered relative to each other. For the simulations, the recovered SFR assuming LinInc, CSF, and InvTau tends to overestimate the intrinsic values, with the largest deviations occurring at the low end of the SFR distribution for both SFGs and QGs. Similar to the age measurements, the best measures are obtained by assuming the Tau, Delay, or Best Fit SFH, with Tau being the best of the three. It is interesting to note that the SFRs of QGs are generally overestimated for all SFHs, with increasing SFHs showing the largest deviations. These are the same galaxies that are forced to rely on SED SFRs, as they are far below the detection limits of the deepest existing IR surveys. While the FUV+IR SFRs are generally considered robust for SFGs, they are likely upper limits for QGs. For example, the *Spitzer*/MIPS 24 μm calibrations tend to overestimate the SFRs for galaxies with logsSFR < -10 yr^{-1} (e.g., Fumagalli et al. 2014; Hayward et al. 2014; Utomo et al. 2014). The results here

suggest that SED SFRs also tend to overestimate the SFRs for this same population of galaxies.

As a final test, we evaluate the ability of our SED fitting procedure to reconstruct the distribution of the mock galaxies in the log(SFR) versus log(M_*) plane. In Figure 7, we plot the log(SFR)–log(M_*) diagram using intrinsic values from the mock catalog (left panel) and derived values assuming different SFHs (right panel). The red lines in the left panel represent different QG selection cuts: dashed, $R_{SB} < 0.25$ (Brennan et al. 2015), and dotted, $R_{SB} < 1/30$ (this study), respectively. We then measure the main sequence (MS) using an Equation (4), where the MS slope of the intrinsic values (orange) is about unity below the turnover mass (~10^{10} $M_\odot$) and becomes flatter (about 0.32) at larger mass, and the blue lines are the best-fit slopes for each respective SFH. Apparently, the MS slopes using Tau and Delay SFHs are close to the intrinsic slope (orange) with a bended MS, even though the turnover mass is slightly larger (~$10^{10.3}$ $M_\odot$). When factoring in the dispersion in addition to the marginal differences in slope and normalization, it becomes clear that the intrinsic properties of the MS are best recovered when assuming the Tau and Delay SFHs. In cases of LinInc, CSF, and InvTau, the MS slope is rather explained by a single power-law (linear fit), and the galaxy distribution in the log(SFR) and log(M_*) plane is totally
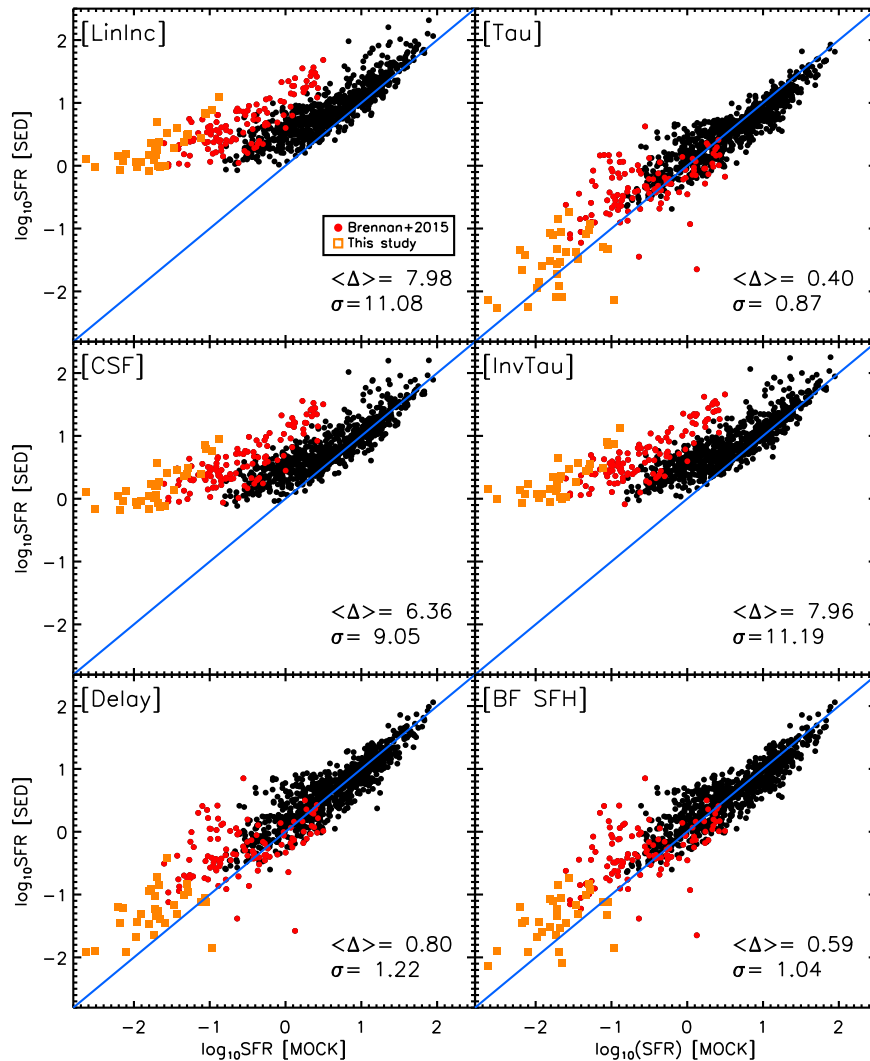
Figure 6. Comparison of SFRs obtained from SpeedyMC relative to simulations, with red and orange points representing QGs classified using different definitions (Brennan et al. 2015 and this study, respectively) and black points SFGs. SFRs obtained using Tau show the best correlation with intrinsic SFRs for both the mock SFGs and QGs.

different from the intrinsic one. As expected, the SFRs of QGs are drastically overestimated when using increasing SFHs (LinInc, CSF, InvTau); the properties of QGs cannot be recovered when adopting these SFHs. It appears that the different SFH clearly affect the scatter in the log(SFR) and log(M_*) relation.

The correlation between log(SFR) and log(M_*) using the Best Fit SFH (last plot in the right panel) are similar to ones using Tau and Delay SFHs because most of galaxies have these decreasing SFHs as their Best Fit SFH. While adopting the Tau SFH in particular is not a poor choice overall, the comparisons with the simulation further support our results in Section 3.1 that the Best Fit SFH better constrains the intrinsic galaxy properties relative to those obtained using one simple SFH. In particular, we find significant systematic biases in the overall population when adopting the CSF, LinInc, or InvTau SFHs.

4. log(SFR)–log(M_*) Diagram at $1.2 \leqslant z < 4$ in CANDELS

We now explore the main sequence of star formation (MS) at $1.2 \leqslant z < 4$ using the robust estimate of stellar masses and SFRs of galaxies in CANDELS. For our analysis of galaxies

in the log(SFR) and log(M_*) plane, we use 9,888 galaxies at $1.2 \leqslant z < 4$ after limiting our sample with stellar mass, $M_* > 10^9 \, M_\odot$ (over 80% completeness limit as shown in Figure 1). Among them, about 17% have IR detections. The rest-frame UVJ diagrams in four redshift bins with $\Delta t \sim 1$ Gyr are shown in Figure 8. Using Equation (1) in Section 2.1, we distinguish about 6% quiescent galaxies from our galaxy sample at $1.2 \leqslant z < 4$. The fraction of quiescent galaxies is mass-dependent. Above a stellar mass limit of $10^9 \, M_\odot (3 \times 10^{10} \, M_\odot)$, the quiescent fraction varies from 9% (27%) at $1.2 < z < 1.5$ to 2.6% (30%) at $2.8 < z < 4$.

4.1. The Main Sequence of Star Formation

Figure 9 illustrates log(M_*) as a function of log(SFR), sliced into four redshift bins (where each bin has $\Delta t \sim 1$ Gyr). Red and black points represent QGs and SFGs classified via rest-frame UVJ colors (Figure 8), respectively. We use the SFR(UV$_{FUV}$ + IR) for IR detected galaxies (green) at $1.2 < z < 3$ and the SFR obtained using the Best Fit SFH for the rest of non-IR detected galaxies. Stellar mass is
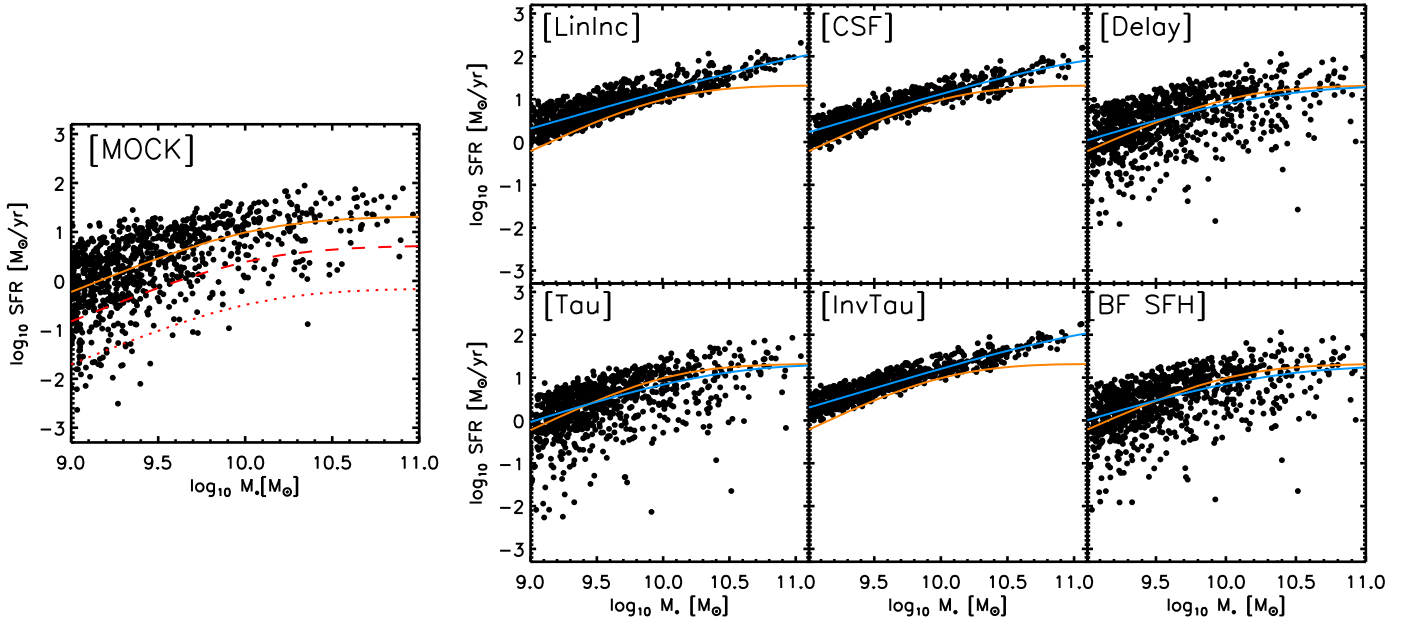
Figure 7. log(SFR) vs. log(M_*) of simulated galaxies from the CANDELS/GOODS-S mock catalog. Left: SFR and M_* are intrinsic values from the mock catalog. The fit of the MS is shown as orange line and the slope is about 1.1 below the turnover mass ($\sim 10^{10}\,M_\odot$) and 0.32 above the turnover mass. The red dashed line represents $R_{SB} = 0.25$ and the red dotted line is for $R_{SB} = 1/30$. Galaxies below these lines are considered as quiescent galaxies in Brennan et al. (2015) and this study (see Section 4), respectively. Right: SFR and M_* are obtained using five SFHs and the Best Fit SFH (BF SFH) and the blue lines are the derived MS slopes. The intrinsic MS slope (orange) is overplotted for a comparison. The MS slope using Delay and Tau, and Best Fit SFH, are close to the intrinsic slope, indicating that intrinsic properties are best recovered when assuming those SFH models.

<div align="center">

Table 2
First Column: The Number of SFGs (IR Detections) and QGs

</div>

	# of SFGs (IR) /QGs	M_0	β_1 $(M < M_0)$	β_2 $(M > M_0)$	σ of MS/IQR of MS
$1.2 \leqslant z < 1.5$	1424 (367) /112	10.09	1.08 ± 0.06	0.18 ± 0.03	0.35 / 0.37
$1.5 \leqslant z < 2$	2442 (637) /183	10.67	0.84 ± 0.04	0.28 ± 0.11	0.40 /0.49
$2 \leqslant z < 2.8$	3318 (537) /129	11.18	0.86 ± 0.03	$\cdots$	0.37 /0.40
$2.8 \leqslant z < 4$	2222 (68[a]) /56	11.35	0.78 ± 0.07	$\cdots$	$0.58(0.47)^{[b]}$ /$0.77(0.64)^{[b]}$

Notes. Second column: turnover mass, M_0. Third and fourth column: β_1 and β_2 are the MS slope below and above the M_0, respectively. Fifth column: σ is the mean value of the $\log_{10}$(SFR) dispersions (IQR: inter-quartile range).
[a] Note again that we do not include IR detected galaxies at $z > 3$.
[b] The number in the parenthesis indicates a σ(or IQR) of the MS excluding the highest mass bin having the largest SFR dispersion with only five galaxies.

measured using the Best Fit SFH as well. Orange points and error bars represent the mean and dispersion of SFRs of SFGs distributed in a stellar mass bin, $\Delta = 0.3$ dex, computed using bisquare weighting. A tight main sequence of SFGs exists at all explored redshifts. To parameterize the main sequence, we fit the mean $\log(M_*)$ and $\log$(SFR) at each redshift bin with a polynomial model provided by Lee et al. (2015),

$$S = S_0 - \log\left[1 + \left(\frac{10^M}{10^{M_0}}\right)^{(-\gamma)}\right], \qquad (4)$$

where $S = \log$(SFR) and $M = \log(M_*/M_\odot)$. γ is the power-law slope at lower stellar masses, and S_0 is the maximum value of $\log$(SFR) that the function is asymptotically approached at

higher stellar masses. In particular, we use this model to quantify the turnover mass, M_0, which is a break of the power-law slope (for a detailed explanation of the model, see Section 4.1 of Lee et al. 2015). The mean SFR in each mass bin is plotted with a MS fit and M_0 in the last panel of Figure 9. In agreement with earlier studies, we show that there is a break of the MS at M_0 (Whitaker et al. 2014; Lee et al. 2015) and observe an evolution of M_0 to larger values with increasing redshift (Schreiber et al. 2015; Tomczak et al. 2016). A broken power-law is used to measure the best-fit MS slope below and above the M_0. The MS slope measurements are listed in Table 2. While the slope is nearly unity ($\beta_1 \sim 0.85$–1.0) below the turnover mass, it becomes flatter ($\sim 0.2 - 0.3$) above M_0 at
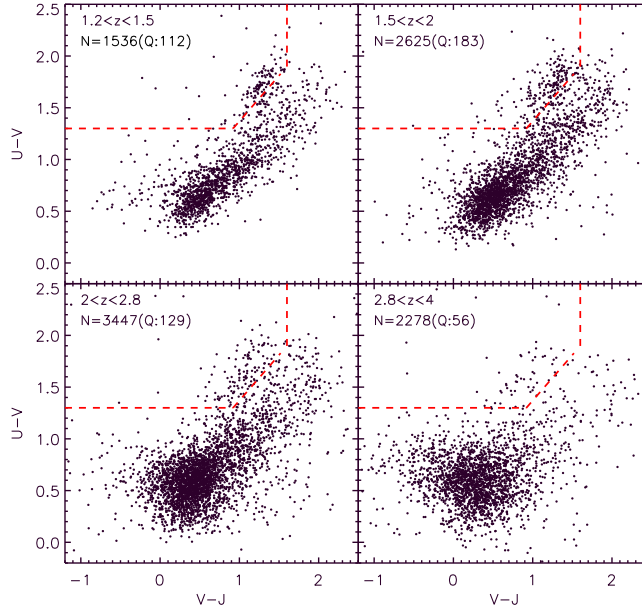
Figure 8. Rest-frame U–V vs. V–J color diagrams at four redshift bins ($\Delta t \sim 1Gyr$), $1.2 < z < 1.5$, $1.5 < z < 2$, $2 < z < 2.8$, $2.8 < z < 4$. Red quiescent and bluer star-forming galaxies are classified by their rest-frame (*U–V*) and (*V–J*) colors with Equation (1) (red dashed line). The number indicates the total number of galaxies included in each redshift bin (Q stands for the number of quiescent galaxies).
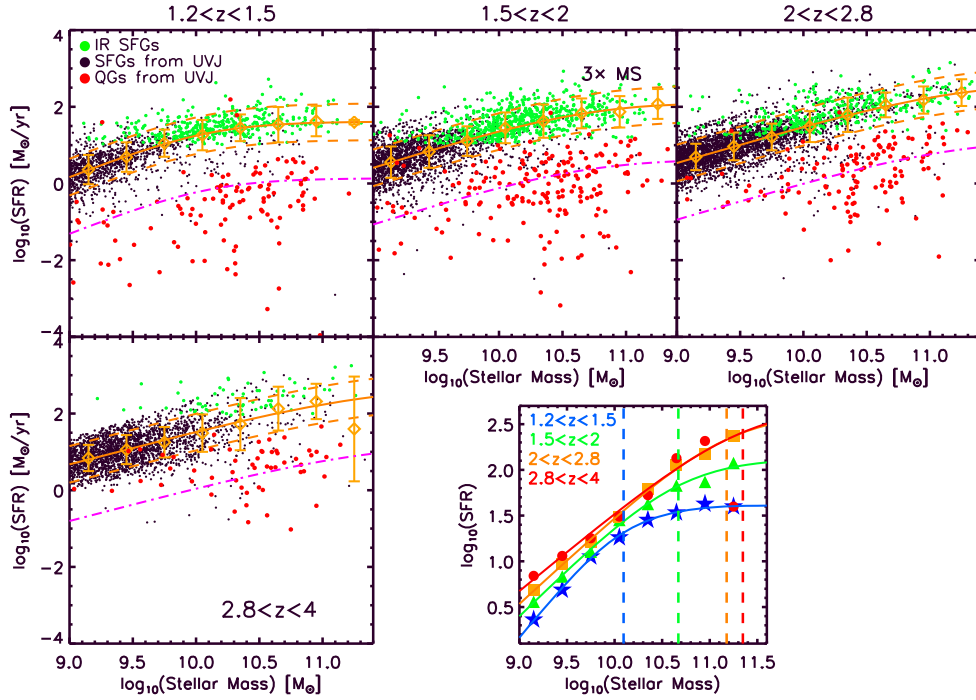

Figure 9. log(SFR) vs. log(M_*) at four redshift intervals corresponding to $\Delta t \sim 1$ Gyr. We fit the MS *only* using SFGs with SFR and M_* estimated from the SED fitting using the best-fit SFHs (black). SFR(IR+UV$_{FUV}$) is used in the case of IR detected galaxies at $z < 3$ (green). The red points are QGs classified from the UVJ colors. The orange line and the error bar represent the MS slope estimated from Equation (4) and the standard deviation of log(SFR) in each stellar mass bin ($\Delta \log(M_*) = 0.3$), respectively. The orange dashed lines are a factor of three above and below the MS slope. The magenta line is the boundary adopted to identify quiescent galaxies relative to the MS. The final panel shows the fitting results obtained from Equation (4) for the four redshift bins, $1.2 < z < 1.5$ (blue), $1.5 < z < 2$ (green), $2 < z < 2.8$ (orange), $2.8 < z < 4$ (red). The vertical dashed line is the turnover mass, M_0, measured for each redshift bin. More details on the MS can be seen in Figure 10.

$z < 2$. This bending of the MS has been explored from the local to $z \sim 4$ universe (Whitaker et al. 2014; Gavazzi et al. 2015; Lee et al. 2015; Tomczak et al. 2016). β_1 is slightly shallower than the finding of Whitaker et al. (2014) at $1.5 < z < 2.5$, but agrees well at $1.2 < z < 1.5$. This may be

because they fixed M_0 to $\log(M_*/M_\odot) = 10.2$ at all redshifts. At $z > 2$, the slope can be rather explained by a single power-law with $\beta_1 \sim 0.8$.

A recent paper by Renzini and Peng (2015) suggested that the MS slope is better explained by a single power-law at
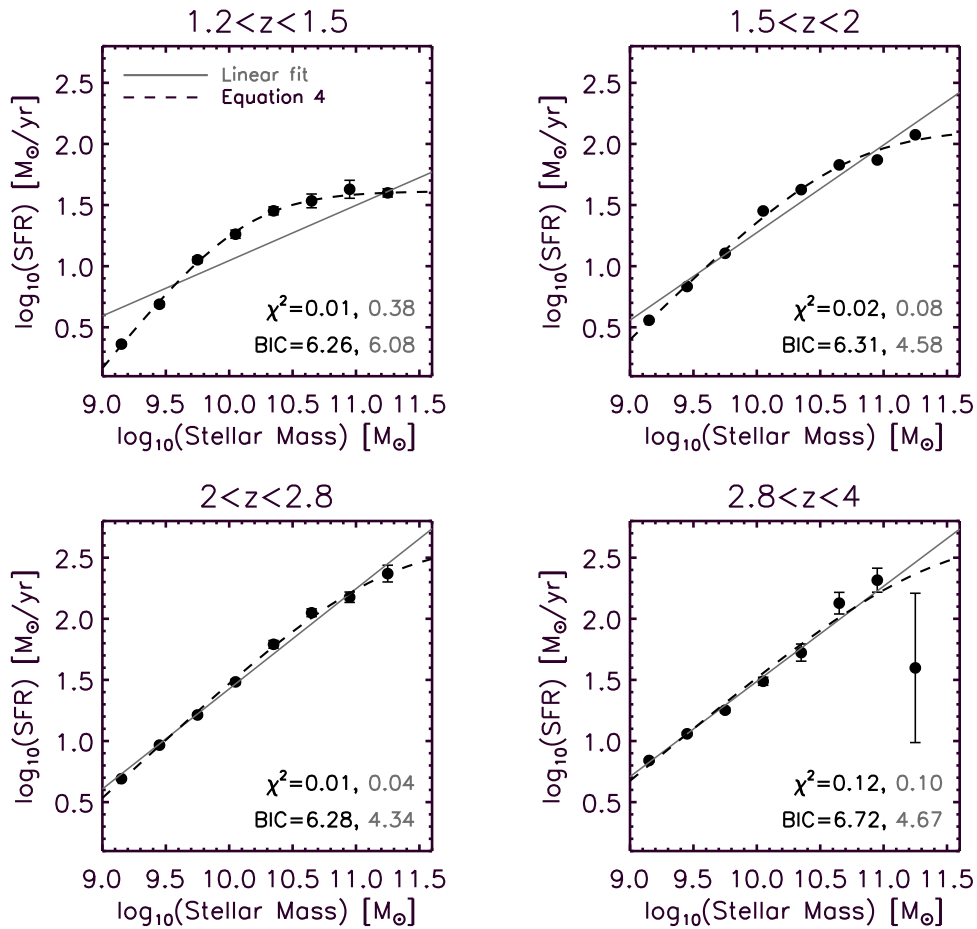
Figure 10. Comparison of the linear fit and polynomial fit (Equation (4)) to the MS in the log(SFR)–log(M_*). The points and error bars represent the mean and standard error ($\sigma/\sqrt{N}$) of SFRs in each stellar mass bin. We fit the data (black points) to the single power-law (linear fit, gray) and Equation (4) (dashed black), and compute a reduced χ^2 and Bayesian Information Criteria (BIC) between the fit and data using σ of the MS from Figure 9. There is no significant difference between the two fittings.

$z \sim 0$, in contrast to Figure 2 in Gavazzi et al. (2015). In Figure 10, we compare the linear (gray) and analytic function fit (black dashed line: Equation (4)) to investigate how the MS fit differs from the single power-law. Although the analytic function fit is almost identical to the linear fit at lower stellar masses, we find an analytic function to be a better fit to the decreasing SFRs at highest masses. Because it is hard to discriminate visually, particularly in the case of the Equation (4) having an extra parameter (M_0), we test which model is a better fit using the reduced χ^2 and the Bayesian information criterion (BIC). The BIC is defined as $\chi^2 + k \ln(n)$, where k is the number of model parameters and n is the number of data points. Figure 10 shows that the linear fit has lower BIC than the polynomial fit over all redshifts. However, the differences between the BIC values are less than two, indicating that the two models are similar. Also, the difference of reduced χ^2 values between linear and Equation (4) is insignificant except in the redshift bin $1.2 < z < 1.5$, which has a smaller reduced χ^2 values with an analytic function fit. Note the small SFR dispersion in the highest mass bin at $1.2 < z < 1.5$ due to three galaxies that accidentally have similar SFRs, which might be responsible for the apparent downward bending of the MS. We believe that the bending is real, though, since we still observe the decline of the MS slope in the high-mass bin when we increase the bin size to

have better statistics. Based on this result, we suggest that a single power-law can generally explain MS with and without the bending of the MS, but the analytic function would be suitable to investigate the curved MS at high masses.

At $z < 2.8$, the observed dispersion of of the log(SFR)–log(M_*) relation (MS dispersion) is consistently measured to be $\sigma \sim 0.35$–0.4 dex at all masses. The MS dispersions obtained in this work are analogous to ones reported by Lee et al. (2015). At $z > 2.8$, the MS dispersion is 0.47 dex. It is possible that increased uncertainties in the photometric redshifts and consequently all derived physical parameters (i.e., SFR) at high redshifts lead to this larger dispersion. However, it is also the case that the adoption of different SFHs in the SED fitting can induce a larger MS dispersion (Salmon et al. 2015; Cassará et al. 2016). This may be why our measured MS dispersion is larger than results based on UV+IR SFRs alone (e.g., Whitaker et al. 2012; Schreiber et al. 2015). The overall normalization of the MS increases with redshift (see the last panel of Figure 9). It has been suggested that this higher sSFR of distant galaxies is related to their larger gas fractions at high redshifts (Sargent et al. 2014).

Overall, our results show a good agreement with other studies which explored the same epoch with different samples and SFR indicators (Karim et al. 2011; Whitaker et al. 2014; Schreiber et al. 2015; Tomczak et al. 2016); all of these studies
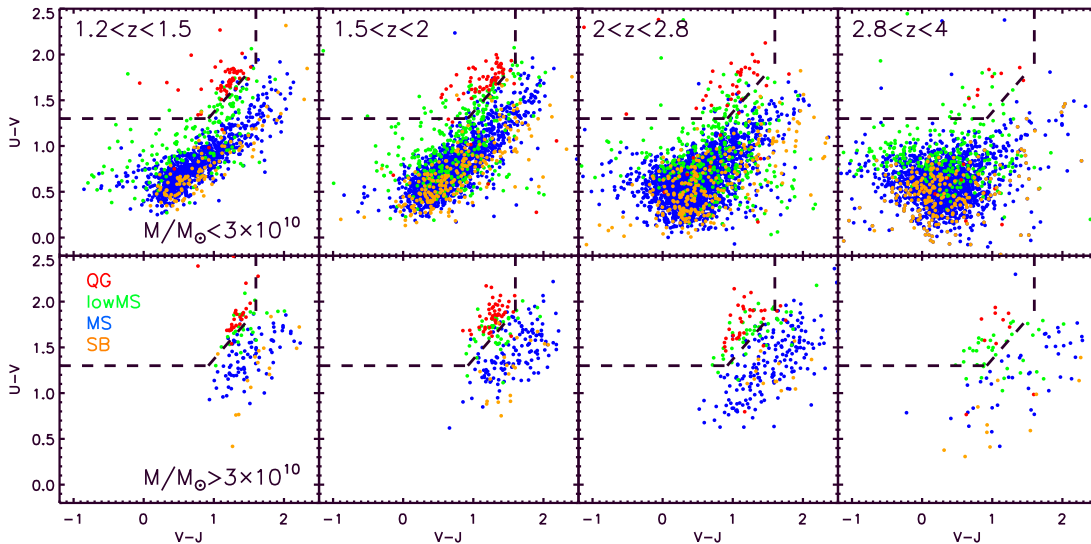
Figure 11. Rest-frame UVJ diagram with four different galaxy populations: starbursts(SB: orange), normal SFGs on the MS (MS: blue), galaxies located below the MS (sub-MS: green), and quiescent galaxies (QG: red). We divide the sample into two stellar mass bins, $1 \times 10^9 < M_*/M_\odot < 3 \times 10^{10}$ (top) and $M_*/M_\odot > 3 \times 10^{10}$ (bottom). Rest-frame colors of the sub-MS galaxies are intermediate between QG galaxies and normal SFGs on the MS.

report that the MS slope below a certain stellar masses ($>2 \times 10^{10}\ M_\odot$ at $z > 1.2$) is close to unity, 0.8–1.0, while the slope dramatically declines for massive galaxies starting around $z = 2$.

4.2. The Properties of Galaxies in the $\log(SFR)$–$\log(M_*)$ Diagram

In the $\log(SFR)$–$\log(M_*)$ diagram, there are non-negligible populations of galaxies that do not lie on the MS. Using our best estimates of galaxy properties, we make a robust characterization of galaxies into four classes based on their positions in the $\log(SFR)$–$\log(M_*)$ plane by measuring the excess in sSFR, or "starburstiness" (R_{SB}). Starburstiness (Elbaz et al. 2011) is defined as $R_{SB} = sSFR/sSFR_{MS}$, which is the distance from the MS measured using Equation (4) in Section 4.1 at a given stellar mass. Here, galaxies are classified as starburst galaxies (SB), normal SFGs on the MS (MS), galaxies below the MS with little star formation activity (sub-MS), and quiescent galaxies (QG) based on R_{SB}. We use $R_{SB} = 3$ to identify galaxies outside 1-σ of the MS at all redshifts. Consequently, the SB galaxies located above the main sequence are defined as galaxies having $R_{SB} > 3$. The MS galaxies are defined as those whose R_{SB} is between $1/3 < R_{SB} < 3$ (within 3 times above and below the MS, or 1σ). The sub-MS galaxies are defined as $1/3 < R_{SB} < 1/30$ (10 times below the lower cut of the MS; see the magenta line in Figure 9). Lastly, we call any galaxies with $R_{SB} < 1/30$ quiescent (QG). This classification results in 895 SB (9.0%), 7510 MS (76.0%), 1181 sub-MS (11.9%), and 302 QG (3.1%) galaxies. As expected, the MS galaxies are dominant, but the number of other populations, particularly SB and sub-MS galaxies, are not negligible.

Rest-frame (U–V) and (V–J) colors of the four populations are illustrated in Figure 11. The galaxies are divided into two stellar mass bins, above and below $M_*/M_\odot = 3 \times 10^{10} \sim \log(M_*) = 10.5$, which roughly corresponds to the turnover mass at $z \sim 2$. SB galaxies tend to be located in the bulk of SFG color–color region. About 83% of the QG galaxies would also be UVJ-selected quiescent galaxies.

Interestingly, the rest-frame colors of the sub-MS galaxies are almost exclusively intermediate between the QG and MS galaxies for the low stellar mass bin. Whereas the same is true for more massive galaxies, there also exist sub-MS massive galaxies with a range of rest-frame colors consistent with normal star-forming galaxies. We find out 15.6% of the sub-MS galaxies are rest-frame UVJ classified as quiescent galaxies, and there is no sub-MS galaxy with sSFR < 0.01 Gyr^{-1}.

5. The Morphology of Galaxies and Their Position in the $\log(SFR)$–$\log(M_*)$ Plane

The relationship between galaxy morphology and star formation history has been studied at $z \sim 2$ (Cameron et al. 2011; Szomoru et al. 2011; Wuyts et al. 2011; Wang et al. 2012; Lee et al. 2013) using various diagnostics beyond visual inspections, including non-parametric measures (Gini [G]: Abraham et al. 2003; M_{20}: Lotz et al. 2004; multiplicity [Ψ]: Law et al. 2007; Concentration [C], Asymmetry [A], and Clumpiness [S]: Conselice 2003), parametric measures (Sérsic index, half-light radius: van der Wel et al. 2012; Whitaker et al. 2015), and projected mass density (Franx et al. 2008; Cassata et al. 2011, 2013; Barro et al. 2013; Fang et al. 2013; Whitaker et al. 2017). In this section, we explore how morphologies of galaxies correlate with their positions on the $\log(SFR)$–$\log(M_*)$ diagram. We use "starburstiness" (R_{SB}), defined in Section 4.2, as a metric quantifying the position of galaxies in $\log(SFR)$–$\log(M_*)$ space relative to the main sequence (MS).

We consider how R_{SB} correlates with Sérsic index (n) and half-light radius (R_e) in Section 5.1, stellar mass surface density (Σ_{50} and Σ_1) in Section 5.2, and G and M_{20} in Section 5.3. Each morphological parameter is introduced in greater detail in the subsequent sections, where we perform an extensive analysis of galaxy morphologies at $1.2 < z < 4$.

Throughout this section, Spearman's rank correlation coefficient, r_s, is used to compute the correlation between morphologies and R_{SB} statistically. This coefficient describes how two variables are monotonically related. Thus, $+1$ (-1) means that two values have a perfect monotonic increasing

(decreasing) relationship, while zero indicates that there is no correlation between two values. We interpret the results of r_s, adopting the following guidelines:

1. $|r_s| < 0.19$ is considered to show no significant correlation.
2. $0.20 < |r_s| < 0.39$ is a weak correlation.
3. $0.40 < |r_s| < 0.59$ is a moderate correlation.
4. $0.60 < |r_s| < 0.79$ is a strong correlation.
5. $0.80 < |r_s| < 1.0$ corresponds to a very strong correlation.

5.1. Fitting the Sérsic Light Profile

The most commonly used parametric diagnostics of galaxy morphology include the Sérsic function, describing the light profile, and the effective radius enclosing half of the light. We fit the Sérsic function to the *HST*/WFC3 F160W (H-band) images using the GALFIT package (van der Wel et al. 2012; hereafter, VDW12), which returns the Sérsic index (n), semimajor axis (SMA), axis ratio, position angle, and various flags by fitting a single Sérsic profile to a galaxy. To avoid large systematic and random uncertainties, we exclude galaxies having GALFIT FLAG $\neq 0$ ($\sim$18%). VDW12 also suggested that faint galaxies are expected to produce biased results. Although we use deeper images (10-epoch) than what was used in VDW12 and most of our sample is relatively bright ($H < 26$), we repeat our morphological analysis in Appendix A using only galaxies having $H < 24.4$, which is a suggested magnitude limit of VDW12 for Sérsic index. We find that restricting the sample to bright galaxies does not change the overall results. Therefore, we do not limit the sample based on the galaxy's magnitude in this study.

The distributions of the Sérsic index and half-light radius as a function of $R_{\rm SB}$ are shown in Figure 12. The circularized half-light radius, R_e, is computed in units of kpc using the formula, $R_e = {\rm SMA}\sqrt{\text{axis ratio}}$. On average, n increases (see the top figure in Figure 12) and R_e decreases (the bottom figure) as $R_{\rm SB}$ decreases. Most galaxies located below the MS (QG and sub-MS) have $n > 2.5$ and $R_e < 2\,kpc$ over all stellar mass and redshift ranges. Based on r_s (see numbers in the bottom panel), we find that massive galaxies show moderate to strong correlations (anti-correlations) between R_e and $R_{\rm SB}$ at $z < 2.8$, while n of massive galaxies at $z < 2$ is moderately correlated with $R_{\rm SB}$. All correlations at $z > 2.8$ are either weak or insignificant. These results are in broad agreement with those presented in Wuyts et al. (2011), Brennan et al. (2017), and Pandya et al. (2017), who present the correlation between specific star formation rate (similar to $R_{\rm SB}$) and Sérsic index across the log(SFR)–log(M_*) diagram since $z \sim 2.5$. For lower mass galaxies, $R_{\rm SB}$ is only weakly correlated with R_e. Similarly, $R_{\rm SB}$ is also weakly correlated with n for low-mass galaxies at $z < 2$, with very weak or insignificant correlations at $z > 2$.

5.2. The Effective Surface Density and Projected Central Mass Density

It has been suggested that the compactness of a galaxy is closely connected to quiescence (Bell et al. 2012; Lang et al. 2014; McIntosh et al. 2014). Sérsic index, bulge-to-total ratio (B/T), and the stellar density are commonly used to identify compact structures (Cassata et al. 2011, 2013; Cheung et al. 2012; Barro et al. 2013, 2017; Fang et al. 2013; Lang et al. 2014; Schreiber et al. 2016). At $z < 0.8$, Cheung et al. (2012) and Fang

et al. (2013) suggested that the projected central mass density is a stronger predictor for the quenching of star formation (SF) than B/T and Sérsic index. In this study, we compute two mass densities, the effective surface mass density (Σ_{50}), and the projected mass density within the central 1 kpc (Σ_1). We investigate trends between the position of galaxies in the log(SFR)–log(M_*) plane and mass density, which is often used as a proxy of compactness. The first, Σ_{50}, is defined as half of the stellar mass divided by a surface surrounded by a half-light radius, $\Sigma_{50} = M_*/2\pi R_{\rm e}^2$ [$M_\odot/{\rm kpc}^2$]. In Cassata et al. (2011), compact QGs at $1.2 < z < 2.5$ are defined as the galaxies located 1-σ below the distribution of local QGs on the mass-size relation, while QGs 0.4 dex smaller than the local QGs are called ultra-compact galaxies. Adopting their definition, we identify galaxies having $\Sigma_{50} > 3 \times 10^9\,M_\odot/{\rm kpc}^2$ (log $\Sigma_{50} \sim 9.5$) and $\Sigma_{50} > 1.2 \times 10^{10}\,M_\odot/{\rm kpc}^2$ as high-mass density and ultra-high-mass density galaxies, respectively (sky blue, violet vertical lines in the top of Figure 13).

The projected central mass density, Σ_1, is the extrapolated projected central density, defined as $M_*(<1\,{\rm kpc})/\pi(1\,{\rm kpc})^2$. The stellar mass within 1 kpc is calculated numerically with the following equation:

$$M_*(<1\,{\rm kpc}) = \frac{\int_0^{1\,{\rm kpc}} I(r)2\pi r dr}{\int_0^\infty I(r)2\pi r dr} \frac{L_{\rm galfit}}{L_{\rm phot}} M_{\rm phot}, \qquad (5)$$

where $I(r)$ is the Sérsic profile and $M_{\rm phot}$ is the stellar mass. $L_{\rm galfit}$ is the total luminosity as computed by integrating a Sérsic profile obtained from GALFIT. $L_{\rm phot}$ is the total luminosity of a galaxy from the CANDELS H-band catalog. Barro et al. (2017) selected compact galaxies with log(Σ_1) > 9.5, defined from the tight correlation between the Σ_1 and stellar masses of the quiescent galaxies. We use this same definition to classify galaxies having the high-central density (orange horizontal line in the bottom of Figure 13).

As illustrated in Figure 13, the correlation coefficient r_s of the relationships Σ_{50} versus $R_{\rm SB}$ and Σ_1 versus $R_{\rm SB}$ is similar to that of R_e versus $R_{\rm SB}$, and they are higher than that for the Sérsic index. In other words, the effective surface mass density, projected central mass densities, and effective radius all show moderate to strong correlations with $R_{\rm SB}$ at $z < 2.8$, while the correlation is weaker for the Sérsic index n.

While qualitatively similar, the relationship between log(Σ_1) and $R_{\rm SB}$ is characterized by significantly less scatter than that of log(Σ_{50}), suggesting that the latter is a noisier statistic than the former. As discussed in Appendix B, this is supported by the direct comparison of log(Σ_1) and log(Σ_{50}), as well as the comparison with the non-parametric statistics, Gini and M_{20}, which provide an alternative description of the degree of "compactness" and "nucleation" of galaxies. We suspect that the higher statistical noise of Σ_{50}, which is solely derived from the parameter r_e, is due to the comparatively large covariance between n and r_e in the fit of the light profile to the Sérsic function. The value of Σ_1, which depends on both r_e and n, evidently turns out to be much better constrained than the two parameters individually. Thus we reach the same conclusions as Whitaker et al. (2017) that the extrapolated projected central stellar density is a better parameter to investigate the connection between the galaxies' central morphology and their star formation activities.
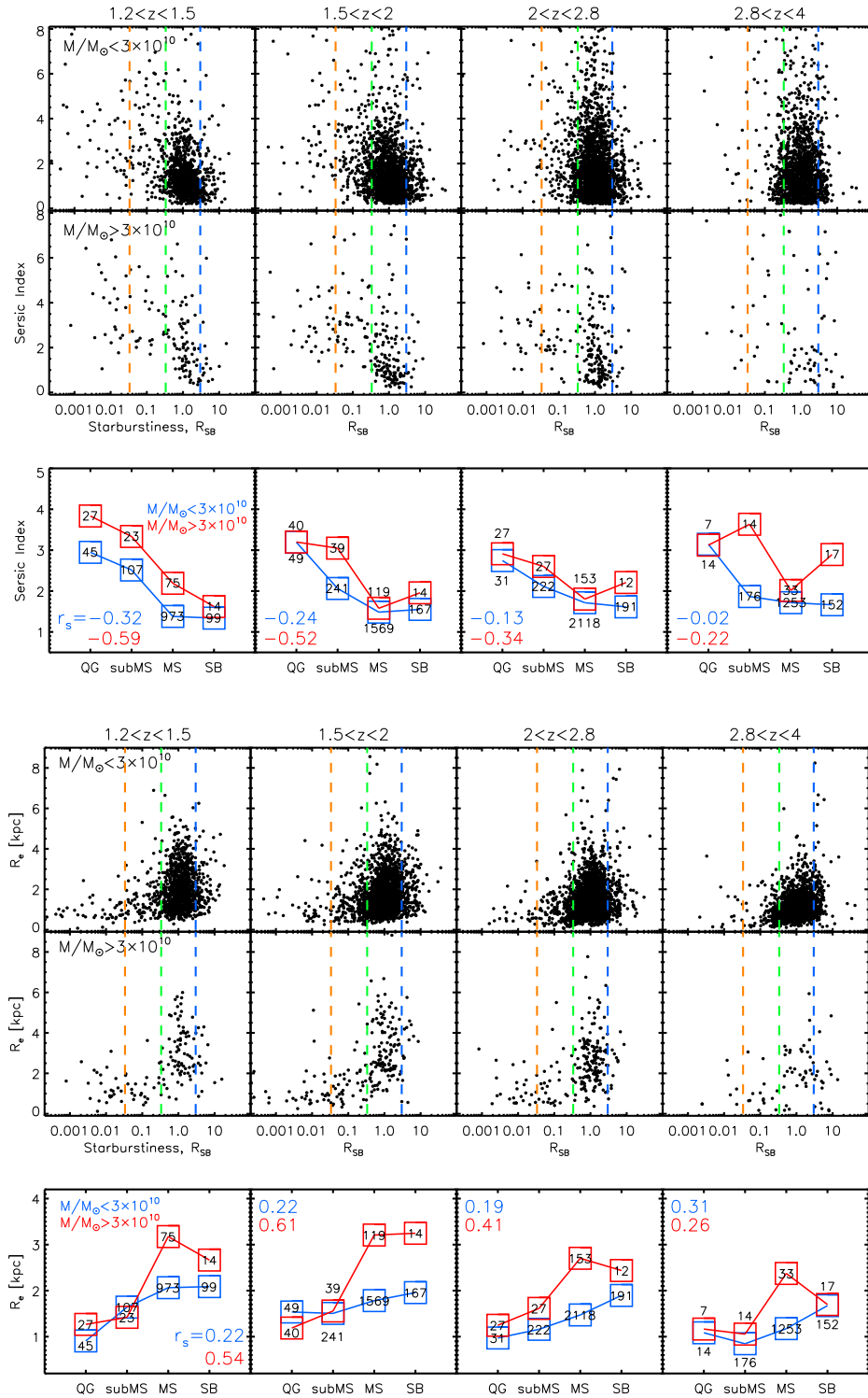
Figure 12. We study the correlation between R_{SB} and Sérsic index(n)/half-light radius(R_e) for four different galaxy populations on the log(SFR)–log(M_*) relation across four redshift bins. In the top two panels, blue, green, and orange vertical lines indicate $R_{SB} = 3$, $1/3$, $1/30$ for the classification of galaxies as SB, MS, and sub-MS, respectively. Galaxies to the left of the orange line are classified as the QG galaxies, irrespective of their rest-frame UVJ colors. The top panels show distributions of n/R_e as a function of R_{SB} for galaxies having stellar masses below (above) $3 \times 10^{10} M_{\odot}$. The bottom panel shows the average Sérsic indices/R_e of the four galaxy populations for the high-mass (red) and low-mass (blue) samples. The number inside the square symbol indicates the number of galaxies in each galaxy population. r_s is the Spearman's rank correlation coefficient between n/R_e and R_{SB} for each redshift and mass bin. Top figure: R_{SB} vs. Sérsic index (n). On average, galaxies tend to have higher n as R_{SB} decreases. The overall correlation between n and R_{SB} is weak, especially at higher redshifts and lower masses. We find a moderate correlation for massive galaxies at $z < 2$. Bottom figure: R_{SB} vs. half-light radius (R_e). On average, as R_{SB} increases, the sizes of the galaxies increase. The correlation between R_{SB} and R_e is weak in all redshift bins for lower mass galaxies and the highest redshift massive galaxies, whereas it is a moderate to strong trend for massive galaxies at $z < 2.8$.

The relationship between Σ_1 and R_{SB} in the bottom of Figure 13 illustrates what appears to be a general property of galaxies, namely that as long as galaxies are on or above the main sequence (i.e., actively forming stars), their central density spans a broad range of values, to first order homogeneously distributed. The central density of galaxies
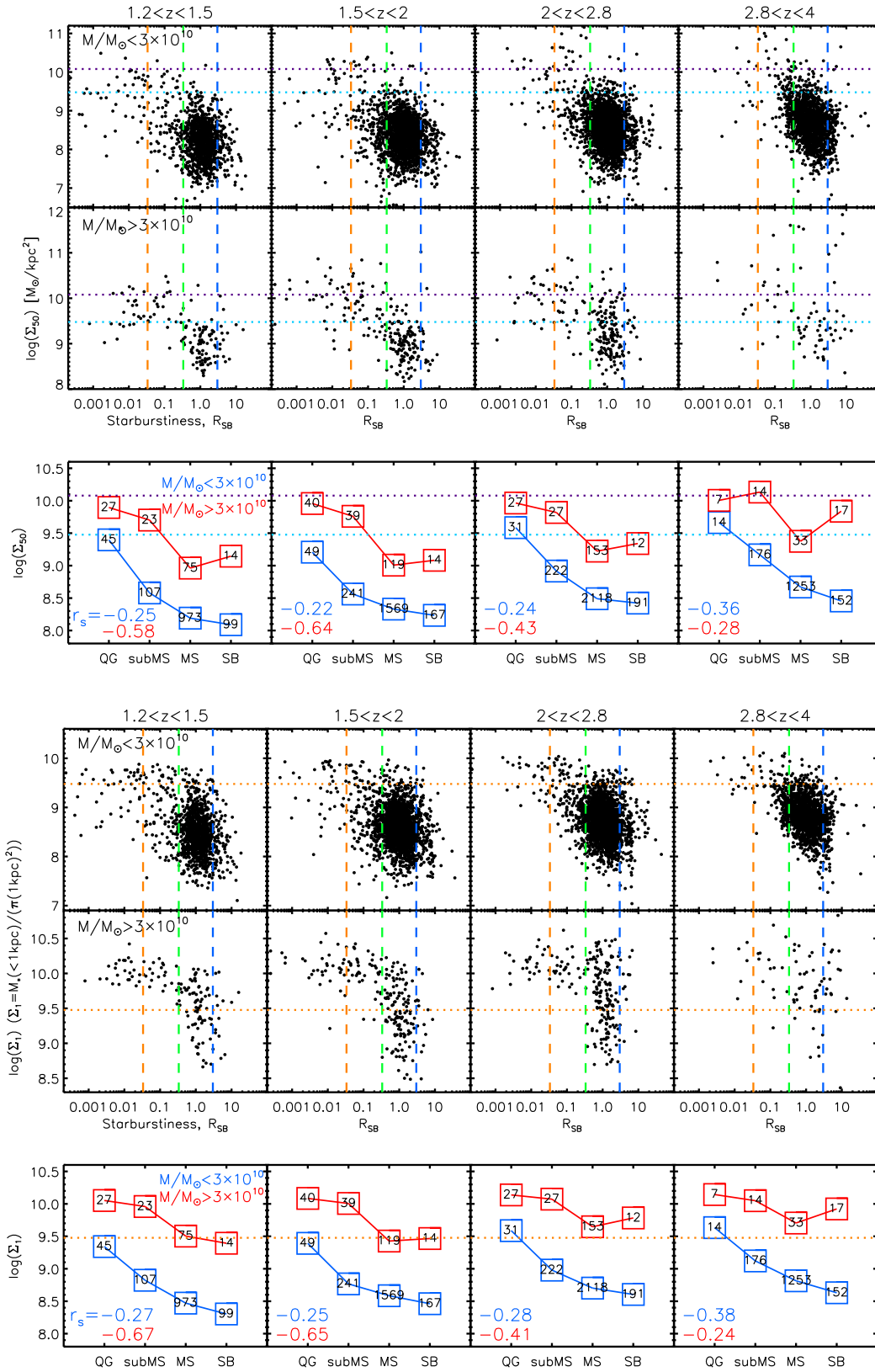
16

Figure 13. Top figure: surface mass density within the effective radius, Σ_{50}, vs. R_{SB} (two top panels) and the average Σ_{50} for the four galaxy populations classified based on R_{SB} (bottom panel). The horizontal lines represent the classification of high density and ultra-high density galaxies defined from Cassata et al. 2011 (sky blue: $\Sigma_{50} = 3 \times 10^9$, violet: 1.2×10^{10}). On average, massive galaxies at $z < 2.8$ show moderate to strong anti-correlations, becoming denser as R_{SB} decreases. The trend is present but weaker in the highest redshift bin. Similarly, we find a weak trend between Σ_{50} and R_{SB} for low-mass galaxies. Bottom figure: extrapolated projected central density, Σ_1, vs. R_{SB} (two top panels) and the average of Σ_1 for the four galaxy populations (bottom panel). The horizontal line is for the classification of high-central density galaxy, $\log(\Sigma_1) = 9.5$, from Barro et al. 2017. The r_s values for Σ_1 are similar to those for Σ_{50}, but with less scatter in the correlation (see top panel).
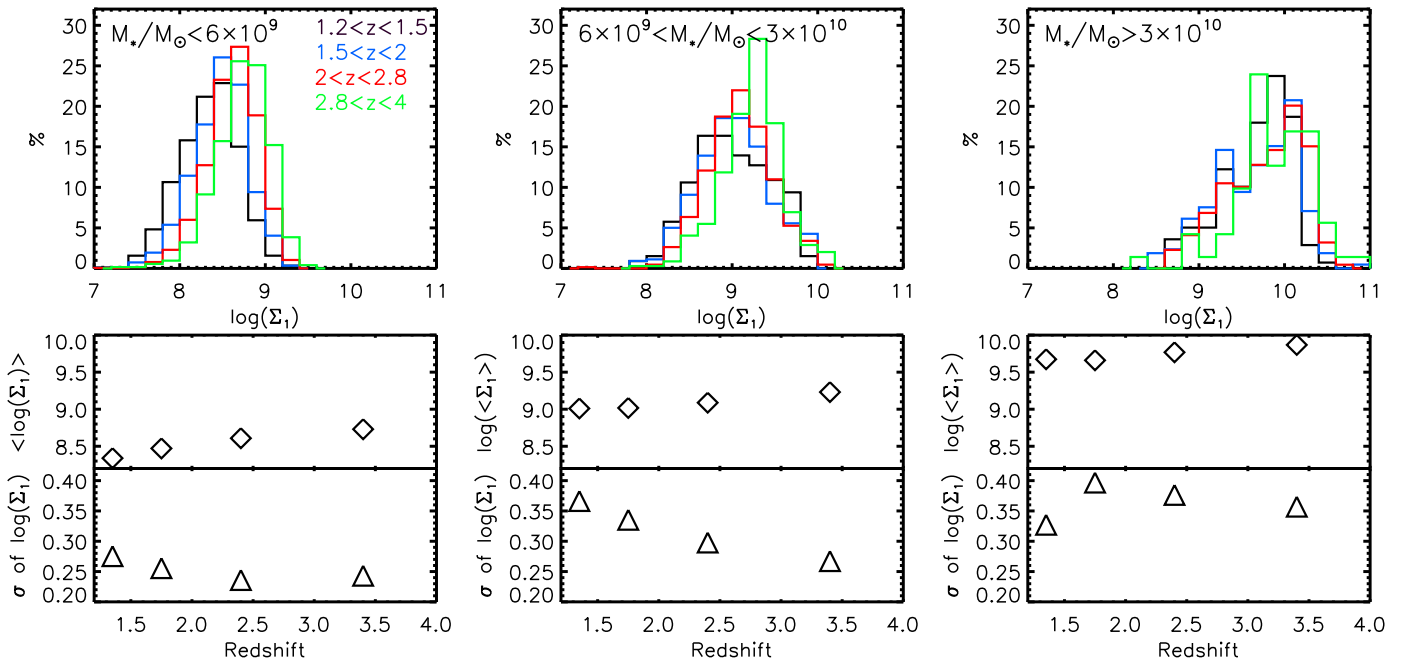
Figure 14. Dependence of the distribution of $\log \Sigma_1$ on stellar mass and redshift. Here we split our low-mass bin ($10^9 < M_*/M_\odot < 3 \times 10^{10}$) into two sub-bins to study the trends in more careful detail. The upper panels show the evolution of the distribution, where we have color-coded the histograms in each of our four redshift bins. The lower panels show the redshift evolution of the mean and the variance of $\log \Sigma_1$. The range of values of $\log(\Sigma_1)$ in each mass bin decreases with decreasing mass, reflecting the well-known correlation between stellar mass and central density (e.g., Woo et al. 2015). But overall, at fixed stellar mass, there are only subtle changes in the dependence of $\log(\Sigma_1)$ with redshift. The range of values covered by the distribution, as well as its peak remains fairly constant, as reflected by the very mild redshift dependence of the mean. The distribution tends to become more extended toward lower $\log(\Sigma_1)$ values as the redshift decreases, which causes the variance to increase correspondingly.

below the main sequence or quenched, on the other hand, is systematically restricted to the approximately top quartile of the distribution of Σ_1, whose value is constant. This result is in very good qualitative and quantitative agreement with similar measures made by Barro et al. (2017) and Brennan et al. (2017). Adopting the value $\log(\Sigma_1) = 9.5$ to define galaxies having the high-central density, the fraction of high-central density galaxies in our sample is 70 (98)%, 23 (95)%, 6 (57)%, and 6 (56)% for QG, sub-MS, MS, and SB galaxies, respectively, where the value in parentheses represents massive galaxies only (i.e., $M_* > 3 \times 10^{10} \, M_\odot$).

This trend between central density and star formation activity is observed in all redshift bins that we have considered here (the larger scatter in the highest redshift bin is consistent with large random errors in the measures), and this independence from redshift is further observed in Figure 14, which plots the redshift evolution of the distribution of $\log(\Sigma_1)$ as a function of stellar mass (top panels), and the mean and variance of $\log(\Sigma_1)$ for the overall population as a function of redshift (bottom panels). While the range of values of $\log(\Sigma_1)$ depend on the stellar mass, monotonically drifting from low to high values as the mass increases, in any given mass bin the range remains fairly constant with redshift. This is also evident in the redshift evolution of the mean (bottom panels), which shows little to no change with time. The shape of the distribution also undergoes only a subtle change, becoming slightly broader toward lower $\log(\Sigma_1)$ values, while keeping the peak substantially unchanged and spanning the same global range of values. This is reflected in the variance that increases toward low redshift. (The only exception is the abrupt decrease of the variance in the lowest redshift bin of the massive galaxies.)

5.3. Non-parametric Morphology: Gini and M$_{20}$

Although the value of Σ_1 is obtained from the Sérsic function parameters fit to the full light profile of each galaxy, it only characterizes the morphology of a galaxy's central regions (i.e., it is a local metric of morphology). A galaxy, however, can have a high value of Σ_1, either if it consists of a predominantly compact nuclear source embedded in a diffuse and fainter component or if it consists of only the compact source (this case is commonly referred to as a "nugget"). Since Σ_1 cannot discriminate between these two cases, which actually might represent the outcomes of different evolutionary and quenching mechanisms (Barro et al. 2013; Woo et al. 2015; Zolotov et al. 2015), we have also characterized the morphology of the galaxies in terms of the Gini coefficient, G, and the second-order moment of the brightest 20% of the galaxy pixels, M_{20}. These diagnostics have been used to describe galaxy morphologies both in the local universe and at high-redshift universe (Abraham et al. 2003; Lotz et al. 2004, 2008; Wang et al. 2012; Lee et al. 2013; Peth et al. 2016). Since not all galaxies are described by smooth and symmetric light profiles, non-parametric measures are known to better characterize the morphologies of irregular galaxies, which are more common at high redshifts (Lotz et al. 2004). For example, Lee et al. (2013) found that the combination of non-parametric and parametric measures of the CANDELS galaxies at $z \sim 2$ provides a more complete description of the morphological properties of high-redshift galaxies than using *only* Sérsic index or R_e.

We have measured G and M_{20} from the WFC3/*HST* F160W (H) images of our samples using the definitions by Lotz et al. (2004). The Gini coefficient provides a powerful description of how nucleated the light of a galaxy is, regardless of its size and mass: light distributed over only a few pixels has $G \sim 1$,

whereas uniformly distributed light corresponds to $G \sim 0$. The M_{20} parameter quantifies the tendency of the light distribution to be in structures (bars, spiral arms, clumps): galaxies with high M_{20} values are clumpy objects, whereas those with low (negative) values of M_{20} are relatively compact objects with one bright core. Thus, for example, a "nugget" would have a large value of Σ_1, a large value of G, and a highly negative value of M_{20}. On the other hand, a galaxy with a massive, compact nuclear component embedded in an extended disk also has a large value of Σ_1 but a lower value of G compared to the nugget. Among massive quiescent galaxies, mean values of G and M_{20} of visually classified nuggets (and non-nuggets) are 0.61 (0.58) and -1.87 (-1.76), respectively.

A complete discussion of the non-parametric morphological measures and their evolution with redshift will be the subject of the second paper in this series. Here we will mostly use the Gini and M_{20} coefficients for a descriptive characterization of the morphology of galaxies on and around the main sequence of star formation.

Figure 15 depicts the distributions of G and M_{20} as a function of R_{SB}, respectively. On average, the galaxies have higher M_{20} (more clumpy) and lower G (more extended) as R_{SB} increases. In other words, the galaxies with more active star formation appear to have more diffuse structures, but the overall correlation between G/M_{20} and R_{SB} for massive galaxies at $z < 2.8$ is weaker than Σ_1 and R_e. r_s of G and M_{20} for less massive galaxies is about <0.15 at all redshifts, an insignificant correlation. Similarly, we find that the correlation of G and M_{20} with R_{SB} barely exists at $z > 2.8$. Such weak or no correlation between non-parametric measures and R_{SB} are observed, even though we only consider very bright galaxies ($H < 24.4$), as shown in Figure 30 (Appendix A).

6. Synthesis of Morphological Trends

A general result of the analysis presented in Section 5 is that main sequence and starburst galaxies cover a broad spectrum of morphologies in all redshift and stellar mass bins considered here, as quantified by our indicators (primarily Σ_1). All the while, quiescent galaxies systematically occupy a more restricted range of the same indicators, located toward the extreme of the distributions where high-central density, compact, and nucleated galaxies are found. The morphology of the sub-MS galaxies is on average intermediate between MS and QG galaxies. The overall trend is that as R_{SB} decreases, galaxies have larger projected (central) stellar density (Σ_1 and Σ_{50}), smaller half-light radius r_e and larger Sérsic index n, and larger G and lower (more negative) M_{20}—namely they are more compact and nucleated. This trend is more pronounced in more massive galaxies. Note that there is in fact either a weak or no significant correlation between R_{SB} and n/non-parametric measures considered for the highest redshift bin at $z > 2.8$ regardless of their magnitudes (see Appendix A).

The trend is particularly evident in Σ_1 versus R_{SB}. For example, Figure 13 (and also Figure 16 in Section 7.1) shows that the range of Σ_1 values of quiescent galaxies is approximately 1/3 (in log space) that of star-forming ones. It is less evident when plotting R_e and n versus R_{SB}, very likely because both are noisier metrics, less representative of a galaxy's overall morphology. In particular, we note that we do not seem to reproduce the tight correlation between n and sSFR observed by Wuyts et al. (2011). Approximately the same compression of the dynamic range of morphological indicators

of quenched galaxies is observed in every redshift bin. Looking at the panel at $2 < z < 2.8$ of Figure 16, for example, this means that the non-compact star-forming galaxies in this redshift range have either (1) not quenched by the time they are observed in the two lower redshift panels (the panels are spaced in cosmic time by $\Delta t \approx 1$ Gyr), or (2) if they have quenched, they have developed a high-central density central region, as quantified by Σ_1.

In fact, the distribution of galaxies in the Σ_1 versus R_{SB} diagram has been interpreted as evidence of morphological transformation during the quenching process itself and possibly of a causal relationship between development of high stellar density and quenching (Cheung et al. 2012; Barro et al. 2013, 2017; Fang et al. 2013; Zolotov et al. 2015; Brennan et al. 2017; Whitaker et al. 2017). Lilly and Carollo (2016) suggested that "progenitor bias" (i.e., the fact that galaxies were smaller and denser in the past) is at least in part responsible for the observed differences between quenched and star-forming galaxies at any epoch. Spectroscopic measures of stellar age at redshift $z < 1.5$ (Belli et al. 2014, 2015; Fagioli et al. 2016; Williams et al. 2017) found that compact galaxies are indeed ≈ 1 Gyr older than normally sized ones, adding support to the idea that progenitor bias plays at least some role.

The extent to which progenitor bias contributes, in part or all, to the apparent morphological transformation of galaxies as they quench illustrated in Figure 13 (and Figure 16) remains to be quantified. However, it is possible that by only using the projected central density Σ_1 (or its noisier sibling Σ_{50}) to quantify the process of "compactification" of galaxies as they complete the transition from the star formation phase to quenching, we may miss the overall features of the phenomenon, since this parameter only describes the transformation at the center of galaxies and does not capture the complexity of morphological evolution and transformation in the whole structure of a galaxy. In the second paper of this series, we will compare Σ_1 as a probe the growth of the core with the non-parametric morphology indicators, G and M_{20}, which inform us about the relative proportions of light (mass) in the core, or in one or more compact sources, and in more diffuse structures in the galaxies.

6.1. Characteristics of the Galaxies Located below the MS

Based on our galaxy classification relative to the MS, we identify a large number of the sub-MS galaxies located below the galaxies on the MS, defined as $1/3 < R_{SB} < 1/30$. The sub-MS galaxies have little star formation (SF) activity but are not yet quenched. We show that the rest-frame colors of the low-mass sub-MS galaxies are intermediate between QG and MS galaxies in Figure 11, while massive galaxies are also intermediate but exhibit a broader range of rest-frame colors consistent with the overall SFG population. The sub-MS galaxies are more spheroidal-like than the MS galaxies as shown in Section 5. These galaxies are seen to be similar to green valley galaxies observed at $z < 1$ in that they have intermediate colors between the red sequence and blue cloud. Schawinski et al. (2014) found that green valley galaxies at $0.02 < z < 0.05$ are located below the MS regardless of morphology and are in the process of quenching. At $z \sim 1$, Mendez et al. (2011) showed that green valley galaxies are typically disk galaxies with high concentrations. Thus, the sub-MS galaxies may be under transition from the star-forming to quiescent populations. The existence of galaxies having
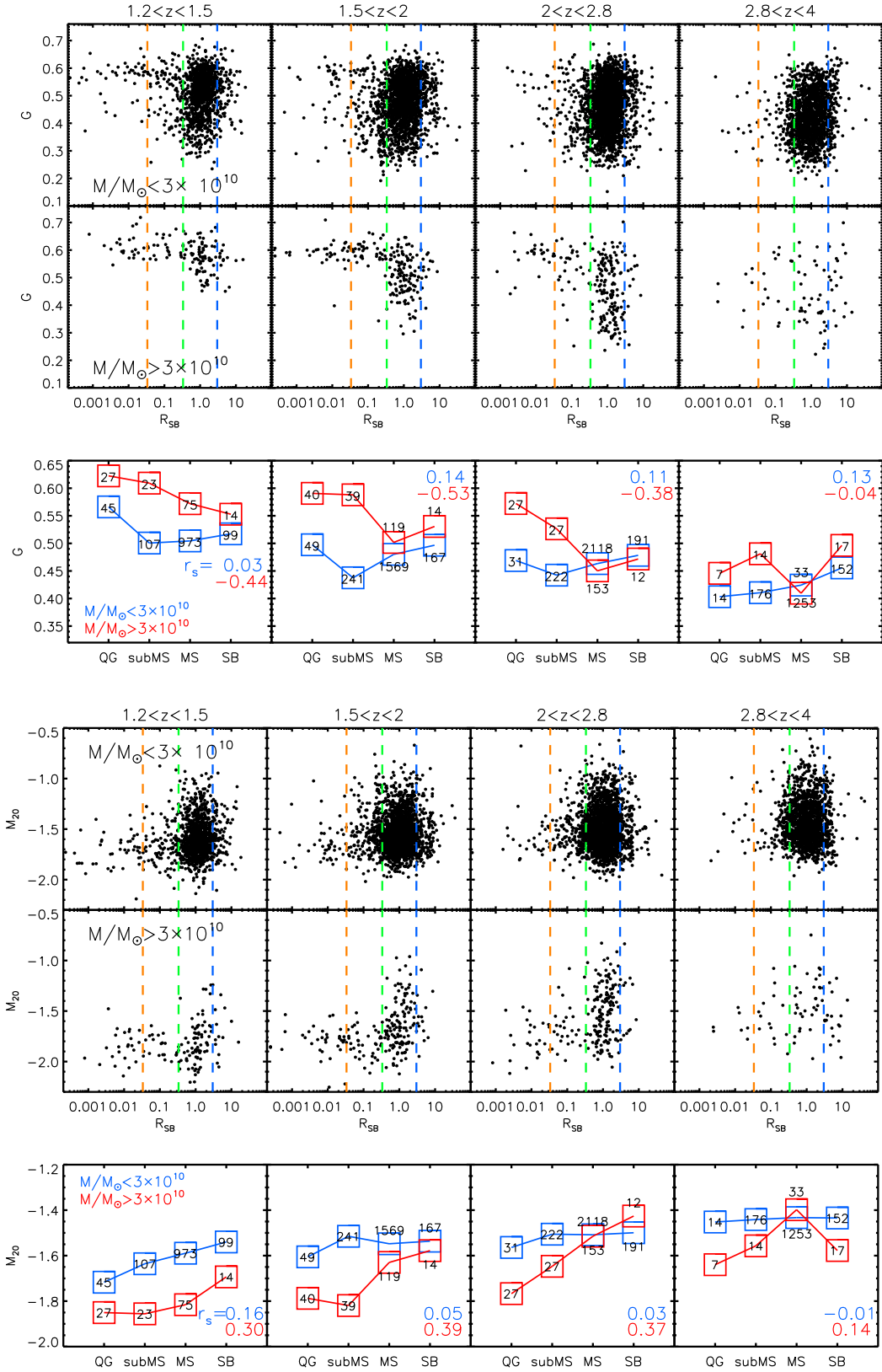
Figure 15. Gini coefficients $(G)/M_{20}$ vs. R_{SB} for individual galaxies at four redshift epochs (top) and the average G/M_{20} across the $\log(SFR)$–$\log(M_*)$ plane, as parameterized by R_{SB}. All lines, colors, and symbols correspond to Figure 12. Top figure: G vs. R_{SB}. QG galaxies have the highest G on average, which is an indication of compact structure. G of massive galaxies at $z < 2.8$ shows moderate/weak correlation with R_{SB}. The low-mass sample and galaxies at the highest redshift has no significant correlation between R_{SB} and G. Bottom figure: M_{20} vs. R_{SB}. SB galaxies have the highest M_{20}, which is indicative of a clumpy sub-structure. For low-mass galaxies at all redshifts, as well as massive galaxies at $z > 2.8$, there is no significant correlation between M_{20} and R_{SB}. M_{20} shows a weak to moderate correlation among massive galaxies at $z < 2.8$.
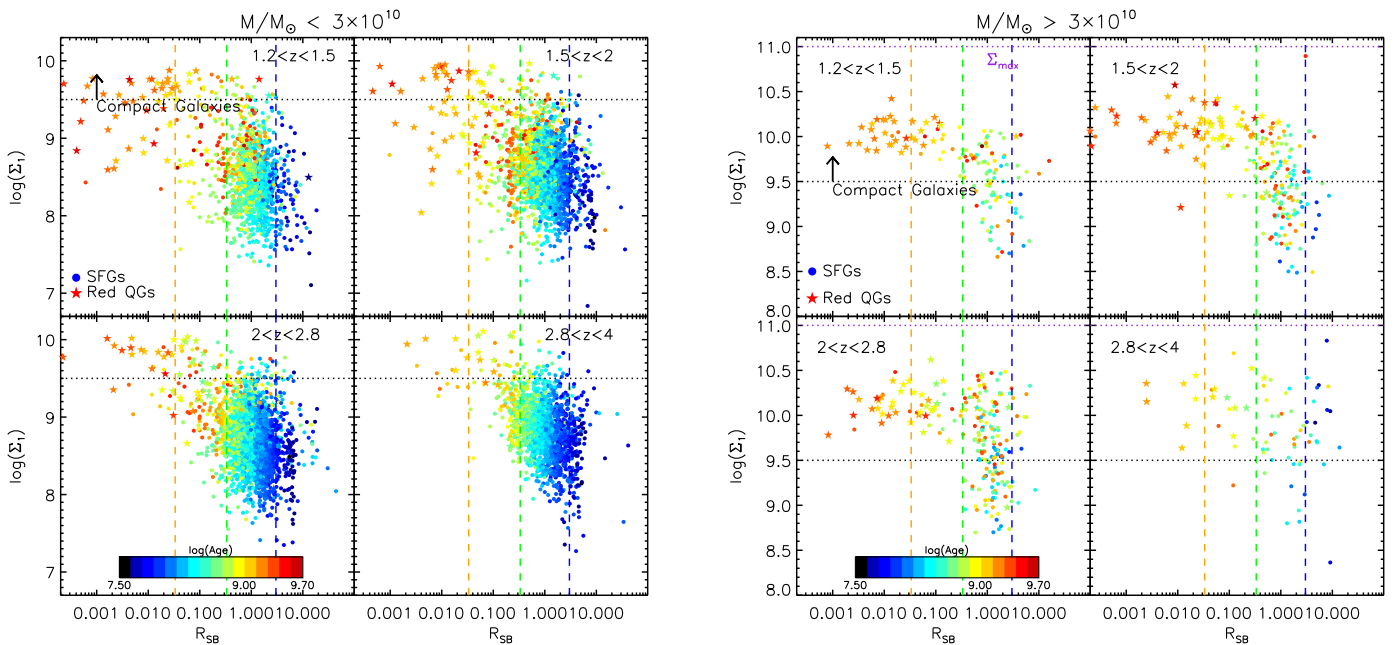
Figure 16. Σ_1 vs. R_{SB} with color-coded median-mass-weighted ages for two stellar mass bins, $M_*/M_\odot < 3 \times 10^{10}$ (left) and $M_*/M_\odot > 3 \times 10^{10}$ (right). Circle and star symbols represent SFGs and red QGs, respectively. Orange, green, and blue lines are to divide galaxies into QG, sub-MS, MS, and SB. Black dotted horizontal line is $\log(\Sigma_1) = 9.5$. Galaxies are older as R_{SB} decreases, but there is no correlation between the projected central density and galaxy age. We also note that massive SFGs are relatively older than less massive SFGs.

intermediate colors and/or morphologies at $z \sim 2$ have been reported; Whitaker et al. (2012) found that galaxies below the MS are redder SFGs having lower sSFR and low-dust attenuation. Pandya et al. (2017) defined the transition galaxies at $z < 3$ as galaxies located between 0.6 dex and 1.4 dex below the main sequence. In a similar vein, Fang et al. (2017) classified "fading galaxies" located in the SFG region of the UVJ diagram, but below the MS ($\Delta \log sSFR < -0.45$ dex), which is a similar definition with our study. These "fading galaxies" have intermediate colors and smaller radii, as well as lower dust attenuation than normal SFGs, indicative of a transition from SFGs to QGs as stopping SF due to the loss of their ISM. We also find that the sub-MS galaxies in our sample have the lower $E(B-V)$ than MS galaxies on average, which further supports that a sub-MS galaxy is transforming to a quiescent galaxy as quenching its SF.

6.2. Morphologies of Starbursts

In this study, starbursts are classified as the galaxies located three times above the MS (SB galaxies). Their very high SFR can be explained by either larger gas reservoirs or a higher star formation efficiency (SFE). Sargent et al. (2014) suggested that the most extreme SFRs observed in high-redshift starbursts would be caused by the SFE boost induced by major mergers, since internal gas reservoirs are depleted quickly due to short-lived SFR boosts. With *Herschel* data, Elbaz et al. (2011) investigated the sizes of starbursts relative to MS galaxies using stacks of rest-frame UV images and found that starbursts at $z \sim 2$ have more compact star formation cores than MS galaxies on average. However, we find that the average rest-frame optical morphologies of the SB galaxies are larger, clumpier (higher M_{20} and lower G), and less dense than ones of the MS galaxies. Most of the SB galaxies in our sample (94%) have $\log(\Sigma_1) < 9.5$ and shallow light profiles ($<n> \sim 1.5$ and 2.3 for less massive and massive SB galaxies). The massive SB

galaxies with $M_* > 3 \times 10^{10}$ have $<R_e> \sim 2.74$ kpc at $1.2 < z < 4$, which is more than a factor of two smaller than QGs, and have $<R_e> \sim 4.0$ kpc at $2 < z < 2.5$, which is about a factor of four smaller than QGs at the same redshift and stellar mass ranges. Morphologically, they are rather different from quiescent galaxies, suggesting that it is unlikely that during the post-starburst phase they can shrink their size to match that of compact quiescent galaxies on a short timescale. This is inconsistent with the previous finding (Wuyts et al. 2011), suggesting a rapid build-up of the central mass concentration in starbursts that have a higher n than the galaxies on the main sequence at $z \sim 2$. One has to be very careful when looking at morphologies of starburst galaxies only using the Sérsic fits, as morphologically disturbed objects would tend to have poor fits (Brennan et al. 2017).

7. Discussion

In this paper, we use the deepest CANDELS data (i.e., the GOODS fields), which have among the broadest and most dense coverage of photometric bands, to investigate general correlations between the position of galaxies at $1.2 < z < 4$ on and around the main sequence and their morphology. We find that the morphology of galaxies clearly correlates with their position in the $\log(SFR)$–$\log(M_*)$ plane. On average, we reproduce previous results that galaxies below the MS tend to have smaller sizes, larger Sérsic indices, a compact central structure with high projected light (mass) densities. By adding measures of stellar age from our new MCMC SED fitting, however, we also find additional more subtle trends that we are now going to discuss.

7.1. Possible Formation Scenarios of Massive, Compact Quiescent Galaxies

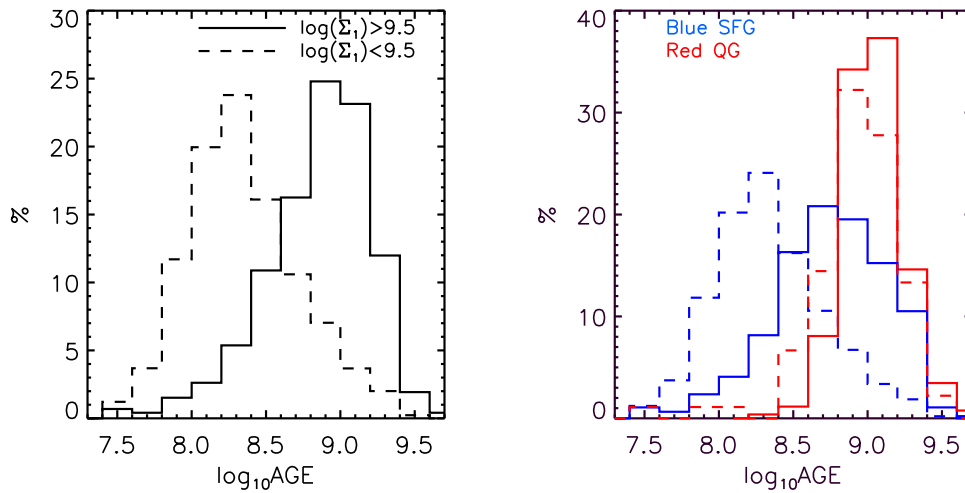Quenching mechanisms in galaxies can be broadly classified by the timescales on which they operate—namely, fast track

Figure 17. Left panel: age histograms of galaxies having high and low-central density, determined by Σ_1. Solid and dashed lines represent galaxies having $\log(\Sigma_1) > 9.5$ and $\log(\Sigma_1) < 9.5$, respectively. Right panel: age histograms of UVJ selected blue SFGs and red QGs. Galaxies having high-central density $(\log(\Sigma_1) > 9.5)$ are relatively older than others for both blue SFGs and red QGs.

and slow-track quenching (Fang et al. 2012, 2013; Barro et al. 2013; Dekel & Burkert 2014; Schawinski et al. 2014; Schreiber et al. 2016). Slow-track quenching appears to dominate at low redshifts or later stages of the galaxy evolution, because it happens when star formation gradually vanishes over several Gyrs. This can be explained by slow gas exhaustion at a critical halo mass, $\sim 10^{12} M_\odot$, without a disruptive external trigger, such as major merging (Fang et al. 2013; Schawinski et al. 2014). As a galaxy on the slow track becomes redder, the inner part of a galaxy becomes denser while the outer disk fades away, and it subsequently moves off to the MS as SF decreases. On the other hand, the fast track quenching is a rapid process occurring with timescales less than 1 Gyr. The gas reservoir of a gas-rich star-forming disk is destroyed by an intensive triggering event such as a merger-induced starburst or a VDI associated with stellar feedback. Then, the gas disk rapidly transforms its morphologies into an early-type and immediately quenches SF and moves to below the MS. The fast track quenching is probably the dominant mechanism at early times and has been proposed to explain the formation of high-redshift massive compact quiescent galaxies (van Dokkum et al. 2008; Barro et al. 2013; Muzzin et al. 2013). Here, we investigate any evidence for slow and fast track quenching based on our morphological analyses of galaxies relative to the MS.

7.1.1. Central Density, Quenching, and Compactification

We find that at any redshift, QGs always occupy a restricted range of values of the morphological parameters Σ_1, G, and M_{20} relative to the spread covered by SFGs. It has been suggested that morphological transformation must take place during the quenching phase (Barro et al. 2013, 2014; Patel et al. 2013; Lang et al. 2014; Zolotov et al. 2015; Tacchella et al. 2016a, 2016b). In this scenario, SFGs are required to shrink their size and develop a compact core within a relatively short timescale, and quench. Highly dissipative gas accretion into the center, or compaction, and adiabatic contraction have been identified in simulations and are considered as viable mechanisms for morphological transformation (Dekel et al. 2013; Dekel & Burkert 2014; Zolotov et al. 2015; Tacchella et al. 2016a, 2016b).

In the simulations, compaction creates dense massive central cores but does not shrink the existing non-dissipative component—namely the stars. Adiabatic compression can compactify the stars, but this should largely take place on the same spatial scales as the gaseous compaction. Thus, it is not clear that the current families of compaction simulations are actually capable of reproducing the observed compact QGs, where the majority do not exhibit extended light profiles on top of the compact central core (Szomoru et al. 2010, 2013).

In any case, if galaxies keep their morphology as they quench, then the progenitors of compact QGs should be the compact star-forming ones. Williams et al. (2014, 2015), van Dokkum et al. (2015), Nelson et al. (2014), and Zolotov et al. (2015) showed that the number density, SFR, mass distribution, and estimated quenching time of compact SFGs are consistent with them being the progenitors of QGs. Note that in the $\log(SFR)$–$\log(M_*)$ diagram, the bulk of compact SFGs are located on the MS or slightly above the MS (Williams et al. 2014; Barro et al. 2017), suggesting that the progenitors should be looked for among normal star-forming galaxies and not starburst ones. This is also supported by the discovery of the short depletion timescales of $\lesssim 100$ Myr for compact SFGs (Barro et al. 2013, 2014; Spilker et al. 2016).

As in previous studies, we also find that the projected central mass density Σ_1 strongly depends on R_{SB}, in the sense that nearly all quiescent galaxies have high Σ_1, and, in the high-mass bin, all of them have $\log(\Sigma_1) > 9.5$. There are, however, MS and sub-MS galaxies that have similarly high values of Σ_1 as QGs. The new aspect of our study is to add the stellar age to the central density and the sSFR. In Figure 16, we further investigate the relationship between morphology and age, and find that as R_{SB} decreases, galaxies get older. Galaxies on the MS, on the other hand, have Σ_1 that spans a broad range of values. If fast quenching follows the formation of a compact central core in most galaxies (Barro et al. 2013; Zolotov et al. 2015), then SFGs with high Σ_1 are expected to be, on average, older than SFGs with lower central densities. The left panel of Figure 17 shows the histograms of the median-mass-weighted age for galaxies with normal and high-central densities $(\log(\Sigma_1) > 9.5)$, regardless of their mass and star formation activity. The
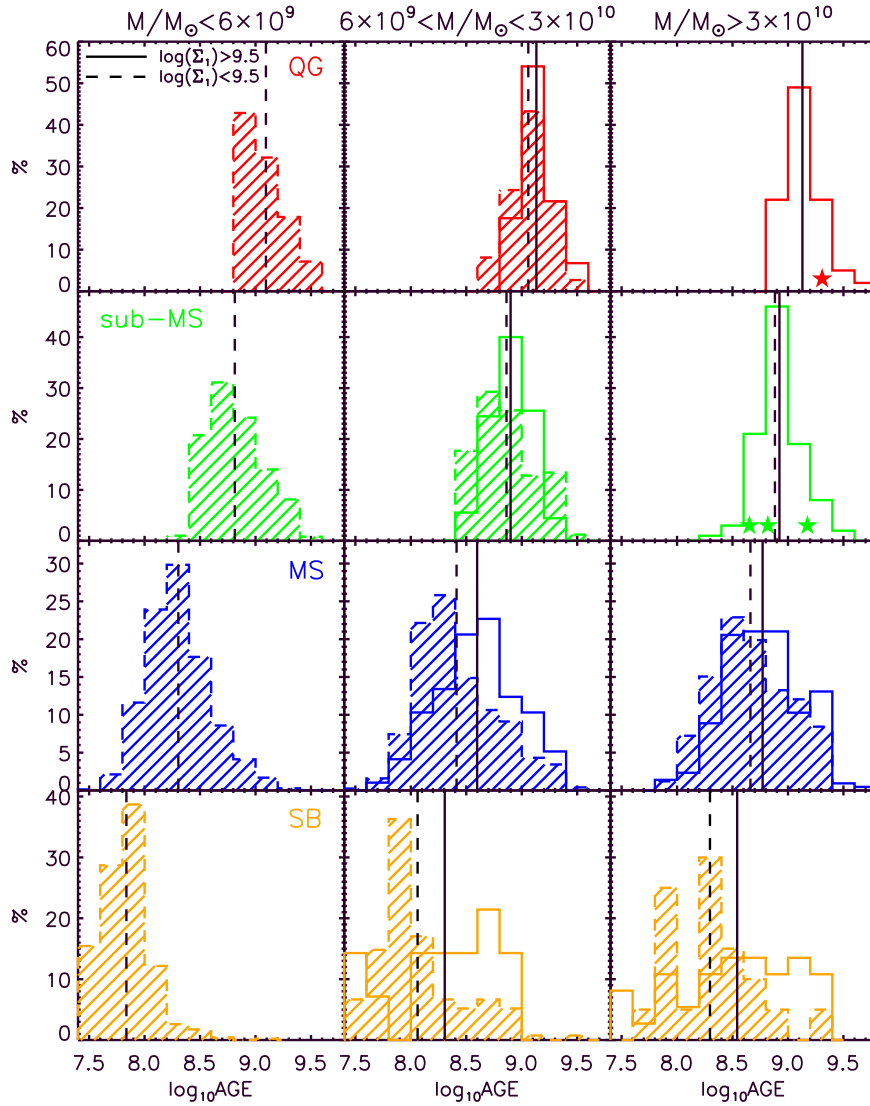
Figure 18. Relative age distributions of QG, sub-MS, MS, and SB galaxies in three stellar mass bins. Plain and shaded histograms represent galaxies having $\log(\Sigma_1) > 9.5$ and $\log(\Sigma_1) < 9.5$, respectively. Note that in the $M_*/M_\odot > 3 \times 10^{10}$ mass bin, there is only one QG galaxy and three sub-MS galaxies having $\log(\Sigma_1) < 9.5$, which are marked with red and green star symbols. Vertical lines stand for mean ages of high-central (solid line) and low-central density (dashed line) galaxies for each population. On average, the QGs are the oldest, while the SB galaxies are the youngest. High-central density massive sub-MS galaxies are older than the rest of the star-forming galaxies.

right panel shows the histograms sub-divided according to their status of either star-forming or passive in the UVJ diagram. Galaxies of all types and mass that have high-central density are on average older, by ≈ 700 Myr, than the others. The right panel shows that the difference still remains among SFGs, but that it tends to vanish among passive ones. To explore this trend in more detail, in Figure 18 we further sub-divide the histograms into three mass bins and four R_{SB} bins, respectively, for both high- and low-central density galaxies. First, there is a clear trend in age from young to old, for all masses, in going from SB to QG galaxies with peak-to-peak values ≈ 500 Myr and ≈ 1 Gyr. The similar age trend is also shown from the predictions using the SAMs that the ages increase from the MS galaxies to green valley to quiescent galaxies (Pandya et al. 2017). We find that there is no galaxy having $\log(\Sigma_1) > 9.5$ at the smallest stellar mass bin, $1 \times 10^9 < M_*/M_\odot < 6 \times 10^9$. In the case of $M_*/M_\odot > 6 \times 10^9$, galaxies with high-central densities are systematically older than those with low-central densities

(with the exception of QG galaxies having $M_*/M_\odot > 3 \times 10^{10}$, where there is only a single low-central density case). The mean age difference is very small for low-mass QG galaxies, but it becomes more pronounced, in both the mean values and the distributions, for MS and SB galaxies, of the order of 100 Myr to a few 100 Myr. Even though the mean age difference between high- and low-central density sub-MS galaxies is small, the distribution of ages suggests that the high-central density sub-MS galaxies quench sooner and have more evolved stellar structures than the low-central density ones, in agreement with the conclusions by Williams et al. (2015) based on the UV spectra of high- and low-density galaxies at $z \sim 3$. This is also consistent with the idea that the progenitors of at least some compact, high-central density galaxies are themselves similarly compact before quenching.

These trends between age, R_{SB} (sSFR), and Σ_1 are consistent with the idea that galaxies develop a massive central structure as they evolve from star-forming to quiescence and that the
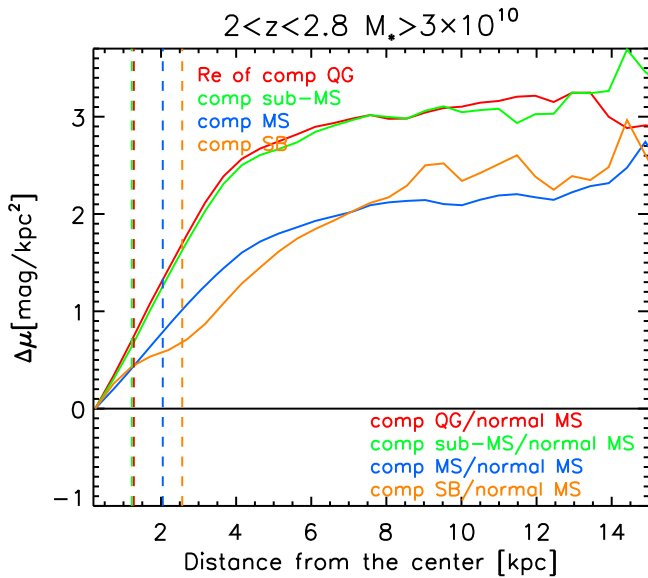
Figure 19. Ratio of the average light profiles of high-central density massive ($\log(\Sigma_1) > 9.5$ and $M_* > 3 \times 10^{10} M_\odot$) galaxies (compact SB, MS, sub-MS, and QG) to that of the low-central density massive MS galaxies ($\log(\Sigma_1 < 9.5)$; normal MS) at $2 < z < 2.8$. A total of 27 QG, 27 sub-MS, 98 MS, 9 SB galaxies, and 55 normal MS are stacked to increase SNR in the outer parts of the light profiles. Vertical lines with different colors stand for the half-light radii (R_e) of stacks of compact QG (red), sub-MS (green), MS (blue), and SB (orange). The high-central density massive QG/sub-MS galaxies have very similar light profiles, and they lose their light faster than the normal MS, indicating that those QG/sub-MS galaxies are not faded MS galaxies. Note that there is about 7% variation in the angular diameter distance between $z = 2$ and $z = 2.8$.

higher the density of this structure, the earlier and more rapid the quenching process is. They do not, however, imply or even necessarily suggest a causal relationship between the central density and the quenching process. The fact that central density of quenched galaxies is always observed to be in a narrow range at the high end of the distribution could simply reflect that star formation typically ends by the time the central parts of the galaxies have reached those values of the projected stellar density. Finally, we observe that massive SFGs are older than their low-mass counterparts, implying that the former quench faster and earlier than the latter, presumably due to some mechanism that depends on the stellar mass.

7.1.2. Is Disk Fading Responsible for the Compactification of Galaxies as They Quench?

Slow-track quenching describes the passive fading of the disk galaxies. As they exhaust their gas, disks gradually fade and bulges become prominent. At low redshift, Fang et al. (2013) found that the bulges become more pronounced and the disks fade away when galaxies evolve from blue to red, and suggested that slow track quenching is the effective quenching process. Motivated from this, we test the fading of disks at $2 < z < 2.8$. We target galaxies having $M_* > 3 \times 10^{10} M_\odot$ at $2 < z < 2.8$ in particular because the number of massive, compact galaxies drops at lower redshifts. The high-central density ($\log(\Sigma_1) > 9.5$) galaxies on, above, and below the MS (compact SB, MS, sub-MS, and QG) and the low-central density ($\log(\Sigma_1) < 9.5$) MS galaxies (normal MS) are stacked to increase the SNR in the outer parts of the light profiles. We,

in turn, plot the differences of surface brightness ($\Delta\mu$) between the high-central density (SB, MS, and sub-MS, QG) galaxies and normal MS galaxies in Figure 19. The surface brightness comes from the *HST*/F160W imaging, which corresponds to roughly the rest-frame B/V band at the redshifts examined. $\Delta\mu$ increases rapidly for the high-central density QG and sub-MS galaxies, indicating that they lose their light faster than the normal MS galaxies. The stacks of the sub-MS galaxies have an almost identical light profile ($n = 4.03$, $R_e = 2.5$ kpc) to those of the QGs having $n = 3.96$ and $R_e = 2.61$ kpc. If the disk fading is responsible for a dense core of the high-central density QG and sub-MS galaxies, we should observe the remnants of disks around the core in stacks. However, we do not find any evidence of the dead disks left in the outer regions of the high-central density QG/sub-MS galaxies (see also Szomoru et al. 2010, 2013). This implies that the high-central density QG/sub-MS galaxies are not faded MS galaxies. It might be the case that the disk fading (slow track quenching) is just less efficient at high redshift because there is not enough time for slow fading to occur or it might occur mainly in massive halos like clusters, which have not formed yet. Alternatively, fast quenching may be dominant at high redshift because of the higher gas fractions at early times invoking more energetic events and causing a rapid quenching of SF (Pandya et al. 2017).

7.1.3. Is the Major Merger-driven Process a Dominant Quenching Mechanism?

In early simulations, strong bursts of star formation by gas-rich mergers leave a compact merger remnant behind (Springel et al. 2005; Hopkins et al. 2008). Subsequently, the compact remnant rapidly quenches star formation, and if the gas fraction is large (e.g., $f_{gas} > 50\%$), its stellar mass is sufficiently large that resulting morphology of the galaxy resembles that of the compact quiescent galaxies observed at $z \sim 2$. The simulated gas-rich merger remnants, however, also have extended stellar halos that originate from the violent relaxation of the pre-existing stellar components (Wuyts et al. 2010). It has been suggested that their morphology is not consistent with that of the massive, compact quiescent galaxies described here, since no extended stellar halos are observed around compact QGs and sub-MS galaxies, either individually or from stacked images, like the one in Figure 19 (e.g., see Figure 16 of Williams et al. [2014], which compares the Sérsic light profile parameters of the merger remnants to those of individual compact galaxies as well as those of stacked images). The results presented here are in agreement with the conclusion of Williams et al. (2014). For example, most starbursts found in this study have larger sizes and more diffuse light profiles, as well as lower G and higher M_{20}, on average than other types of galaxies in the $\log(\text{SFR})$–$\log(M_*)$ diagram, in particular including compact quiescent galaxies of comparable stellar mass. We visually inspected the starbursts galaxies with $M_* > 3 \times 10^{10}$ and $\log(\Sigma_1) > 9.5$, whose redshift is $z > 2.8$ (about half of the starburst sample), and indeed confirm the presence of compact compact structures embedded in a more diffuse light distribution. Most of these sources are found to host heavily dust-obscured star formation and, in approximately 50% of the cases, an AGN (based in the detection of X-ray flux in the *Chandra* images). If most starburst galaxies are
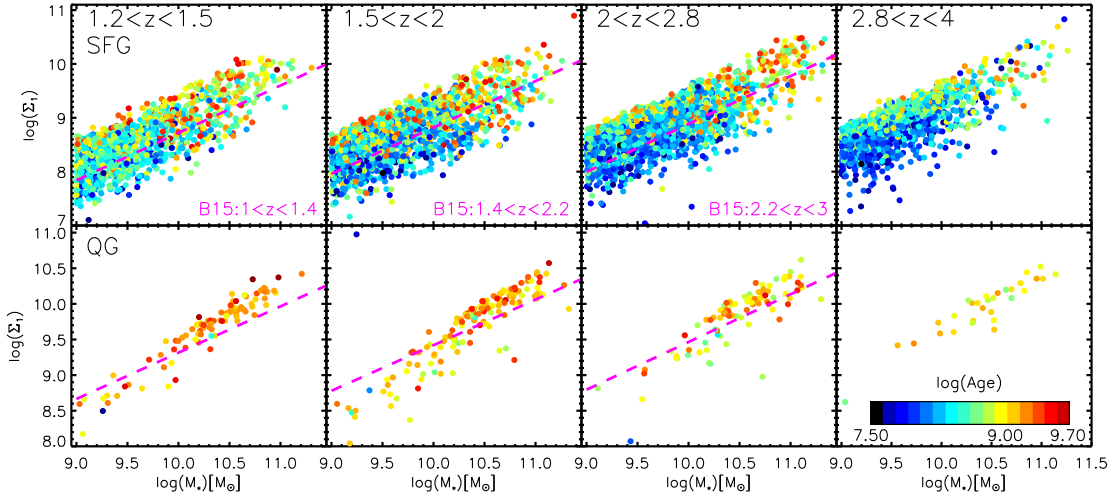
Figure 20. Projected central mass density vs. stellar mass for UVJ selected star-forming galaxies (SFG: top) and quiescent galaxies (QG: bottom) at four redshift bins. The median-mass-weighted stellar age is color-coded, and the best-fit $\log(\Sigma_1)-\log(M_*)$ relations computed from Barro et al. (2017) for two populations are overplotted in the redshift bins in common. Our measures are in good agreement with Barro et al. (2017), and we show a clear correlation between Σ_1 and M_* at all explored redshifts.
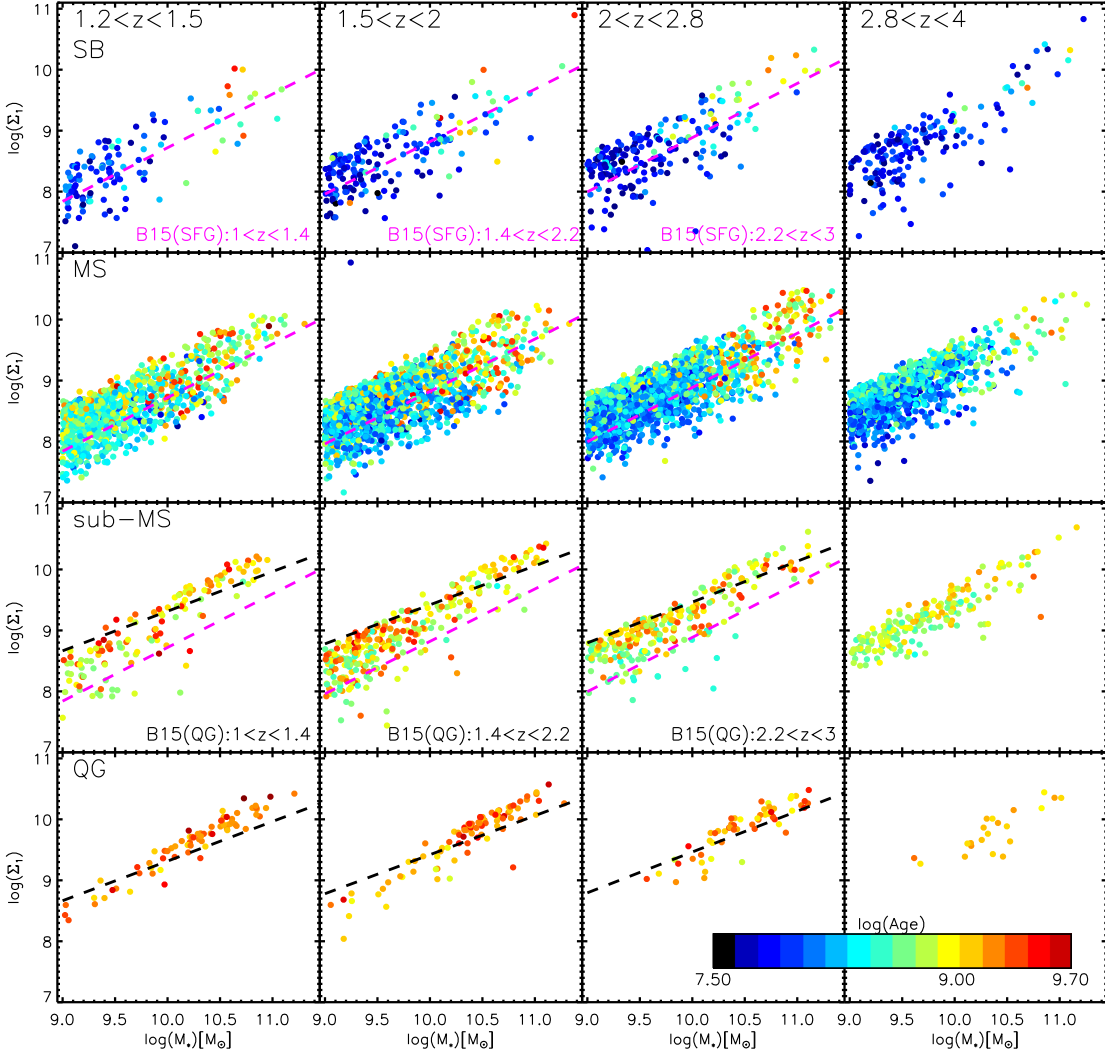
Figure 21. Projected central mass density vs. stellar mass for four galaxy populations relative to the MS at four redshift bins. The median-mass-weighted stellar age is color-coded. The best-fit relation for UVJ selected QGs (black dashed line) from Barro et al. (2017) are overplotted in the bottom panel (QG galaxies). For SB and MS galaxies, the best-fit relation for UVJ selected SFGs (magenta dashed line) from Barro et al. (2017) are used while best-fit relations for both SFG and QG are overplotted for sub-MS galaxies. Narrower dispersion of Σ_1 with M_* represents that different quenching processes play a role at low and large masses (cf. sub-MS panels).
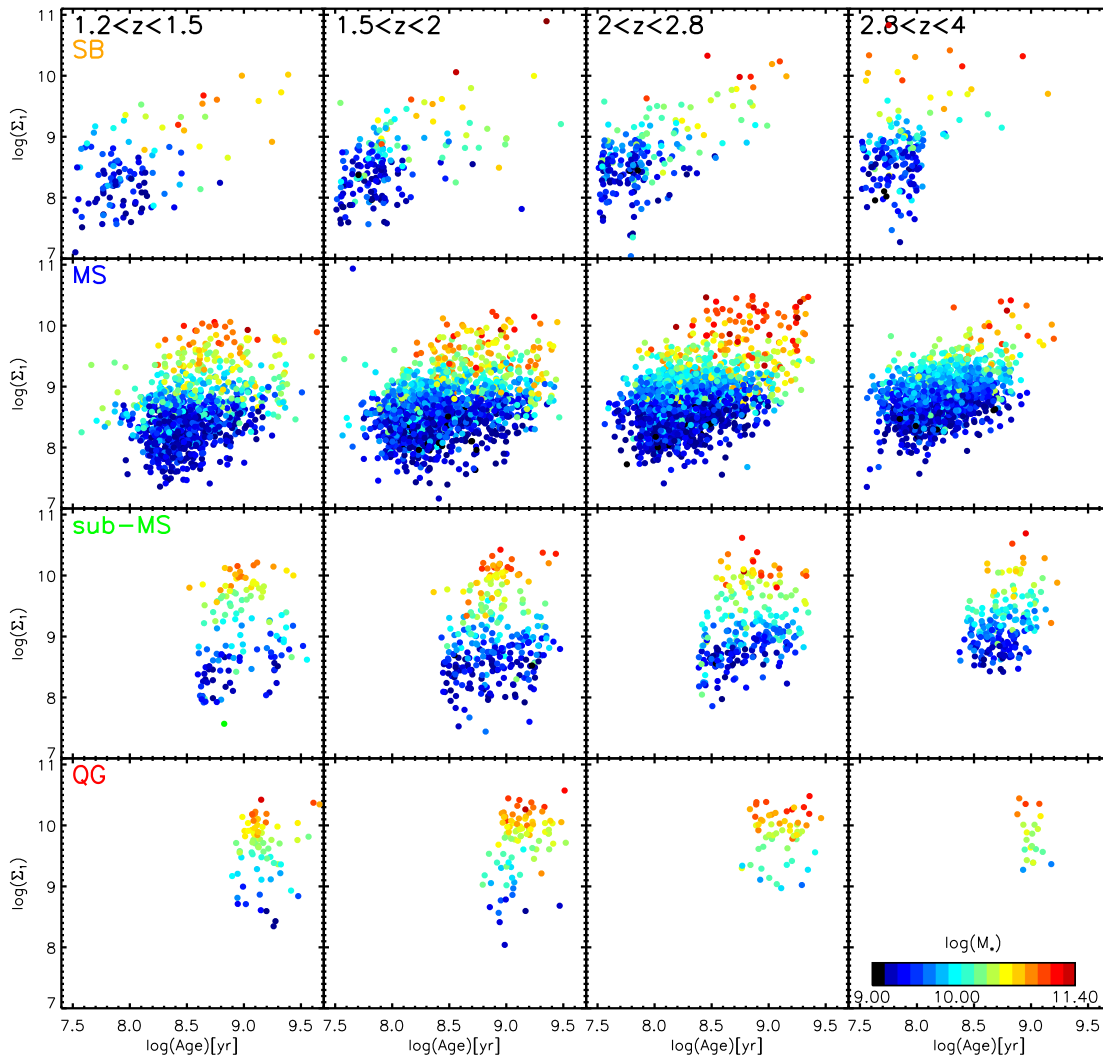
Figure 22. Projected central mass density (Σ_1) vs. median-mass-weighted stellar age (Age) for four galaxy populations relative to the MS at four redshift bins. The stellar mass is color-coded. When galaxies are in the MS and SB regions, both Σ_1 and M_* increase with increasing stellar age. But when they are quenched, the growth of both Σ_1 and M_* stops and the correlation with ages ends. Thus, QGs show a "vertical" shape in the bottom panel.

mergers observed during the burst of star formation, the compact source would be consistent with the remnant of a highly dissipative gas process (Hopkins et al. 2008; Wuyts et al. 2010). The problem is how to get rid of the extended stellar component during a purely passive transition into the quenching phase (van Dokkum et al. 2008; Cassata et al. 2011, 2013), since the light profile of most massive QGs is that of a "naked" nugget and is quite different from that of the starburst galaxies, as shown in Figure 19. We caution, however, that it is not clear if the simulations of wet mergers have sampled a large enough volume of the parameter space of the progenitors such that compact passive galaxies consistent with the observations can still be produced, and/or if the observations have reached the sensitivity to rule out low surface brightness extended halos.

7.2. Evolution of Galaxies in the log(SFR)–log(M$_*$) Plane and Morphological Transformation

Do galaxies transform their morphology as their stellar mass grows and their star formation activity evolves and

eventually quenches? Or, stated differently, is morphological transformation implied by the observed trends of morphology, stellar age, and position on and around the MS at $1.2 < z < 4$? As others before us, we also find that the distribution of the projected central density Σ_1 narrows toward the top end of the overall distribution as galaxies move away and below from the MS. We did not find any evidence that this is the result of a fading disk, which would leave the compact bulge as visible evidence. In other words, it is unlikely that compact quiescent galaxies form directly from normal SFGs on the MS through simple disk fading, as the star formation fades. Wellons et al. (2015) tracked the assembly histories of compact quiescent galaxies at $z = 2$ in the Illustris simulation, and found that there are two dominant mechanisms of formation of compact quiescent galaxies: (1) compact galaxies form via starbursts from major mergers between $z \sim 2 - 4$, or (2) compact galaxies form at very early epochs and maintain their morphologies until $z \sim 2$. Based on our observational findings (Section 7.1.3 and Figure 19), the first scenario seems unlikely, since starbursts, the most likely candidates for wet mergers, are characterized by a significant amount of diffuse light around
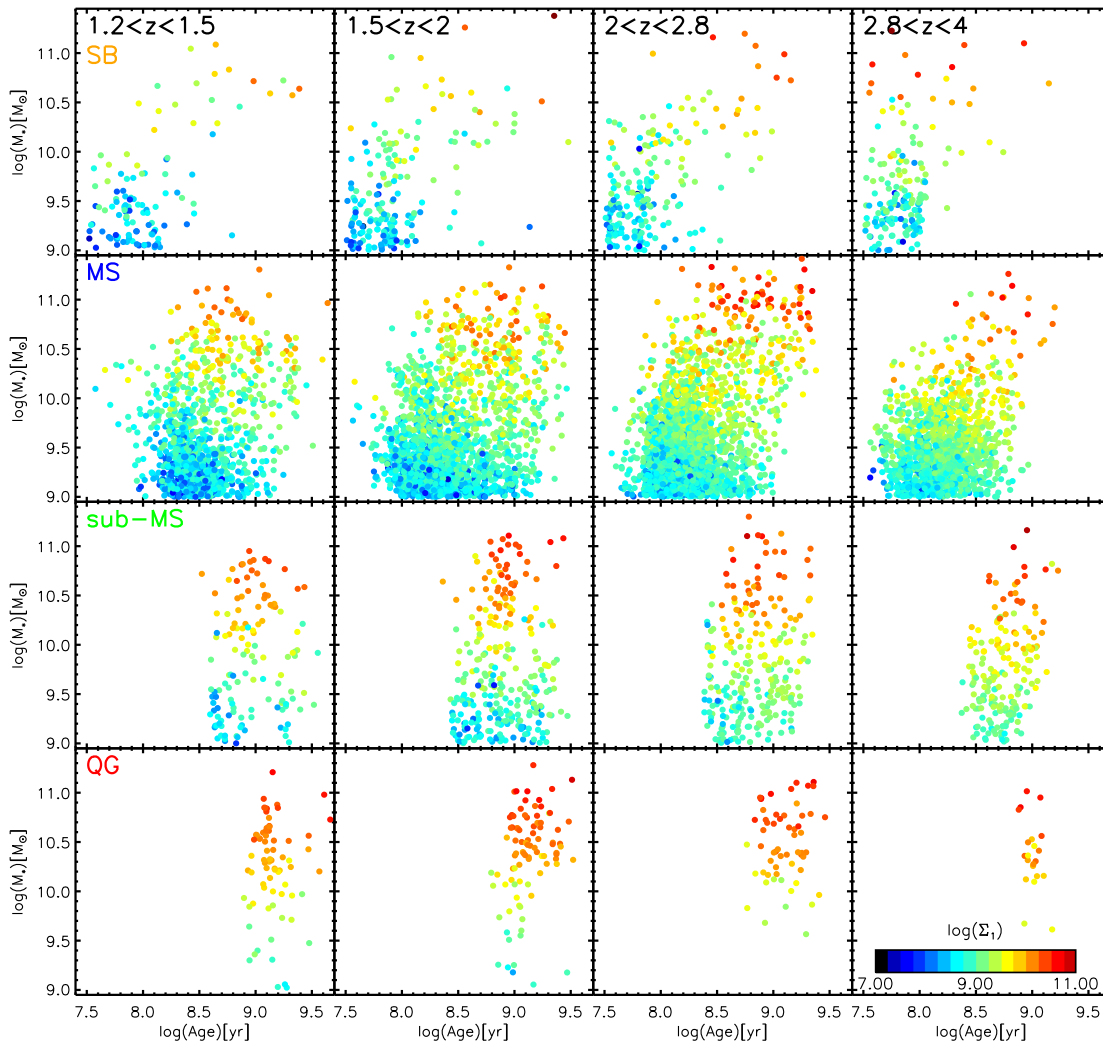
Figure 23. Stellar mass (M_* vs. median-mass-weighted stellar age (Age) for four galaxy populations relative to the MS at four redshift bins. The projected central mass density is color-coded. As stellar age increases, galaxies become more massive and their central density increases. But, the correlation between M_* and Age is no longer exist, once galaxies stop their star formation.

the compact central source, presumably tidal debris, stripped stars and in general the violently relaxed stellar component, which seems not to be observed in compact quenched galaxies, either individually or in very deep stacked images. The alternative scenario suggested by our findings is that a significant fraction of the compact massive galaxies that dominate the counts at $z \sim 2$ assemble at earlier times when the universe was denser, and subsequently evolve mostly through in situ star formation keeping their compact morphologies (Williams et al. 2014, 2017; van Dokkum et al. 2015; Lilly & Carollo 2016).

We investigate the relationship between Σ_1 and stellar mass as a function of stellar age in our four redshift bins for star-forming and quiescent galaxies selected in the UVJ plane and relative to their distance from the MS, respectively, in Figures 20 and 21. Our measures are in good agreement with the analogous ones by Barro et al. (2017), and, for comparison, in the figures we display their best-fit over-plotted to our data in the redshift bins in common. There is a clear correlation between central density and stellar mass, which becomes tighter for galaxies with decreasing activity of star formation. Compared to Barro et al. (2017), our

analysis adds the extra dimension of stellar age, which shows that (1) at fixed stellar mass galaxies with higher central density tend to be older, and (2) at larger stellar mass and hence larger central density galaxies tend to be older. Since the distribution of Σ_1 is nearly constant with redshift at all mass (Figure 14), the implication is that as galaxies form stars, both their stellar mass and central stellar density grow, and the growth continues until the central density enters in a relatively narrow range of values, at which point the growth stops and galaxies quench.

We additionally study the correlation between Σ_1 and age in Figure 22, where the points representing the galaxies have been color-coded with their stellar masses and the correlation between stellar mass and age, with the points color-coded according to the value of Σ_1 in Figure 23. Both figures show that, as galaxies form stars (i.e., when they are in the MS and SB regions), both Σ_1 and M_* increase with increasing stellar age. Namely, during the star formation phase galaxies become both more massive and their central density increases as time increases. As galaxies start to quench, the correlations with ages becomes weaker. However, galaxies with older ages are more massive and also have larger central density Σ_1. Once
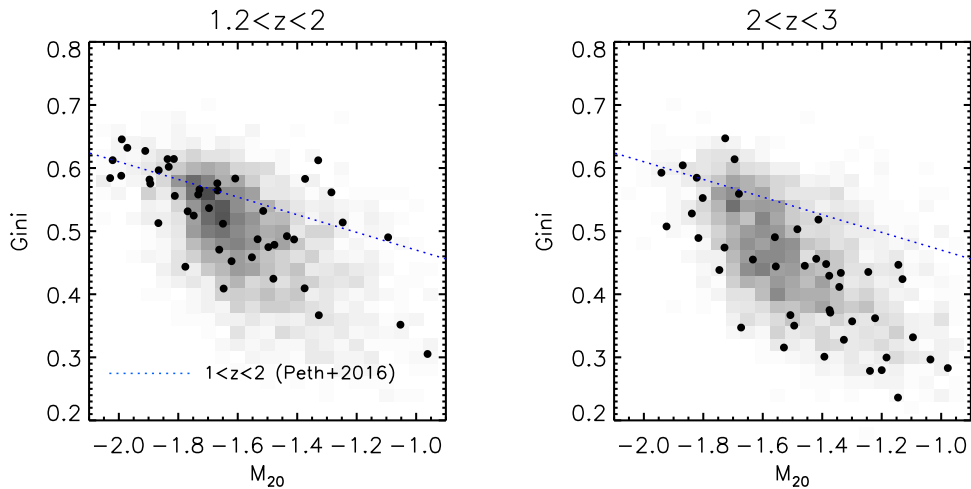
Figure 24. Gini vs. M_{20} for old main sequence galaxies (black points) at two redshift bins. We find no galaxy with Age > 1 Gyr and $M_* > 3 \times 10^{10}\, M_\odot$ in the main sequence at $z > 3$. The distribution of all main sequence galaxies is colored according to the density of sources. The darkest color represents densest regions. We overplot the definition of mergers of $1 < z < 2$ galaxies from Peth et al. (2016; blue dotted line). We find that there is no difference in galaxy morphologies of old MS galaxies (black points) and the rest of the galaxies in the MS.

galaxies have ceased star formation, the growth of both Σ_1 and M_* stops and the correlations with ages ends as well. The plots for QGs become "vertical" (the bottom panels in Figures 22 and 23) because stellar age differences are become smaller and harder to measure relative to the large absolute age of the galaxies.

Of the three variables (Age, Σ_1, and M_*), Age should naturally be the independent one. Indeed, our results show that both stellar mass and central density increase with age as galaxies evolve: stellar mass reflects the history of star formation and Σ_1 reflects the history of dissipative gas accretion in galaxies. However, more massive galaxies are also more efficient at promoting dissipative gas accretion, which results in the relatively tight correlation between Σ_1 and M_*. But while the measures of Σ_1 and M_* are relatively accurate, the measures of stellar age are comparatively noisier, which washes out a bit of the correlation between age and the other two variables.

In conclusion, the scaling relationship of Σ_1 and stellar mass and their evolution with redshift for massive galaxies show that massive galaxies quench when their central density (Σ_1) how grown to value in a narrow range from the maximum observed one (which is mass dependent), and the narrowness, threshold (for quenching), and maximum value are essentially independent from redshift, as also argued by Barro et al. (2017). Note that this *does not* imply any causal relationship between high core density and quenching: the two phenomena simply happen together at some point during the growth of a galaxy. Qualitatively, the larger dispersion of Σ_1 values at fixed stellar mass observed in star-forming galaxies simply reflects the different points in times during their evolution when the galaxies are observed, as evidenced by the trend that at fixed stellar mass older galaxies have larger central density. If a galaxy can keep growing in mass, it eventually reaches a critical size, approximately log $(M_*) \approx 10.5 - 11$ (see also Peng et al. 2010; Lilly et al. 2013), at which point the probability that it quenches rapidly increases with the mass, with the quenching caused by something that happens when the galaxy reaches that stellar mass. At large mass, the relatively narrow dispersion of Σ_1 suggests that the quenching is probably caused by processes
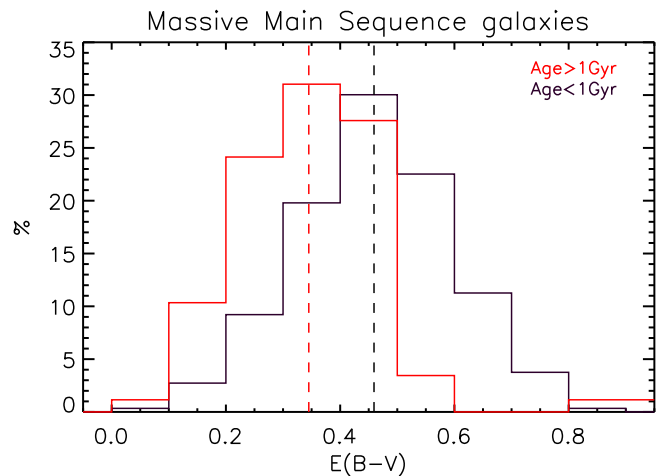

Figure 25. Distribution of the values of the best-fit $E(B - V)$ parameter for massive ($M_*/M_\odot > 3 \times 10^{10}$) MS galaxies in the two age bins that define the old MS galaxies. The $E(B - V)$ distributions of the two groups of galaxies are similar in shape, but the peak of that of the old galaxies is ≈ 0.1 smaller. This is an indication of the age-obscuration degeneracy of SED fitting procedures. The older fitted age and the smaller $E(B - V)$ color excess of old MS galaxies are within the covariance of the degeneracy between age and obscuration of our SED fitting procedure.

internal to the galaxies and the quenching probability is a steep function of the mass (small dispersion). This trend is particularly evident in the sub-MS panel of Figures 21–23 (i.e., "quenching" galaxies). Quenching, however, could also happen for other reasons before the galaxy reaches the critical size, and this seems suggested by the larger scatter in the Σ_1 versus M_* relationship (cf. sub-MS panel) at lower masses. In this case, quenching would be caused by something external to the galaxies (environmental quenching). Evidence that environmental quenching plays a role in shaping the red sequence has been found by Quadri et al. (2012). More recently, Tal et al. (2014), Guo. et al. (2017), and our recently submitted work T. Ji et al. (2018, in preparation) found direct evidence of environmental quenching in low-mass ($\approx 10^9 M_\odot$) galaxies up to $z \sim 2.5$. (T. Ji et al.
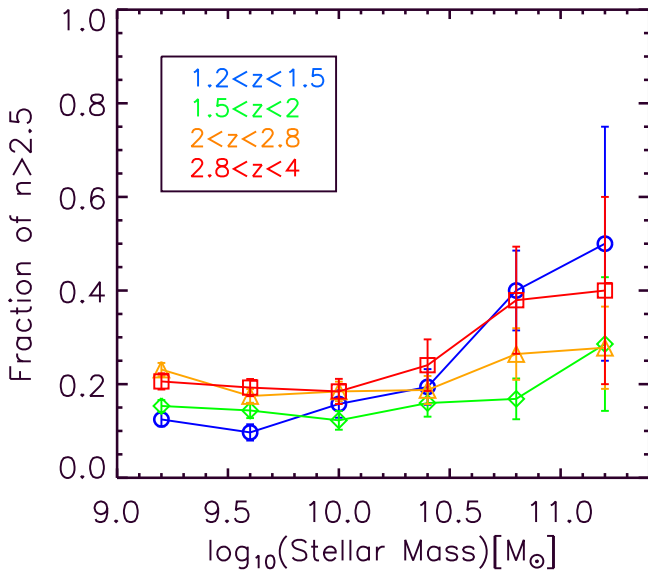
Figure 26. Fraction of SFGs having Sérsic index (n) >2.5 as a function of the stellar mass (with $\Delta \log(M_*) = 0.4$) for four redshift bins. We find a weak increase of the fraction of bulge-dominant galaxies ($n > 2.5$) at all explored redshifts. The error bar represented here is 1σ uncertainties based on Poisson statistics.

2018, in preparation) reach the same conclusions with Quadri et al. (2012) that the environment plays a greater role in assembling the red sequence for low-mass galaxies than more massive ones (for which other mechanisms control quenching), based on both clustering arguments and on the quenched fraction as a function of stellar mass, which rapidly increases with stellar mass and peaks around the critical value $\log(M_*) \approx 10.5$–11. Taken together with the former argument about the internal process and the other evidence of environmental quenching, the thickening of the dispersion of the Σ_1 versus stellar mass relationship at lower masses is therefore "consistent" with external quenching mechanisms that become more and more important at lower masses. Summarizing, we suggest the possibility that external mechanisms, most likely related to the environment, effectively quench the galaxies before internal ones, freezing the central density at the current value, which is lower than the one the galaxy would have if it was possible for it to quench by internal mechanisms.

7.3. Old Galaxies in the Main Sequence

The addition of the "third dimension" of age (median-mass-weighted stellar age) to the $\log(SFR)$ versus $\log(M_*)$ plane reveals the presence of galaxies with old stellar age (i.e., $Age > 10^9$ year), still on the main sequence. These old MS galaxies are observed in both mass bins considered here, but seem to be more common among the massive galaxies ($M_*/M_\odot > 3 \times 10^{10}$: 29.7%) than in the low-mass ones ($M_*/M_\odot < 3 \times 10^{10}$: 3.7%). In the high-mass bin, they appear to span the full range of Σ_1 values, and seem to be most abundant at $1.5 < z < 2.8$, while they are nearly absent in the highest redshift bin. Among the low-mass galaxies, they seem confined to high Σ_1 values and their number progressively increases with decreasing redshift (i.e., increasing cosmic time, perhaps signaling a genuine aging

of the star-forming galaxies as they approach the quenching phase).

We further investigate the nature of the massive old MS galaxies to explore the possibility that they are somewhat different from the rest of the MS galaxies of similar mass. As Figure 16 shows, these galaxies do not preferentially occupy a special region of the MS, and in particular, they do not sit near the lower boundary of the MS, closer to the quenching region. A look at the best-fit SFH of these galaxies shows the same distribution of the five analytic functions that we have used as in the rest of the MS.

We also look at their morphology and make a visual inspection to search for evidence of an excess of mergers or interacting systems, finding that these galaxies seem similar to the rest of those in the MS. More quantitatively, a number of studies (Lotz et al. 2004, 2008; Peth et al. 2016) have shown that the Gini and M_{20} coefficients provide useful diagnostics of merging and interaction at $z < 2$. Following their results, we use the G–M_{20} diagram to inspect the incidence of mergers among massive old MS galaxies at $1 < z < 2$ using the definition of from Peth et al. (2016), who suggested that most of the mergers at these redshifts are located above the blue dotted line in the left panel of Figure 24. As the figure shows, there is no evidence that the relative distributions of the old galaxies and of the rest of the MS differ, both at $1.2 < z < 2$, where the index was calibrated, and also at $2 < z < 3$. This confirms the visual analysis that the frequency of merging events and/or of interactions among the old MS galaxies is the same as that of the rest of the MS. This suggests that the old age derived in our fitting procedure is unlikely to be the result of rejuvenation effects of passive galaxies due to merging events, although the accretion of gas or of very faint gas-rich satellites cannot be excluded.

Additionally, we look at the fraction of AGN classified from the latest deep *Chandra* images in GOODS North by Xue et al. (2016) and by Luo et al. (2017) in GOODS-South. AGN hosts are classified among X-ray sources if they satisfy one of the six criteria listed in Luo et al. (2017) (see Section 4.7, paragraph 2). There are 97/380 AGN hosts among massive galaxies in the MS—namely 26% with a Poisson uncertainty, 0.03. Among the old galaxies, there are 16/87 AGN hosts (i.e., 18% with a poison uncertainty, 0.04). These numbers show no evidence that AGN activity among the old MS galaxies is different from the rest of the MS.

We observe, however, a difference in the distribution of the values of $E(B - V)$ from the best-fit SED procedure among the two groups of galaxies. As Figure 25 shows, while the shape of the two distributions is rather similar, the peak of the old galaxies' one is ≈ 0.1 smaller, very likely a manifestation of the age-obscuration degeneracy of SED fitting procedures based on broad-band photometry, no matter how deep or accurate. We conclude that most likely there is no intrinsic difference in the physical properties of what we called "old MS galaxies" (i.e., galaxies whose best-fit stellar age is larger than 1 Gyr) and the rest of the galaxies in the MS. The older fitted age and the smaller $E(B - V)$ color excess are within the covariance of the degeneracy between age and obscuration of our SED fitting procedure.
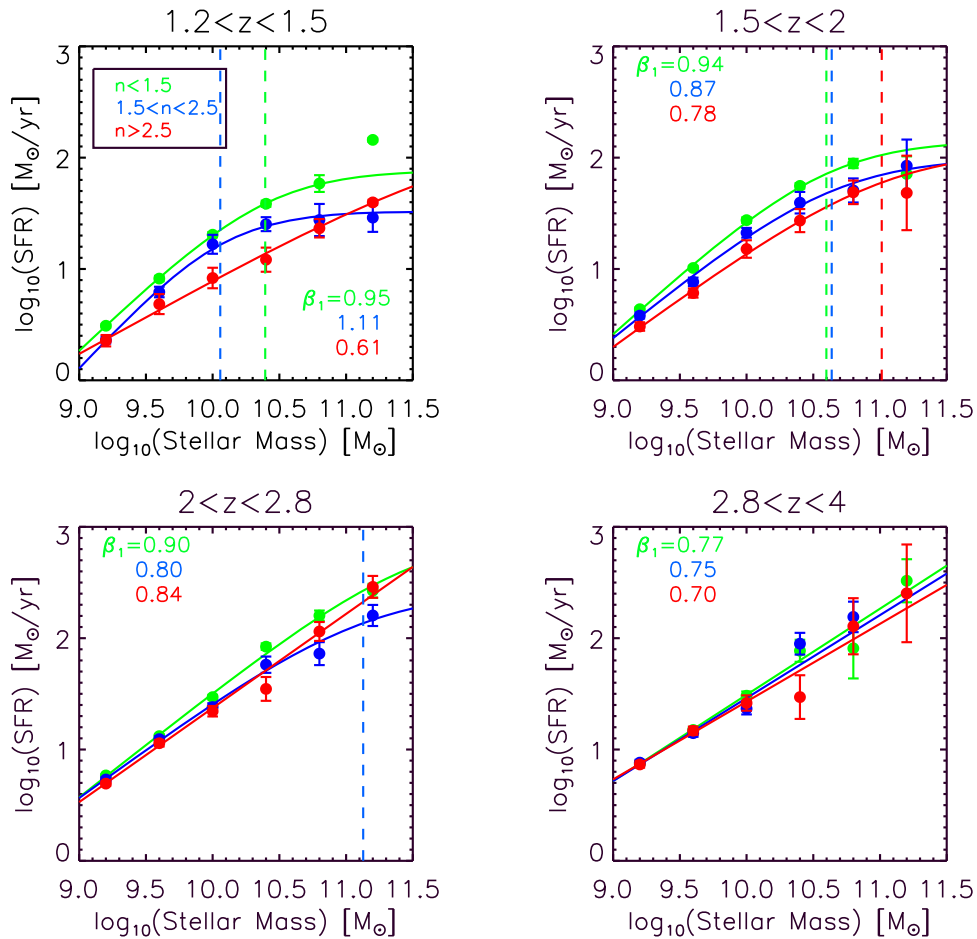
Figure 27. MS of SFGs having different Sérsic indexes: we classify galaxies into three classes, $n < 1.5$ (green), $1.5 < n < 2.5$ (blue), and $n > 2.5$ (red), and then fit the slope of the $\log(\mathrm{SFR})$–$\log(M_\star)$ relation separately with the standard error ($\sigma/\sqrt{N}$). The vertical line represents M_0 of each population, and β_1 is the MS slope below M_0 or the slope in case of explained by a single power-law. Note that there is no galaxy having $M_\star > 10^{11} M_\odot$ and $1.5 < n < 2.5$ at $2.8 < z < 4$. Also, at $1.2 < z < 1.5$, the most massive bin of $n < 1.5$ is excluded from a fit because of a poor statistic (only two galaxies having almost identical SFR values).

7.4. Does the MS Slope Depend on Morphologies of Galaxies?

In Section 4, we show that the bending of the MS slope is a function of redshift and is prominent at $z < 2$. By $z \sim 2$, the slope is close to ~ 0.8 at all stellar masses. The bending of the MS implies that massive galaxies are experiencing a decrease of SF (i.e., massive galaxies have lower sSFR relative to less massive galaxies). The reason for this bending of the MS is yet uncertain. Abramson et al. (2014) showed that MS slope is almost unity without a bending of the MS in the local universe when they use M_{disk} instead of $M_\star$. This suggests that including bulge components might cause the bending of the MS at high masses, since the bulge does not contribute significantly to SF. Lang et al. (2014) also concluded that the bulge growth at high masses leads to the departure of the MS slope from unity using the CANDELS/3D-*HST*. Recently, Schreiber et al. (2016) extended this study out to $z = 1$ by measuring the slope of the SFR–M_{disk} relation. In disagreement with previous studies, they found a flattening of the MS at high masses using M_{disk} and concluded that the secular growth of quiescent bulges in SFGs is not the main driver for the change of the MS, at least at $z = 1$.

To test for a possible relationship between the bulge growth and the bending of the MS at high masses, we use the Sérsic

index to broadly classify disk-like and spheroid-like galaxies. Sérsic index has been widely used to distinguish early-type quiescent galaxies with $n > 2.5$ (Kajisawa et al. 2015) and star-forming galaxies with $n < 1.5$ (Shibuya et al. 2015). We compute the fraction of bulge-dominant galaxies, simply identified as SFGs having $n > 2.5$, as a function of stellar masses in Figure 26. There is a weak increment of the fraction of $n > 2.5$ over all stellar masses at all explored redshifts. However, it is insufficient to support the idea that higher bulge fractions at high masses cause the bending of the MS due to small number statistics (large error bars at the massive end).

We further study whether the break of the MS depends on morphologies in Figure 27. Here, SFGs are separated into galaxies having disky ($n < 1.5$), intermediate ($1.5 < n < 2.5$), and bulge-dominant structures ($n > 2.5$). Because we do not see a depression in the slope at the massive end at $z > 2$, we do not expect to see a trend with morphology at these redshifts. If the bulge growth in a massive galaxy at $z < 2$ is a key driver of the decrease of the MS slope at high masses, the MS slope measured only using galaxies having $n > 2.5$ is expected to show the bending of the MS, and it should be different from one measured using galaxies having $n < 1.5$. However, we find that the bending of the MS is evident for galaxies having $n < 1.5$ and $1.5 < n < 2.5$ out to $z = 2$, while the MS of

galaxies having $n > 2.5$ is rather explained by a single power-law, except for galaxies at $1.5 < z < 2$. At $z < 2$, $n < 1.5$ have relatively steeper slopes (see β_1 in the Figure 27) and higher SFRs at a given stellar masses on average than $n > 2.5$. But the average SFRs at the highest mass bin weakly depend on n, indicating that massive galaxies have lower SFRs irrespective of their morphologies. Apparently, the MS does not depend on galaxy morphologies based on Sérsic index. Whitaker et al. (2015) also reported the weak dependence on n at $z < 1$ among star-forming galaxies, but do not see strong evidence at $z > 1$. They suggested that bulges in massive $z \sim 2$ galaxies are actively building up and the stars in the bulges are relatively younger than old bulges within SFGs at $z < 1$. However, using gas masses estimated by stacking *Herschel* data, Schreiber et al. (2016) provided evidence that the low sSFRs in massive galaxies on the MS are caused by a slow downfall of the star formation efficiency (SFE = SFR/M_{gas}) at $z < 2$, and not by the growth of bulges.

In sum, we do not find evidence that the inclusion of galaxies having bulge-dominant structures causes the bending of the MS at $1.2 < z < 2$. Rather, massive galaxies have relatively lower SFRs on average, regardless of their morphologies. This is consistent with the notion that the decrease of SF, and ultimately quenching, is driven by internal processes (e.g., AGN and/or stellar feedback), which depend on the mass of the galaxy (mass quenching: Peng et al. 2010, 2012; Lilly et al. 2013; Lilly & Carollo 2016).

8. Summary

We have studied the morphology and stellar ages of galaxies located on and around the main sequence of star formation in the log(SFR)–log(M_*) plane at $1.2 < z < 4$. In order to constrain the MS more accurately, we have re-measured the physical properties of galaxies (stellar mass, age, SFR) using new SED fitting procedures. In our adopted methodology, we explore five analytical star formation history models (constant SFR; linearly increasing; exponentially increasing; delayed; exponentially decreasing) and find the Best Fit SFH for individual galaxies. We test this "Best Fit SFH" procedure using mock galaxies from high-resolution N-body simulations coupled to the semi-analytical models. We find that the Best Fit SFH procedure recovers the intrinsic properties of the galaxies more accurately than using one fixed SFH for all galaxies. Our key results are summarized as follows:

1. At $z < 2.8$, the main sequence (MS) observed in this study is tight with a constant dispersion, $\sigma \sim 0.37$ dex, and the slope is curved at the turnover mass, M_0, which mildly increases from $10^{10.6}$ to $10^{11.5} M_\odot$ with redshifts. At $z < 2$, below M_0, the MS slope is about 0.85–1.0, and the slope becomes flattened above the turnover mass. The MS of galaxies at $2 < z < 4$ is rather explained by a single power-law, with the slope ~ 0.8, and the dispersion of the MS is higher than one for lower redshifts. With the carefully measured MS, we classify galaxies into four populations based on their positions in the log(SFR)–log(M_*) plane, using starburstiness, R_{SB}: starbursts 1-σ above the MS, star-forming galaxies on the MS, sub-MS galaxies located 1-σ below the MS, and the quiescent galaxies.

2. We identify a significant number of galaxies located below the MS (sub-MS) having intermediate rest-frame colors and morphologies between the quiescent galaxies and star-forming galaxies on the MS. These galaxies have lower $E(B–V)$ than MS galaxies on average, supporting that the sub-MS galaxies may be under transition from normal star-forming to the quiescent population. In particular, among the sub-MS galaxies with $M_* > 3 \times 10^{10} M_\odot$, most of them are compact ($\Sigma_1 > 10^{9.5} M_*/\text{kpc}^2$). These galaxies are systematically older than normal star-forming galaxies at same stellar masses.

3. Using both traditional diagnostics of morphology (Sérsic index n, R_e, and Σ_1), as well non-parametric (Gini and M_{20} coefficients), we observe clear morphological differences among galaxies located in different locations in the log(SFR)–log(M_*) plane, which also correlate with stellar age. In particular, we reproduce the trends between the projected central mass density (Σ_1) and R_{SB}: as the star formation activity decreases (i.e., R_{SB} decreases) and galaxies become older, the spread of Σ_1 becomes narrower and confined to the top end of the global distribution at all explored redshifts. The projected central density gets compressed toward an upper limit at low R_{SB}. This upper limit does not change with redshift, but it depends on the stellar mass of the galaxies.

4. We find a general trend between the galaxies' median-mass-weighted stellar age and their position relative to the MS, where the age steadily increases for galaxies located at increasingly lowers SFRs below the MS. Galaxies on the MS, however, have Σ_1 that spans a broad range of values (i.e., SFGs with high Σ_1 are not older than SFGs with lower central densities). Thus the central stellar density of galaxies spans a relatively large dynamic range of values while they are on the MS (i.e., they are during the star-forming phase). The dynamic range becomes restricted (to about $1/4$ in Log space) toward the high end of the distribution as galaxies quench and become passive. We stress that this growth of the stellar mass density of the central regions, which reflects of history of dissipation that took place in each galaxy, is not necessarily causally connected with the quenching process.

5. Stacks of light profiles of massive, compact quenched/quenching galaxies at $z \sim 2.5$ do not show evidence for faded disks in their outskirts. The lack of the extended stellar halos, namely the violently relaxed stellar component of the merging galaxies, around the compact quiescent galaxies suggests that these galaxies are unlikely the remnants of highly dissipative wet mergers, unless the stellar contents of the merging galaxies was so small to remain undetected in existing images. This interpretation is consistent with the presence of extended light in starburst galaxies, which probably formed via gas-rich major merging. We find that in general the light distribution of starburst galaxies is significantly more diffuse and their size larger than compact passive galaxies. Massive, compact starbursts ($M_*/M_\odot > 3 \times 10^{10}$ and log(Σ_1) > 9.5) are rare and *essentially* do not exist at lower redshifts. Therefore, it

is unlikely that starbursts can shrink their size to match that of compact quiescent galaxies within a short timescale.

6. By adding the stellar age as a third dimension in the Σ_1 and M_* plane, we show that older galaxies have a larger central density at fixed stellar mass, and the dispersion of Σ_1 observed in the star-forming galaxies is relatively larger than one for galaxies with decreasing activity of star formation. As galaxies evolve in size and mass by forming stars, their central density also increases with age, reflecting the integrated history of dissipation that they underwent. The shrinking of the dispersion of Σ_1 after quenching depends on the stellar mass, with more massive galaxies showing a smaller dispersion. Together with independent evidence of environmental quenching of smaller mass satellites around more massive centrals (e.g., Guo. et al. 2017; T. Ji et al. 2018, in preparation), this can be interpreted as evidence that different quenching processes are at work at different mass regimes. At large mass, the quenching is caused by processing internal to the galaxies that depends on the galaxy's reaching a particular value of the stellar mass, while at lower mass is related to the environment, namely when the quenching takes place is independent on the stellar mass that the galaxy has grown up to that moment.

7. The flattening of the MS at high masses persists even when we examine only the disk-dominated galaxies (having $n < 1.5$). At $z < 2$, we find no significant difference in the MS slopes between the spheroid-dominated ($n > 2.5$) and disk-dominated ($n < 1.5$) galaxies. Furthermore, we find that the average SFR for the highest mass bin rarely depends on the Sérisc index, indicating that massive galaxies have low SFRs regardless of their morphologies. We suggest that the decrease in SFR at high masses (e.g., star formation quenching) is not driven by the bulge growth, but it is the result of internal processes, which is dependent on the stellar masses.

Based on our empirical study of the morphologies of galaxies and their stellar age at $1.2 < z < 4$, we suggest that the monotonic increase of projected central mass density (i.e., growth of the central parts of the galaxies) as galaxies grow is an indication of a general phenomenon of structural transformation of galaxies. Massive, compact galaxies observed at $z \sim 2$ are simply assembled at very early times and evolve through in situ star formation to form compact quiescent galaxies. Instead of major wet merging events, a direct accretion of cold gas can drive the formation of massive, compact galaxies, either via violent disk

instabilities in a compact disk or direct cold mode accretion of the gas traveling into the galaxy center and forming stars in situ.

In this paper, we focus on morphological analysis mostly using the projected central density in the log(SFR)–log(M_*) plane with an additional dimension, stellar age, to quantify the process of "compactification" of galaxies as they quench their star formation. However, it is insufficient to explain the overall features of the complex morphological evolution and transformation of a galaxy. In the second paper, we will complete the discussion of characteristics of galaxies in the log(SFR)–log(M_*) plane and their morphological evolution by comparing Σ_1 with the non-parametric morphological indicators, G and M_{20}.

Appendix A
A Weak Dependence of Magnitude Limits on the Analysis of Morphologies

Morphological parameters used in this study are sensitive to the magnitude, hence signal-to-noise ratio (Lotz et al. 2004; van der Wel et al. 2012). Using CANDELS 4-epoch data, van der Wel et al. (2012) found that the H-band magnitude limit for GALFIT is $H < 23.5$ for n and $H < 24.5$ for R_e, with galaxies fainter than these magnitude limits expected to produce biased results. Non-parametric measures can also be unreliable for faint sources, and they are generally robust for bright sources (Lotz et al. 2004). Using CANDELS/Deep fields (10-epoch), Grogin et al. (2011) suggested that morphologies of galaxies having $H < 24.7$ can be effectively identified using non-parametric measures.

Because our galaxy sample goes to lower stellar mass limits ($\sim 10^9 M_\odot$) and most of them have $H < 26$, it is important to understand how the limiting magnitude affects our morphological analysis. We use deeper images (10-epoch) than van der Wel et al. (2012), so the limiting magnitude for GALFIT is about 0.9 magnitudes deeper, which is $H = 25.4$ ($H = 24.4$) for R_e (n). About 92% (60%) of our sample have $H < 25.4$ ($H < 24.4$). In this section, we repeat the same analysis for all galaxy morphology measures used in this study, Sérsic index, R_e, Σ_1, Gini, and M_{20}, using
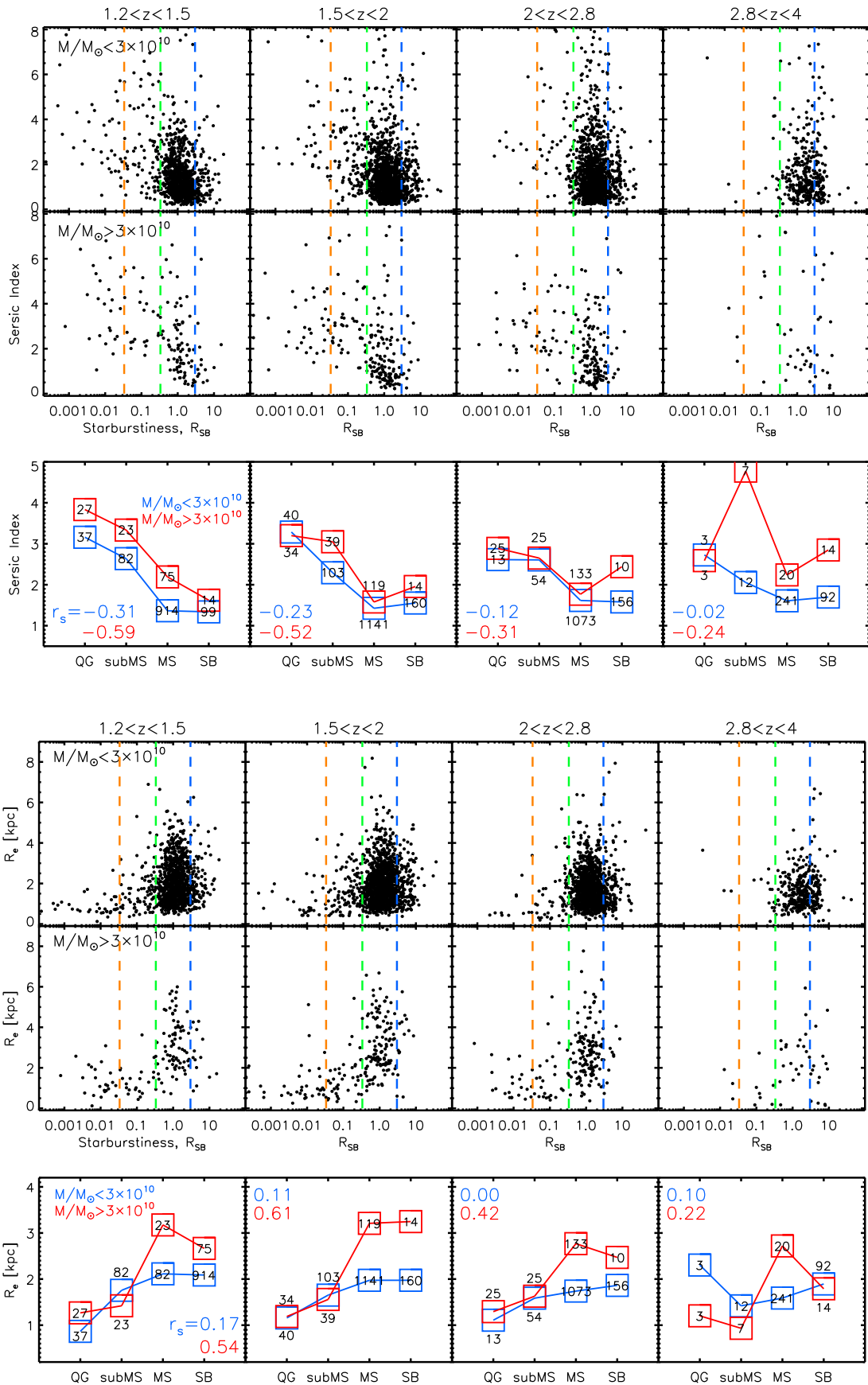
Figure 28. We study the correlation between R_{SB} and Sérsic index (top)/R_e (bottom) for four different galaxy populations on the log(SFR)–log(M_*) relation across four redshift bins using galaxies having $H < 24.4$. All lines, colors, and symbols correspond to the definitions in Figure 12. r_s is the Spearman's rank correlation coefficient between n/R_e and R_{SB} for each redshift and mass bin. r_s is almost identical to the one using all sample without limiting magnitude, indicating that restricting galaxy sample with its magnitude would not significantly change our morphological analysis.
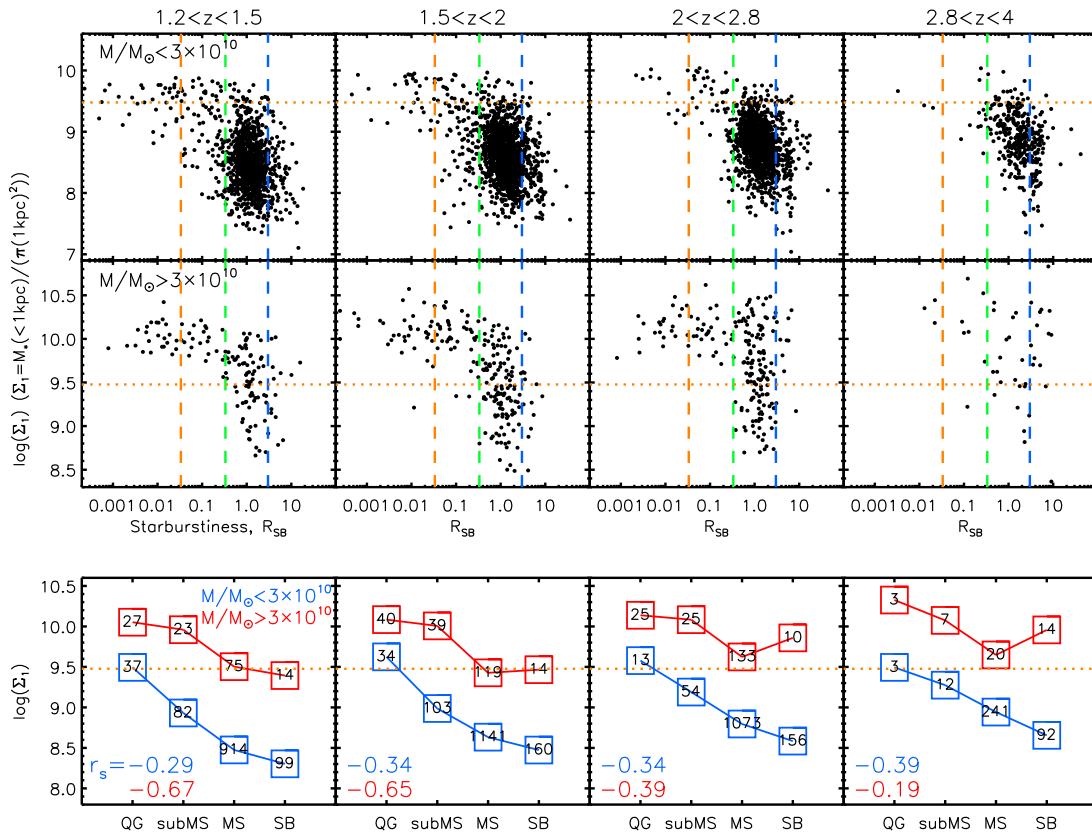
Figure 29. Extrapolated projected central density, Σ_1, vs. R_{SB} (two top panels) and the average of Σ_1 for the four galaxy populations (bottom panel) using galaxies having $H < 24.4$. The horizontal line is for the classification of high-central density galaxy, $\log(\Sigma_1) = 9.5$, from Barro et al. (2017).

only galaxies having $H < 24.4$ in Figures 28–30. The overall distribution of all morphological parameters looks less scattered than ones using entire sample without limiting magnitudes (Figures 12, 13, 15). However, the correlations between R_{SB} and morphological parameters (based on the

Spearman's rank correlation coefficient, r_s, are rarely changed at all redshifts and stellar masses. This suggests that our result does not suffer from this systematic bias. Therefore, throughout this paper, we do not limit the sample based on the galaxy's brightness.
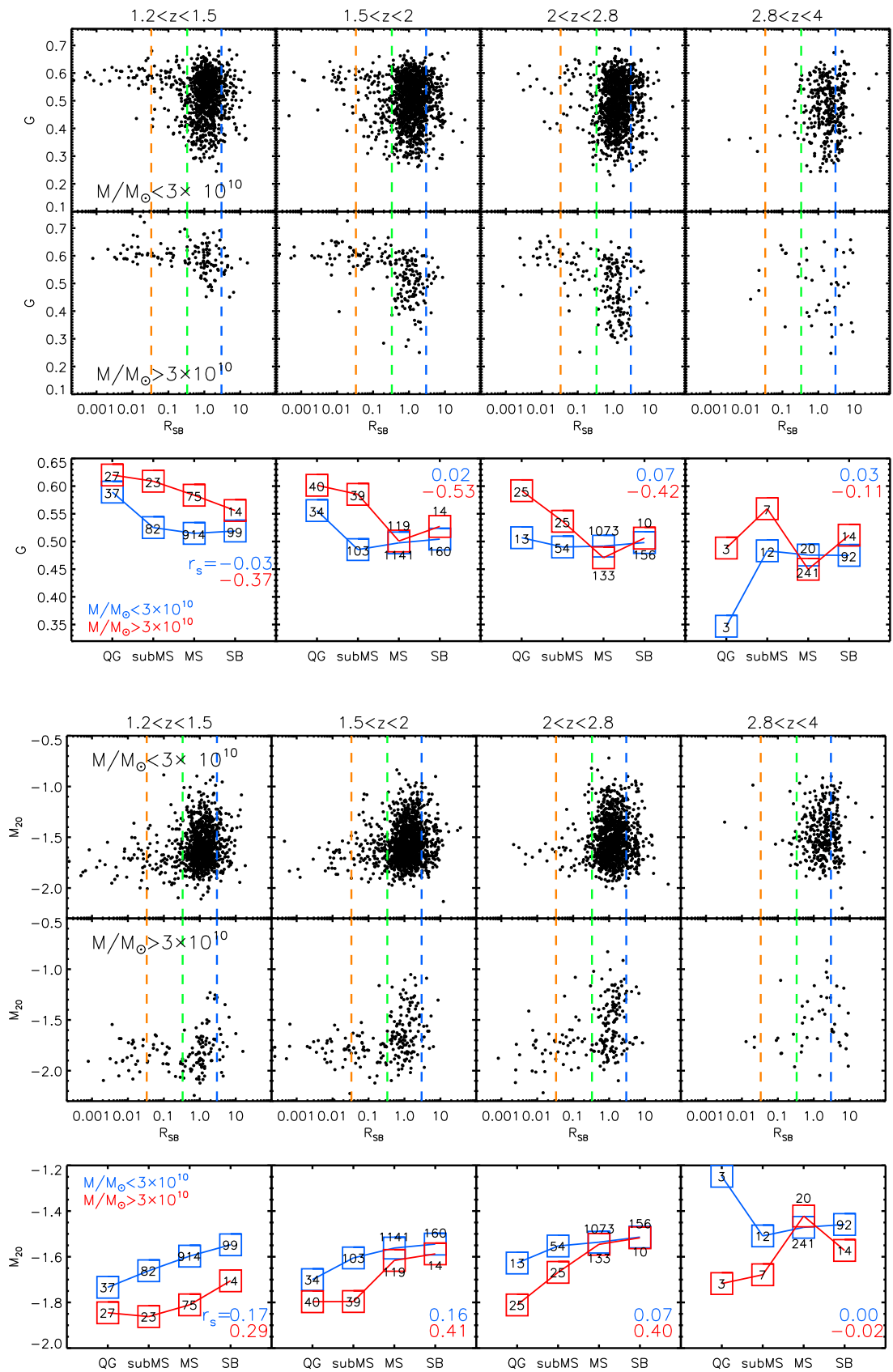
Figure 30. Top panels: Gini vs. R_{SB} using galaxies having $H < 24.4$. Bottom panels: M_{20} vs. R_{SB} using galaxies having $H < 24.4$. All lines, colors, and symbols correspond to Figure 28.

Appendix B
Σ_1 Versus Σ_{50}

We directly compare two projected mass densities in Figure 31. The majority of galaxies have higher Σ_1 than Σ_{50}, and all the galaxies with log (Σ_1) > 9.5 have log (Σ_{50}) > 9.5. There are some galaxies with $\Sigma_{50} > \Sigma_1$, most of which have R_e < 1 kpc. Hopkins et al. (2009) found that the maximum stellar surface density of any galactic systems is close to log (Σ_{max}) ∼ 11. But we find 15 galaxies with log (Σ_{50}) > 11.0, whereas Σ_1 never reaches Σ_{max}. Although these 15 galaxies are bright (all of them have H < 26 and 80% of them have H < 24.4), they are extraordinarily small, <0.3 kpc (<0.1 pixel). They might be unresolved relative to the point-spread function (PSF). Or, GALFIT Sérsic profile of these galaxies might be wrong because GALFIT cannot converge for galaxies with R_e < 0.5 pixel (Peng et al. 2010).

To reveal how well the projected mass densities represent the compactness of galaxies, we study the correlation between projected mass densities and non-parametric measures (G, M_{20}) by computing the Spearman's rank correlation coefficient, r_s. Because the parametric measures obtained from Sérsic profile fitting are already correlated with Σ_{50} and Σ_1, it is not worthy to study correlations between Sérsic index (or R_e) and densities. Statistically, Σ_1 is correlated with G and M_{20} better than Σ_{50} based on r_s. (The r_s between G and Σ_{50} [Σ_1] are 0.45 [0.49] and the r_s between M_{20} and Σ_{50} [Σ_1] are −0.25 [−0.43].) This correlation is also observed in the histogram of G and M_{20} in Figure 32. Galaxies having log (Σ_{50}) < 9.5 and log (Σ_1) > 9.5 (black histogram) show similar G and M_{20} distributions with those having log (Σ_{50}) > 9.5 and log (Σ_1) > 9.5 (red histogram). The average values of G (M_{20}) are 0.47 (−1.56), 0.52 (−1.69), and 0.57 (−1.70) for blue (all galaxies), black, and red histograms, respectively. Black and red histograms have very similar average values of G and M_{20}, indicating that
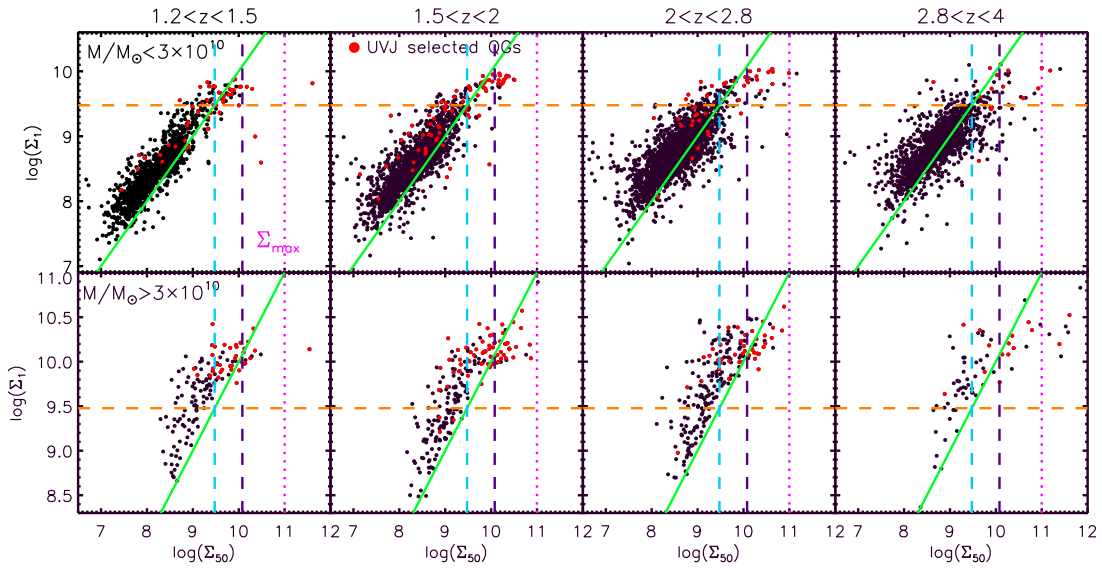
Figure 31. Σ_1 vs. Σ_{50}. The green line is the one-to-one correlation between Σ_1 and Σ_{50}. High density and ultra-high density threshold based on the Σ_{50} are sky blue and violet vertical lines. The orange horizontal line indicates log(Σ_1) = 9.5, and galaxies above this line are considered as high-central density galaxies. Σ_{max} is equal to $10^{11} M_\odot$/kpc^2, which is the maximum stellar density can be observed in any systems (Hopkins et al. 2009).
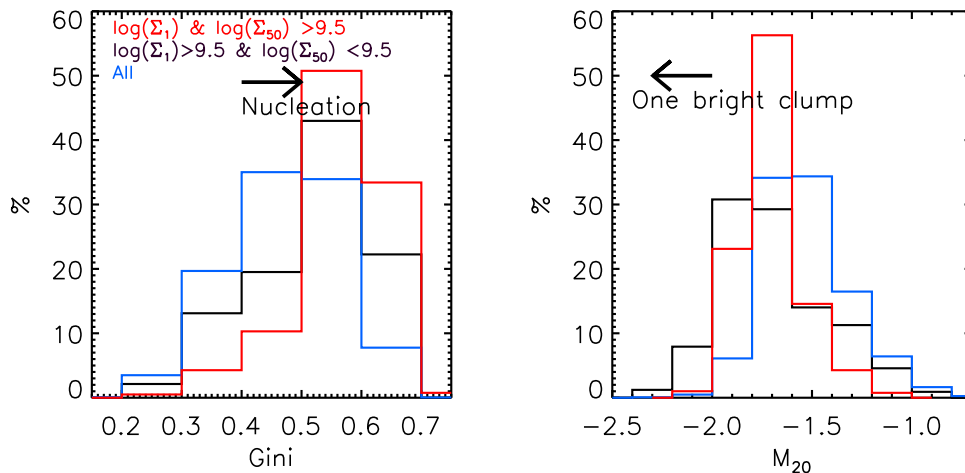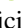

Figure 32. Relative distribution of G and M_{20} for all galaxies (blue), galaxies having log(Σ_1) and log(Σ_{50}) > 9.5 (red), galaxies having log(Σ_1) > 9.5 and log($\Sigma50$) < 9.5 (black). The mean values of G (M_{20}) are 0.47 (−1.56), 0.52 (−1.69), and 0.57 (−1.70) for blue, black, and red histograms. The black histogram has a similar distribution with the red one, indicating that these galaxies might be nucleated although their log (Σ_{50}) < 9.5.

these galaxies having $\log(\Sigma_1) > 9.5$ and $\log(\Sigma_{50}) < 9.5$ can be nucleated. It is possible to lose compact galaxies to some extent, only when Σ_{50} is used. Our results show that the compactness of a galaxy might be better explained by Σ_1 than Σ_{50}.

ORCID iDs

Bomee Lee ⓘ https://orcid.org/0000-0003-1954-5046
Mauro Giavalisco ⓘ https://orcid.org/0000-0002-7831-8751
Katherine Whitaker ⓘ https://orcid.org/0000-0001-7160-3632
Christina C. Williams ⓘ https://orcid.org/0000-0003-2919-7495
Henry C. Ferguson ⓘ https://orcid.org/0000-0001-7113-2738
Viviana Acquaviva ⓘ https://orcid.org/0000-0002-6788-6315
Anton M. Koekemoer ⓘ https://orcid.org/0000-0002-6610-2048
Yicheng Guo ⓘ https://orcid.org/0000-0003-2775-2002
Jeyhan S. Kartaltepe ⓘ https://orcid.org/0000-0001-9187-3605
Jennifer Lotz ⓘ https://orcid.org/0000-0003-3130-5643
Camilla Pacifici ⓘ https://orcid.org/0000-0003-4196-0617
Darren J. Croton ⓘ https://orcid.org/0000-0002-5009-512X
Yu Lu ⓘ https://orcid.org/0000-0003-2691-1622

References

Abraham, R. G., van den Bergh, S., & Nair, P. 2003, ApJ, 588, 218
Abramson, L. E., Kelson, D. D., Dressler, A., et al. 2014, ApJL, 785, 36
Acquaviva, V., Gawiser, E., & Guaita, L. 2011, ApJ, 737, 47
Acquaviva, V., Gawiser, E., & Guaita, L. 2012, in Proc. IAU Symp. 284, The Spectral Energy Distribution of Galaxies, ed. R. J. Tuffs & C. C. Popescu (Cambridge: Cambridge Univ. Press), 42
Alexander, D. M., Bauer, F. E., Brandt, W. N., et al. 2003, ApJ, 126, 539
Anders, P., & Fritze-v, A. U. 2003, A&A, 401, 1063
Arnouts, S., Le Floc'h, E., Chevallard, J., et al. 2013, A&A, 558, 67
Barro, G., Faber, S. M., Koo, D. C., et al. 2017, ApJ, 840, 47
Barro, G., Faber, S. M., Perez-Gonzalez, P. G., et al. 2013, ApJ, 765, 104
Barro, G., Trump, J. R., Koo, D. C., et al. 2014, ApJ, 795, 145
Behroozi, P. S., Wechsler, R. H., Wu, H.-Y., et al. 2013, ApJ, 763, 18
Bell, E. F., & de Jong, R. S. 2000, MNRAS, 312, 497
Bell, E. F., van der Wel, A., Papovich, C., et al. 2012, ApJ, 753, 167
Belli, S., Newman, A. B., & Ellis, R. S. 2014, ApJ, 783, 117
Belli, S., Newman, A. B., & Ellis, R. S. 2015, ApJ, 799, 206
Bourne, N., Dunne, L., Maddox, S. J., et al. 2016, MNRAS, 462, 1714
Brammer, G. B., van Dokkum, P. G., & Coppi, P. 2008, ApJ, 686, 1503
Brammer, G. B., Whitaker, K. E., van Dokkum, P. G., et al. 2011, ApJ, 739, 24
Brennan, R., Pandya, V., Somerville, R. S., et al. 2015, MNRAS, 451, 2933
Brennan, R., Pandya, V., Somerville, R. S., et al. 2017, MNRAS, 465, 619
Bruce, V. A., Dunlop, J. S., Cirasuolo, M., et al. 2012, MNRAS, 427, 1666
Bruzual, G., & Charlot, S. 2003, MNRAS, 344, 1000
Calzetti, D., Armus, L., Bohlin, R., et al. 2000, ApJ, 533, 682
Cameron, E., Carollo, C. M., Oesch, P. A., et al. 2011, ApJ, 743, 146
Cassará, L. P., Maccagni, D., Garilli, B., et al. 2016, A&A, 593, 14
Cassata, P., Cimatti, A., Kurk, J., et al. 2008, A&A, 483L, 39
Cassata, P., Giavalisco, M., Guo, Y., et al. 2010, ApJ, 714L, 79
Cassata, P., Giavalisco, M., Guo, Y., et al. 2011, ApJ, 743, 96
Cassata, P., Giavalisco, M., Williams, C. C., et al. 2013, ApJ, 775, 106
Charlot, S., & Fall, S. M. 2000, ApJ, 539, 718
Chary, R., & Elbaz, D. 2001, ApJ, 556, 562
Cheung, E., Faber, S. M., Koo, D. C., et al. 2012, ApJ, 760, 131
Cimatti, A., Daddi, E., Renzini, A., et al. 2004, Natur, 430, 184
Conroy, C. 2013, ARA&A, 51, 393
Conroy, C., Gunn, J. E., & White, M. 2009, ApJ, 699, 486
Conselice, C. J. 2003, ApJS, 147, 1
Daddi, E., Dickinson, M., Morrison, G., et al. 2007, ApJ, 670, 156
Daddi, E., Elbaz, D., Walter, F., et al. 2010, ApJL, 714, L118
Dahlen, T., Bahram, M., Faber, S. M., et al. 2013, ApJ, 775, 93
Dekel, A., Birnboim, G., Engel, G., et al. 2009, Natur, 457, 451
Dekel, A., & Birnboim, Y. 2008, MNRAS, 383, 119
Dekel, A., & Burkert, A. 2014, MNRAS, 438, 1870

Dekel, A., Zolotov, A., Tweed, D., et al. 2013, MNRAS, 435, 999
Donley, J. L., Koekemoer, A. M., Brusa, M., et al. 2012, ApJ, 748, 142
Elbaz, D., Dickinson, M., Hwang, H. S., et al. 2011, A&A, 533, 119
Fagioli, M., Carollo, C. M., Renzini, A., et al. 2016, ApJ, 831, 173
Fang, G., Kong, X., Chen, Y., & Lin, X. 2012, ApJ, 751, 109
Fang, J. J., Faber, S. M., Koo, D. C., et al. 2017, ApJ, submitted (arXiv:1710.05489)
Fang, J. J., Faber, S. M., Koo, D. C., & Dekel, A. 2013, ApJ, 776, 63
Franx, M., van Dokkum, P. G., Forster, S., et al. 2008, ApJ, 688, 770
Fumagalli, M., Labbé, I., Patel, S. G., et al. 2014, ApJ, 796, 35
Gavazzi, G., Consolandi, G., Dotti, M., et al. 2015, A&A, 580, 116
Gelman, A., & Rubin, D. B. 1992, StaSc, 7, 457
Genzel, R., Newman, S., Jones, T., et al. 2011, ApJ, 733, 101
Grogin, N. A., Kocevski, D. D., Faber, S. M., et al. 2011, ApJS, 197, 35
Guo., Y., Bell, E. F., Lu, Y., et al. 2017, ApJ, 841, 22
Guo, Y., Ferguson, H. C., Giavalisco, M., et al. 2013, ApJS, 207, 24
Guo, Y., Giavalisco, M., Cassata, P., et al. 2012, ApJ, 749, 149
Hayward, C. C., Lanz, L., Ashby, M. L. N., et al. 2014, MNRAS, 445, 1598
Hopkins, P. F., Cox, T. J., Younger, J. D., & Hernquist, L. 2009, ApJ, 691, 1168
Hopkins, P. F., Hernquist, L., Cox, T. J., et al. 2006, ApJS, 163, 1
Hopkins, P. F., Hernquist, L., Cox, T. J., Dutta, S. N., & Rothberg, B. 2008, ApJ, 679, 156
Johansson, P. H., Naab, T., & Ostriker, J. P. 2012, ApJ, 754, 115
Kajisawa, M., Morishita, T., Taniguchi, Y., et al. 2015, ApJ, 801, 134
Karim, A., Schinnerer, E., Martínez-Sansigre, A., Sargent, M. T., et al. 2011, ApJ, 730, 61
Keres, D., Katz, N., Weinberg, D. H., et al. 2005, MNRAS, 363, 2
Kirkpatrick, A., Pope, A., Sajini, A., Roebuck, E., et al. 2015, ApJ, 814, 9
Klypin, A. A., Trujillo-Gomez, S., & Promack, J. 2011, ApJ, 740, 102
Koekemoer, A. M., Faber, S. M., Ferguson, H. C., et al. 2011, ApJS, 197, 36
Kriek, M., van Dokkum, P. G., Franx, M., et al. 2009, ApJL, 705, L71
Laidler, V. G., Papovich, C., Grogin, N. A., et al. 2007, PASP, 119, 1325
Lang, P., Wuyts, S., Somerville, R. S., et al. 2014, ApJ, 788, 11
Law, D. R., Steidel, C. C., Erb, D. K., et al. 2007, ApJ, 656, 1
Lee, B., Giavalisco, M., Williams, C. C., et al. 2013, ApJ, 774, 47
Lee, K.-S., Arjun, D., Reedy, N., et al. 2011, ApJ, 739, 99
Lee, N., Sanders, D. B., Casey, C. M., et al. 2015, ApJ, 801, 80
Lee, S.-K., Ferguson, H. C., Somerville, R. S., Wiklind, T., & Giavalisco, M. 2010, ApJ, 725, 1644
Lee, S.-K., Idzi, R., Ferguson, H. C., et al. 2009, ApJS, 184, 100
Lilly, S. J., & Carollo, C. M. 2016, ApJ, 833, 1
Lilly, S. J., Carollo, C. M., Pipino, A., Renzini, A., & Peng, Y. 2013, ApJ, 772, 119
Lotz, J. M., Davis, M., Faber, S. M., et al. 2008, ApJ, 672, 177
Lotz, J. M., Primack, J., & Madau, P. 2004, AJ, 128, 163
Luo, B., Brandt, W. N., Xue, Y. Q., et al. 2017, ApJS, 228, 2
MAdau, P. 1995, ApJ, 441, 18
Madau, P., & Dickinson, M. 2014, ARAA, 52, 415
Magnelli, B., Elbaz, D., Chary, R. R., et al. 2009, AA, 496, 57
Maraston, C. 2005, MNRAS, 362, 799
Maraston, C., Pforr, J., Renzini, A., et al. 2010, MNRAS, 407, 830
McIntosh, D. H., Wagner, C., Cooper, A., et al. 2014, MNRAS, 442, 533
Mendez, A. J., Coil, A. L., Lotz, J., et al. 2011, ApJ, 736, 110
Meurer, G. R., Heckman, T. M., & Calzetti, D. 1999, ApJ, 521, 64
Murphy, E. J., Chary, R.-R., Dickinson, M., et al. 2011, ApJ, 732, 126
Muzzin, A., Marchesini, D., Stefanon, M., et al. 2013, ApJS, 206, 8
Muzzin, A., Marchesini, D., van Dokkum, P. G., et al. 2009, ApJ, 701, 1839
Nelson, E., van Dokkum, P., Franx, M., et al. 2014, Natur, 513, 394
Noeske, K. G., Weiner, B. J., Faber, S. M., et al. 2007, ApJL, 660, L43
Pacifici, C., Kassi, S. A., Weiner, B., Charlot, S., & Gardner, J. P. 2013, ApJ, 762, 15
Padovani, P., Miller, N., Kellermann, K. I., et al. 2011, ApJ, 740, 20
Pandya, V., Brennan, R., Somerville, R. S., et al. 2017, MNRAS, 472, 2054
Pannella, M., Carilli, C. L., Daddi, E., et al. 2009, ApJL, 698, L116
Pannella, M., Elbaz, D., Daddi, E., et al. 2015, ApJ, 807, 141
Papovich, C., Finkelstein, S. L., Freguson, H. C., et al. 2011, MNRAS, 412, 1123
Patel, S. G., van Dokkum, P., Franx, M., et al. 2013, ApJ, 766, 15
Peng, Y.-J., Lilly, S. J., Kovac, K., et al. 2010, ApJ, 721, 193
Peng, Y.-j., Lilly, S. J., Renzini, A., et al. 2012, ApJ, 757, 4
Peth, M., Lotz, J. M., Freeman, P. E., et al. 2016, MNRAS, 458, 963
Pforr, J., Maraston, C., & Tonini, C. 2012, MNRAS, 422, 3285
Quadri, R. F., Williams, R. J., Franx, M., & Hildebrandt, H. 2012, ApJ, 744, 88
Reddy, N. A., Pettini, M., Steidel, C. C., et al. 2012, ApJ, 754, 25

Renzini, A. 2009, MNRAS, 398, L58
Renzini, A., & Peng, Y. 2015, ApJL, 80, 29
Rodighiero, G., Daddi, E., Baronchelli, I., et al. 2011, ApJL, 739, L40
Salim, S., Dickinson, M., Michael, R. R., et al. 2009, ApJ, 700, 161
Salmi, F., Elbaz, D., Sargent, M. T., et al. 2012, ApJL, 754, L14
Salmon, B., Papovich, C., Finkelstein, S. L., et al. 2015, ApJ, 799, 183
Santini, P., Ferguson, H. C., Fontana, A., et al. 2015, ApJ, 801, 97
Sargent, M. T., Bethermin, M., Daddi, E., & Elbaz, D. 2012, ApJL, 747, L31
Sargent, M. T., Daddi, E., Bethermin, M., et al. 2014, ApJ, 793, 19
Schaerer, D., & de Barros, S. 2009, A&A, 592, 423
Schawinski, K., Urry, C. M., Simmons, B. D., et al. 2014, MNRAS, 440, 889
Schreiber, C., Elbaz, D., Pannella, M., et al. 2016, A&A, 589, 35
Schreiber, C., Pannella, M., Elbaz, D., et al. 2015, A&A, 575, 74
Shibuya, T., Ouchi, M., Harikane, Y., et al. 2015, ApJS, 219, 15
Simha, V., Weinberg, D. H., Conroy, C., et al. 2014, arXiv:1404.0402
Sobral, D., Best, P. N., Matsuda, Y., et al. 2012, MNRAS, 420, 1926
Somerville, R. S., Gilmore, R. C., Primack, J. R., & Dominguez, A. 2012,
    MNRAS, 423, 1992
Speagle, J. S., Steinhardt, C. L., Capak, P. L., & Silverman, J. D. 2014, ApJS,
    214, 15
Spilker, J. S., Bezanson, R., Marrone, D. P., et al. 2016, ApJ, 832, 19
Springel, V., Di Matteo, T., & Hernquist, L. 2005, MNRAS, 361, 776
Szomoru, D., Franx, M., Bouwens, R. J., et al. 2011, ApJL, 735, L22
Szomoru, D., Franx, M., van Dokkum, P. G., et al. 2010, ApJ, 714, 244
Szomoru, D., Franx, M., van Dokkum, P. G., et al. 2013, ApJ, 763, 73
Tacchella, S., Dekel, A., Carollo, C. M., et al. 2016a, MNRAS, 457, 2790
Tacchella, S., Dekel, A., Carollo, C. M., et al. 2016b, MNRAS, 458, 242
Tal, T., Delek, A., Oesch, P., et al. 2014, ApJ, 789, 164
Tomczak, A. R., Quadri, R. F., Tran, K. H., et al. 2016, ApJ, 817, 118

Trujillo, I., Conselice, C. J., Bundy, K., et al. 2007, MNRAS, 382, 109
Trujillo, I., Feulner, G., Goranova, Y., et al. 2006, MNRAS, 373, 36
Utomo, D., Kriek, M., Labbé, I., Conroy, C., & Fumagali, M. 2014, ApJ,
    783, 30
van der Wel, A., Bell, E. F., Häussler, B., et al. 2012, ApJS, 230, 24
van der Wel, A., Rix, H.-W., Wuyts, S., et al. 2011, ApJ, 730, 38
van Dokkum, P. G., Franx, M., Kriek, M., et al. 2008, ApJL, 677, L5
van Dokkum, P. G., Nelson, E. J., Franx, M., et al. 2015, ApJ, 813, 23
Wang, T., Huang, J.-S., Faber, S. M., et al. 2012, ApJ, 752, 134
Wellons, S., Torrey, P., Ma, C., et al. 2015, MNRAS, 449, 361
Whitaker, K. E., Bezanson, R., van Dokkum, P. G., et al. 2017, ApJ, 838,
    19
Whitaker, K. E., Franx, M., Bezanson, R., et al. 2015, ApJ, 811L, 12
Whitaker, K. E., Franx, M., Leja, J., et al. 2014, ApJ, 795, 104
Whitaker, K. E., Kriek, M., van Dokkum, P. G., et al. 2012, ApJ, 745, 179
Whitaker, K. E., Labbe, I., van Dokkum, P. G., et al. 2011, ApJ, 735, 86
Whitaker, K. E., van Dokkum, P. G., Brammer, G., & Franx, M. 2012, ApJ,
    754L, 29
Williams, C. C., Giavalisco, M., Bezanson, R., et al. 2017, ApJ, 838, 94
Williams, C. C., Giavalisco, M., Cassata, P., et al. 2014, ApJ, 780, 1
Williams, C. C., Giavalisco, M., Lee, B., et al. 2015, ApJ, 800, 21
Williams, R. J., Quadri, R. F., Franx, M., et al. 2009, ApJ, 691, 1879
Woo, J., Dekel, A., Faber, S. M., & Koo, D. C. 2015, MNRAS, 448, 237
Wuyts, S., Cox, T. J., Hayward, C. C., et al. 2010, ApJ, 722, 1666
Wuyts, S., Förster Schreiber, N. M., van der Wel, A., et al. 2011, ApJ, 742, 96
Wuyts, S., Franx, M., Cox, T. J., et al. 2009, ApJ, 696, 348
Xue, Y. Q., Luo, B., Brandt, W. N., et al. 2011, ApJS, 195, 10
Xue, Y. Q., Luo, B., Brandt, W. N., et al. 2016, ApJS, 224, 15
Zolotov, A., Dekel, A., Mandelker, N., et al. 2015, MNRAS, 450, 2327